

Adaptive Optics for High Energy Laser Systems

by

Joseph Edward Wall, III

B.S., Electrical Engineering, Tulane University, (1992)

SUBMITTED TO THE DEPARTMENT OF
ELECTRICAL ENGINEERING AND COMPUTER SCIENCE
IN PARTIAL FULFILLMENT OF THE REQUIREMENTS FOR THE DEGREE OF

MASTER OF SCIENCE
IN ELECTRICAL ENGINEERING AND COMPUTER SCIENCE

at the

MASSACHUSETTS INSTITUTE OF TECHNOLOGY
May 1994

© Joseph E. Wall, III

Signature of Author _____

Department of Electrical Engineering
and Computer Science, May 1994

Certified by _____

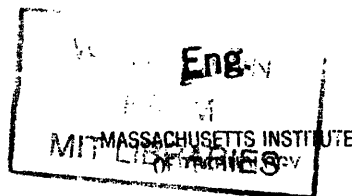
Dr. Brent Appleby
Technical Supervisor
Charles Stark Draper Laboratory

Certified by _____

Dr. Michael Athans
Professor of Systems Science and Engineering
Department of Electrical Engineering and Computer Science
Thesis Supervisor

Accepted by _____

Dr. Frederic R. Morgenthaler
Chairman, Department Graduate Committee
Department of Electrical Engineering and Computer Science



JUL 13 1994

LIBRARIES

Adaptive Optics for High Energy Laser Systems

by

Joseph Edward Wall, III

Submitted to the Department of Electrical Engineering and Computer Science
on May 30, 1994 in Partial Fulfillment of the Requirements for
the Degree of Master of Science in Electrical Engineering and Computer Science

ABSTRACT

High-energy laser propagation in the atmosphere requires consideration of self-induced beam expansion due to thermal blooming and random distortion due to atmospheric turbulence. Thermal blooming is a result of interaction between the laser radiation and the propagation path. A small portion of the laser energy is absorbed by the atmosphere. This energy heats the air causing it to expand and form a distributed thermal lens along the path. The refractive index of the medium is decreased in the region of the beam where heating is the greatest, causing the beam to spread. Atmospheric turbulence is caused by random naturally occurring temperature gradients in the atmosphere.

This research focuses on the design of beam control systems for high-energy lasers. In particular, it compares traditional phase conjugation and open loop techniques to a model-based optimal correction technique which modifies the laser power and focal length. For light thermal blooming, phase conjugation is seen to be a reasonable control strategy. However, as the level of thermal blooming increases, phase conjugation performs increasingly worse. For moderate to heavy thermal blooming scenarios, the new technique is shown to increase peak intensity on target up to 50% more than traditional compensation methods. Additionally, the optimal correction technique is insensitive to errors in the model parameters. The system under consideration is a ground-based continuous wave laser operating in an environment with wind. It is assumed that a tracking system provides target position and velocity information. A reflection of the laser wavefront off the target is useful, but not required.

Thesis Supervisor:

Title:

Dr. Michael Athans

Professor of Systems Science and Engineering

Technical Supervisor:

Title:

Dr. Brent Appleby

Senior Member of the Technical Staff

Acknowledgments

I would like to thank The Charles Stark Draper Laboratory for providing me with the opportunity to pursue my graduate studies at MIT. I am especially grateful to my supervisor at Draper, Dr. Brent Appleby, for his continuous assistance with all aspects of my research.

Additionally, I would like to thank Greg Cappiello for his assistance with the optical part of the project, Dr. John Dowdle for his overall guidance, and Professor Michael Athans for his inspiring courses and insightful suggestions for this thesis.

This thesis was prepared at The Charles Stark Draper Laboratory, Inc., under Independent Research and Development Project No. 529: Adaptive Optics for Beam Control in an Unstable Medium. Draper Laboratory's financial support under this project was greatly appreciated.

Publication of this thesis does not constitute approval by the Draper Laboratory or the Massachusetts Institute of Technology of the findings or conclusions contained herein. It is published for the exchange and stimulation of ideas.

I hereby assign my copyright of this thesis to The Charles Stark Draper Laboratory, Inc., Cambridge, Massachusetts.

Permission is hereby granted by The Charles Stark Draper Laboratory, Inc., to the Massachusetts Institute of Technology to reproduce any or all of this thesis.

Table of Contents

| | |
|---|----|
| List of Tables | 11 |
| List of Figures | 13 |
| 1 Introduction | 17 |
| 1.1 Typical High Energy Laser Platform | 18 |
| 1.2 High Energy Laser Issues | 20 |
| 1.3 Project Purpose | 21 |
| 1.4 Phase Conjugation Overview | 22 |
| 1.5 Thesis Contributions | 23 |
| 1.6 Thesis Outline | 24 |
| 2 Mathematical Foundation of Thermal Blooming | 27 |
| 2.1 Analytic Derivation of Thermal Blooming Equations | 28 |
| 2.2 Approximations to Steady State Thermal Blooming | 29 |
| 2.3 Relationship Between Phase Error and Intensity | 32 |
| 2.4 Introduction to Zernike Polynomials | 35 |
| 2.5 Summary | 35 |
| 3 Thermal Blooming Model | 37 |
| 3.1 Thermal Blooming Model Parameters | 37 |
| 3.2 Peak Intensity | 39 |
| 3.3 Critical Power | 41 |
| 3.4 Dispersive Effects | 42 |
| 3.4.1 Random Linear Effects | 42 |
| 3.4.2 Deterministic Nonlinear Effects | 43 |
| 3.4.3 Heating Phase | 44 |
| 3.5 Parameterization of Aberrated Beam | 46 |
| 3.5.1 Focus | 48 |
| 3.5.2 Astigmatism | 48 |
| 3.5.3 Coma | 49 |
| 3.5.4 Spherical | 50 |
| 3.6 Simulations | 50 |

| | | |
|----------|---|------------|
| 3.7 | Summary | 52 |
| 4 | Atmospheric Turbulence Model..... | 53 |
| 4.1 | Turbulence Model Parameters | 53 |
| 4.2 | Zernike Coefficient Modeling..... | 54 |
| 4.2.1 | Power Spectral Density..... | 55 |
| 4.2.2 | Power Spectral Density Approximation | 57 |
| 4.2.3 | Transfer Function Gain..... | 59 |
| 4.3 | Simulations..... | 61 |
| 4.4 | Covariance of Primary Modes | 66 |
| 4.5 | Summary | 68 |
| 5 | Optimal Atmospheric Correction..... | 69 |
| 5.1 | Control Strategies | 70 |
| 5.1.1 | Open Loop | 70 |
| 5.1.2 | Phase Conjugation | 70 |
| 5.1.3 | Optimal Focal Length..... | 71 |
| 5.1.4 | Optimal Focal Length with Optimal Power..... | 72 |
| 5.2 | Simulations..... | 73 |
| 5.2.1 | Light Thermal Blooming | 73 |
| 5.2.2 | Moderate Thermal Blooming..... | 76 |
| 5.2.3 | Heavy Thermal Blooming..... | 79 |
| 5.3 | Summary | 82 |
| 6 | Parameter Sensitivity and Estimation..... | 85 |
| 6.1 | Parameter Sensitivity..... | 86 |
| 6.2 | Extended Kalman Filter Design..... | 88 |
| 6.2.1 | Basic Equations..... | 88 |
| 6.2.2 | Implementation | 91 |
| 6.3 | Simulations..... | 93 |
| 6.4 | Summary..... | 103 |
| 7 | Realistic Thermal Blooming Correction..... | 105 |
| 7.1 | Parameter Uncertainty Models | 106 |
| 7.1.1 | Atmospheric Constants..... | 106 |
| 7.1.2 | Target Information..... | 106 |

| | | |
|----------|------------------------------------|------------|
| 7.1.3 | Wind..... | 106 |
| 7.2 | Simulations | 107 |
| 7.2.1 | Light Thermal Blooming..... | 107 |
| 7.2.2 | Moderate Thermal Blooming..... | 111 |
| 7.2.3 | Heavy Thermal Blooming | 115 |
| 7.3 | Summary..... | 119 |
| 8 | Conclusions | 121 |
| 8.1 | Conclusions | 121 |
| 8.2 | Recommendations | 123 |
| A | Zernike Polynomials..... | 125 |
| B | Parameter Sensitivity | 133 |
| | References..... | 147 |

List of Tables

| | | |
|-----|---|-----|
| 3.1 | Thermal Blooming Model Parameters | 38 |
| 4.1 | Atmospheric Turbulence Model Parameters..... | 54 |
| 4.2 | h-Functions | 56 |
| 4.3 | Atmospheric Turbulence Scaled Corner Frequencies (Hertz)..... | 58 |
| 4.4 | Zernike Mode Variance Relative to σ_1 | 61 |
| A.1 | Zernike Polynomial Functions | 126 |

List of Figures

| | | |
|-----|---|----|
| 1.1 | Typical High Energy Laser Platform..... | 20 |
| 1.2 | Effect of Thermal Blooming on Power-Intensity Curve..... | 21 |
| 1.3 | Phase Conjugation Overview | 23 |
| 2.1 | Wavefront and Equal Intensity Contours for a Thermally Bloomed Wave..... | 32 |
| 2.2 | Coordinate System for Intensity Equations | 33 |
| 2.3 | Strehl Ratio as a Function of Wavefront Error..... | 35 |
| 3.1 | Effects of Diffraction and Thermal Blooming on Beam Spreading..... | 39 |
| 3.2 | Intensity as a Function of Laser Power for Various Wind Speeds | 42 |
| 3.3 | Ray Diagram for Focus Aberration..... | 48 |
| 3.4 | Ray Diagram for Astigmatism Aberration | 49 |
| 3.5 | Ray Diagram for Coma Aberration..... | 49 |
| 3.6 | Ray Diagram for Spherical Aberration..... | 50 |
| 3.7 | Typical Wavefront for Light Thermal Blooming | 51 |
| 3.8 | Typical Wavefront for Heavy Thermal Blooming..... | 51 |
| 4.1 | Model for Zernike Turbulence Coefficient | 55 |
| 4.2 | Wavefront Distortion Due to Turbulence, Stationary Target Light Wind..... | 62 |
| 4.3 | Wavefront Distortion Due to Turbulence, Moving Target Moderate Wind..... | 62 |
| 4.4 | RMS Zernike Coefficient Values Corresponding to Figure 4.2 | 63 |
| 4.5 | RMS Zernike Coefficient Values Corresponding to Figure 4.3 | 63 |
| 4.6 | Zernike Coefficient Time History Corresponding to Figure 4.2..... | 64 |
| 4.7 | Zernike Coefficient Time History Corresponding to Figure 4.3..... | 65 |
| 5.1 | Intensity as a Function of Focal Length | 72 |
| 5.2 | Intensity as a Function of Focal Length and Laser Power..... | 73 |
| 5.3 | Target Route for Light Thermal Blooming Scenario | 74 |
| 5.4 | Performance Comparison for Light Thermal Blooming | 75 |
| 5.5 | Intensity as a Function of Focal Length for Light Thermal Blooming Indicating Open Loop, Phase Conjugate, and Optimal Focus Focal Ranges ... | 76 |
| 5.6 | Target Route for Moderate Thermal Blooming Scenario | 77 |

| | | |
|------|--|-----|
| 5.7 | Performance Comparison for Moderate Thermal Blooming | 78 |
| 5.8 | Intensity as a Function of Focal Length for Moderate Thermal Blooming Indicating Open Loop, Phase Conjugate, and Optimal Focus Focal Ranges ... | 79 |
| 5.9 | Target Route for Heavy Thermal Blooming Scenarios | 80 |
| 5.10 | Performance Comparison for Heavy Thermal Blooming..... | 81 |
| 5.11 | Intensity as a Function of Focal Length for Heavy Thermal Blooming Indicating Open Loop, Phase Conjugate, and Optimal Focus Focal Ranges ... | 82 |
| 6.1 | Sensitivity to Refractive Index..... | 87 |
| 6.2 | Sensitivity to Transverse Wind Velocity..... | 88 |
| 6.3 | Kalman Filter Performance with Parameters Known Exactly..... | 94 |
| 6.4 | Kalman Filter Performance with Maximum Parameter Error of 2.5%..... | 95 |
| 6.5 | Kalman Filter Performance with Maximum Parameter Error of 5% | 95 |
| 6.6 | Kalman Filter Performance with Maximum Parameter Error of 10%..... | 96 |
| 6.7 | RMS Wind Estimate Error as a Function of Target Velocity Error..... | 97 |
| 6.8 | RMS Wind Estimate Error as a Function of Target Distance Error..... | 97 |
| 6.9 | Estimation Error Statistics for Light Thermal Blooming Simulations..... | 99 |
| 6.10 | Estimation Error Statistics for Light Thermal Blooming Simulations | 100 |
| 6.11 | Return Wavefront Zernike Coefficients as a Function of Wind Speed | 101 |
| 6.12 | Estimation Error Statistics for Heavy Thermal Blooming Simulations..... | 102 |
| 7.1 | Performance Comparison for Light Thermal Blooming..... | 108 |
| 7.2 | Estimator Performance for Light Thermal Blooming..... | 109 |
| 7.3 | Performance Comparison for Light Thermal Blooming with Parameter Errors... | 110 |
| 7.4 | Estimator Performance for Light Thermal Blooming with Parameter Errors | 111 |
| 7.5 | Performance Comparison for Moderate Thermal Blooming..... | 112 |
| 7.6 | Estimator Performance for Moderate Thermal Blooming | 113 |
| 7.7 | Performance Comparison for Moderate Thermal Blooming with Parameter Errors | 114 |
| 7.8 | Estimator Performance for Moderate Thermal Blooming with Parameter Errors . | 115 |
| 7.9 | Performance Comparison for Heavy Thermal Blooming | 116 |
| 7.10 | Estimator Performance for Heavy Thermal Blooming | 117 |
| 7.11 | Performance Comparison for Heavy Thermal Blooming with Parameter Errors.. | 118 |
| 7.12 | Estimator Performance for Heavy Thermal Blooming with Parameter Errors..... | 119 |

| | | |
|------|---|-----|
| A.1 | Zernike Polynomial Functions 1-4..... | 127 |
| A.2 | Zernike Polynomial Functions 5-8..... | 128 |
| A.3 | Zernike Polynomial Functions 9-12 | 129 |
| A.4 | Zernike Polynomial Functions 13-16..... | 130 |
| A.5 | Zernike Polynomial Functions 17-20..... | 131 |
| | | |
| B.1 | Sensitivity to Transverse Wind Velocity | 134 |
| B.2 | Sensitivity to Turbulence Constant | 135 |
| B.3 | Sensitivity to Absorption Coefficient..... | 136 |
| B.4 | Sensitivity to Scattering Coefficient | 137 |
| B.5 | Sensitivity to Refractive Index | 138 |
| B.6 | Sensitivity to Refractive Index Gradient | 139 |
| B.7 | Sensitivity to Air Density | 140 |
| B.8 | Sensitivity to Specific Heat | 141 |
| B.9 | Sensitivity to Beam Quality..... | 142 |
| B.10 | Sensitivity to Beam Spread due to Jitter | 143 |
| B.11 | Sensitivity to Beam Spread due to Wander | 144 |
| B.12 | Sensitivity to Transverse Target Velocity | 145 |
| B.13 | Sensitivity to Target Distance..... | 146 |

Chapter 1

Introduction

The concept of directed energy systems can be traced back to Archimedes' defense of Syracuse in 215 B.C. By positioning their polished shields to focus sunlight towards small areas on the sides of approaching Roman ships, the Syracuse army was able to ignite the ships and defeat the attackers. The U.S. military is currently developing several directed-energy systems employing high-energy lasers that are now in the conceptual design stage. The Air Force is developing the Airborne Laser. The Army is considering a ground-based system, GARDIAN, as well as an airborne system, Defender. Finally, the Navy is considering ship-based systems. In addition to military applications, directed-energy systems have been proposed as a means to deliver large amounts of power to lunar stations and earth-orbiting satellites. Remote power sources would significantly reduce onboard power requirements.

Because of the extremely high levels of laser power used in directed energy systems, propagation models must include the effect of self-induced beam expansion due to thermal blooming as well as random distortion due to atmospheric turbulence. Thermal blooming

is a result of interaction between the laser radiation and the propagation path. A portion of the laser energy is absorbed by the atmosphere. This energy heats the air causing it to expand and form a distributed thermal lens along the path. The refractive index of the medium is decreased in the region of the beam where heating is the greatest, causing the beam to spread. Atmospheric turbulence is caused by random naturally occurring temperature gradients in the atmosphere.

This research focuses on the design of beam control systems for high-energy lasers. It compares open loop and phase conjugate methods to model-based optimal correction techniques. The optimal correction techniques allow for modification of focal length and laser power. It will be shown that for moderate and heavy cases of thermal blooming, as occurs for a slow moving target in light wind, phase conjugation is a poor method for maximizing intensity on target. When thermal blooming is strong, modification of focal length or laser power increases intensity on target 20% over open loop and 100% over phase conjugation. The system under consideration is a ground-based continuous wave laser operating in an environment with wind. It is assumed that a reflection of the laser off the target is available for measurement.

1.1 TYPICAL HIGH ENERGY LASER PLATFORM

The optical path of a typical ground-based high energy laser platform is given in Figure 1.1. The mirrors and separators, in the order of an outgoing wave, are described below [1].

Deformable Mirror - deforms the wavefront taking into account the wavefronts received at the incoming and outgoing wavefront sensors.

Beam Splitter - allows a small amount of the laser to be fed to the wavefront sensor while reflecting the rest onto the deformable mirror.

Outgoing Wavefront Sensor - detects the wavefront error before the laser is reflected off any mirrors.

Turning Mirror - reflects the beam.

Tilt Mirror - high bandwidth mirror which can point the beam in any direction, used to remove tilt errors from the wavefront.

Beam Expander - consists of a small convex mirror and a larger concave mirror. It allows beam steering and focusing.

Large Turning Mirror (Traverse) - used for course pointing in combination with rotation of the whole beam expander. It has limited orthogonal motion capability creating a traverse axis for better dynamic performance.

This project is concerned with measurements taken at the incoming wavefront sensor, commands given to the deformable mirror, and the power of the high energy laser.

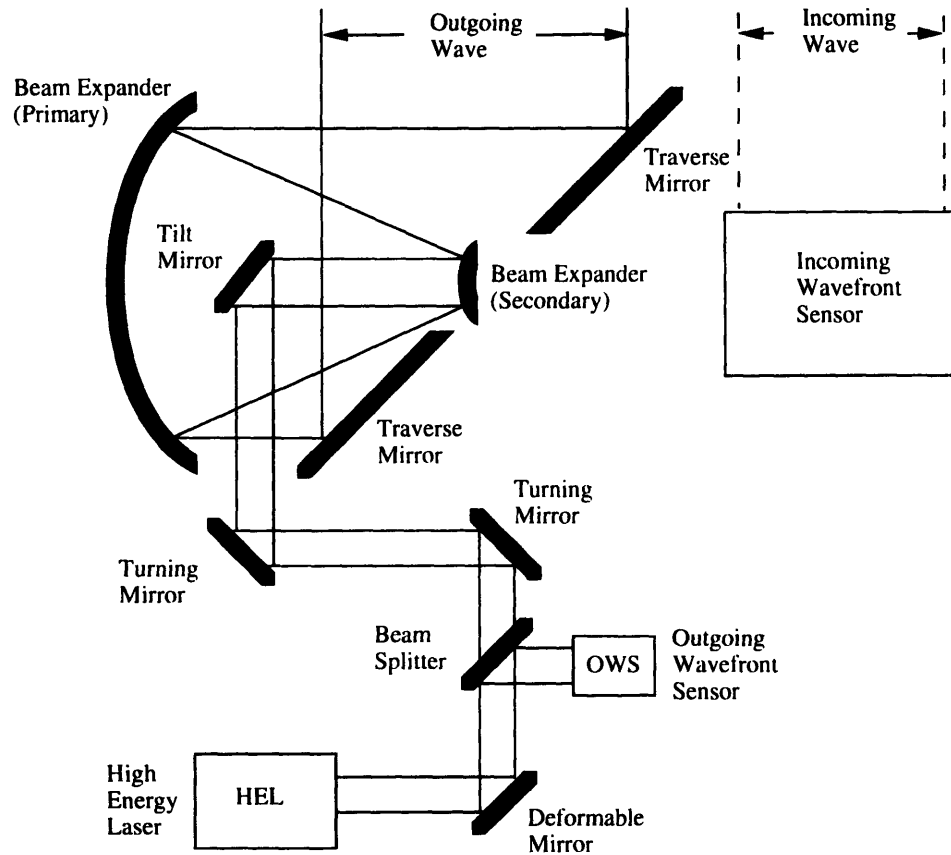


Figure 1.1. Typical High Energy Laser Platform.

1.2 HIGH ENERGY LASER ISSUES

The purpose of a high-energy laser system is to deliver power to a target. Several atmospheric effects decrease the effectiveness of such a system. These effects include both linear and nonlinear terms. Diffraction, turbulence, jitter, and wander linearly decrease the intensity on target. If the nonlinear effects are ignored, any increase in intensity on target can be accomplished by increasing the laser power. When the nonlinear effect of thermal blooming is included, increasing laser power will not always be beneficial and can even reduce the level of transmitted power. Figure 1.2 shows the performance of an open loop system by determining intensity on target as a function of laser power with and without

blooming. As seen in Figure 1.2, it is clear that thermal blooming must be considered when evaluating this system if the laser is operating above 25,000 Watts. If thermal blooming is ignored in the design stage, the actual intensity on target will be a small fraction of what is expected.

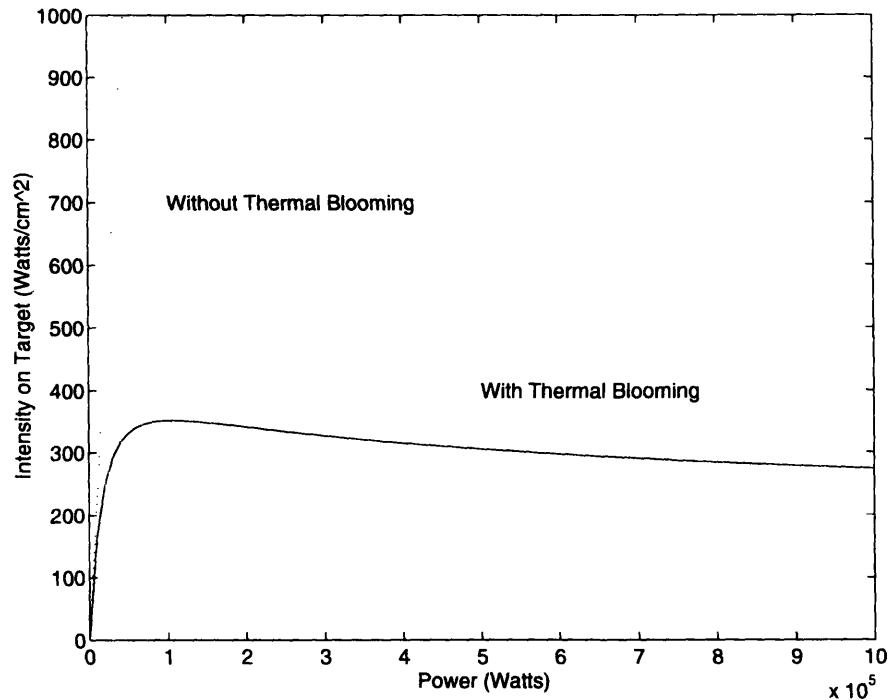


Figure 1.2. Effect of Thermal Blooming on Power-Intensity Curve.

1.3 PROJECT PURPOSE

For any high-energy ground-based laser application, compensation for thermal blooming should be considered. Extensive work has been done on the subject of both thermal blooming and adaptive optics [2,3,4]. A brief history of the work on thermal blooming is given by Gebhardt [5]. Tyson presents a thorough introduction to adaptive optics [1]. Generally two approaches are taken for modeling thermal blooming - simple scaling laws and complex wave propagation codes. The scaling laws provide order of magnitude results useful for quick approximations. The wave propagation codes closely match experimental

results, but are computationally intensive. One of the more famous propagation codes was developed at Lincoln Laboratory by Bradley and Hermann [6]. The model described in this thesis expands on the simple scaling laws by allowing for modification of the outgoing wavefront, (the whole idea of adaptive optics), while at the same time remaining analytically tractable and not requiring the use of a supercomputer [7]. The use of adaptive optics systems to compensate for atmospheric effects allows for greater energy delivery on target at any point along the power-intensity curve. The purpose of this research is to examine current methods of beam control and to propose an alternative, model-based approach. While not a detailed evaluation of one particular laser system, this project attempts to be a useful tool for evaluating adaptive optics systems in general.

1.4 PHASE CONJUGATION OVERVIEW

The most common approach for compensation of atmospheric aberrations is phase conjugation. A plane reference wavefront travels through an aberration source. The distortion caused by the aberrator is measured by a wavefront sensor. The outgoing wavefront is predistorted by the phase conjugate of the measured wavefront. Ideally the aberrator causes the same distortion as it did to the reference wavefront and the outgoing wavefront reaches its target undistorted. Figure 1.3 demonstrates the phase conjugation method.

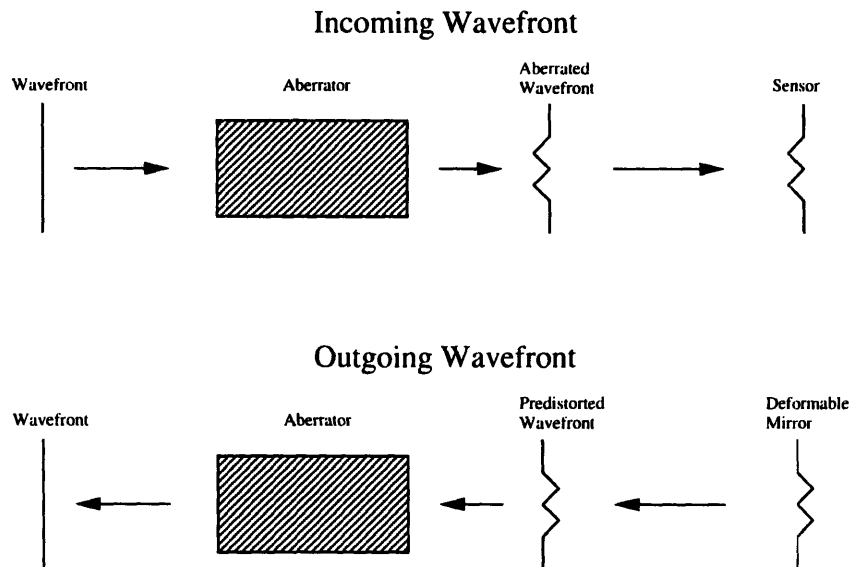


Figure 1.3. Phase Conjugation Overview.

Distortion caused by atmospheric turbulence is independent of the applied phase and phase conjugation has the possibility of significantly reducing wavefront distortion at the target. However, the atmospheric distortion caused by thermal blooming is a function of the applied phase. It will be shown that phase conjugation techniques are not optimal and model-based controllers can improve the performance of directed energy systems. It has been recognized for some time that phase conjugation methods are prone to instability. The phenomenon of phase compensation instability, PCI, has been studied extensively [8,9].

1.5 THESIS CONTRIBUTIONS

A simulation tool has been developed to allow the comparison of alternative control techniques for high-energy laser systems. The performance of phase conjugation, open loop, and an optimal correction technique which modifies the laser power and focal length are compared under light, moderate, and heavy thermal blooming scenarios. The main components of the simulator are a thermal blooming model, an atmospheric turbulence

model, and the implementation of the various control techniques. The thermal blooming model pieces together work done by a number of authors at the Ballistic Research Laboratory, the U.S. Army High Energy Laser Systems Project Office, and the Charles Stark Draper Laboratory. The atmospheric turbulence model was developed by researchers at The Analytical Sciences Corporation.

The optimal correction technique determines the optimal laser focal range and power using an internal model of thermal blooming. The concept of using an internal model of thermal blooming in an adaptive optics system has not previously been studied. The optimal correction technique uses an extended Kalman filter to estimate the wind speed from return wavefront measurements.

1.6 THESIS OUTLINE

The primary goal of this thesis is to evaluate current methods of wavefront control and compare them with novel, model-based control techniques that modify the focal range and laser power. Models of thermal blooming and atmospheric turbulence are presented. The performance of the various systems is compared assuming perfect parameter knowledge. The sensitivities of the model-based approaches to errors in the model parameters is then examined. An estimator is designed to determine the wind speed from return wavefront measurements. Finally, the alternative systems are compared with errors in the model parameters and the use of the estimator to determine the wind speed.

Chapter 2 derives simple scaling laws for thermal blooming and defines basic nomenclature for adaptive optics and thermal blooming. The mathematics behind the classical "bending into the wind" shape of a thermally bloomed wave is explained and equal intensity profiles are plotted. The important relationship between intensity and wavefront error is examined. Finally, the Zernike representation of two dimensional surfaces is defined.

Chapter 3 describes the thermal blooming model used for the remainder of the research. The model is a function of nineteen atmospheric, laser, and target parameters. Atmospheric parameters include wind speed, air density, and absorption coefficients. Laser parameters include aperture radius, power, and wavelength. Target parameters describe the target's position and velocity. The model produces peak intensity and the laser profile on target in terms of four Zernike modes: focus, astigmatism, coma, and spherical.

Chapter 4 describes the model of atmospheric turbulence. Only six parameters are needed to compute the turbulence distortion: transverse wind velocity, transverse target velocity, target distance, Kolmogorov turbulence constant, the laser wavelength, and aperture radius. The model describes the turbulence aberration in terms of the first twenty Zernike modes.

Chapter 5 describes the traditional control strategies for a high-energy laser: open loop and phase conjugation, and compares their performance with two model-based approaches: optimal focus correction and optimal power with optimal focus correction. The performance of the four systems is compared during light, moderate, and heavy thermal blooming scenarios. In this chapter, the model parameters are perfectly known so that an upper bound for the novel, model-based control techniques can be established.

Chapter 6 discusses the sensitivity of the model-based techniques to errors in the model parameters. The majority of parameters are atmospheric constants that can be measured at the start of the day or entered from a table. However, the transverse wind speed and the transverse and axial target speed and distance will continuously change. It is assumed that a radar system provides target information, so wind speed is the only parameter that is not accurately known. The second part of Chapter 6 constructs an extended Kalman filter to

estimate the wind speed from return wavefront Zernike coefficients and evaluates the performance of the estimator with and without model parameter errors.

Chapter 7 compares the four control strategies once again, but instead of having perfect parameter knowledge, errors are introduced into the model parameters. The estimator designed in Chapter 6 is used to estimate the wind speed. The performance of the various control techniques is compared using the same light, moderate, and heavy thermal blooming scenarios that are presented in Chapter 5.

Chapter 8 presents the conclusions of this design effort and makes recommendations for extensions on the current design and future research.

Chapter 2

Mathematical Foundation of Thermal Blooming

Thermal blooming of high energy lasers is a beam-spreading effect that can significantly reduce the effectiveness of laser systems both as directed energy weapons and as remote powering devices. When a high energy laser propagates through a medium, a portion of the laser energy is absorbed by the medium. This absorbed power heats the medium causing it to expand, changing its index of refraction.

Thermal blooming is classified by the form of heat transfer that balances the absorbed power. The three cases are thermal conduction, natural convection, and forced convection [2]. Thermal conduction occurs when there is no relative motion between the beam and the medium and when no natural convective velocities are established. Natural convection results when the absorbed power causes gas heating, which establishes convection currents. By far the most important continuous wave case is convection forced by wind and beam slewing.

This chapter derives simple scaling laws for thermal blooming and define basic nomenclature for adaptive optics and thermal blooming. The classical "bending into the wind" shape of a thermally bloomed wave will be pictured. Additionally, the important

relationship between intensity and wavefront error will be examined. Finally, the representation of two-dimensional wavefronts by Zernike polynomials will be introduced.

2.1 ANALYTIC DERIVATION OF THERMAL BLOOMING EQUATIONS

Thermal blooming is a highly nonlinear phenomenon. A simple method for analyzing the effects of thermal blooming is to start with the general wave optics equations and find a perturbation solution [10]. The following equations completely specify steady-state thermal blooming in the ray optics limit.

Intensity, I , is given by

$$\text{div}(I\vec{s}) = -\alpha I \quad (2.1)$$

which can be expanded into

$$\vec{s} \cdot \text{grad}I + I \cdot \text{div}(\vec{s}) = -\alpha I \quad (2.2)$$

\vec{s} is the unit vector denoting the direction of propagation.

α is the linear loss coefficient due to absorption in the medium.

\vec{s} can be determined by

$$\frac{d}{ds}(\text{grad}S) = \text{grad}\mu \quad (2.3)$$

S is the eikonal.

μ is the index of refraction.

S and \vec{s} are related by

$$\mu \vec{s} = \text{grad} S \quad (2.4)$$

Using Equation 2.4 and the definition of S

$$\text{div}(\vec{s}) = \text{div}\left(\frac{\text{grad} S}{\mu}\right) \quad (2.5)$$

Substituting into Equation 2.2 gives

$$\left(\frac{\text{grad} S}{\mu}\right) \cdot \text{grad} I + \frac{I}{\mu} \text{div}(\text{grad} S) = -\alpha I \quad (2.6)$$

and using Equation 2.3

$$\frac{I}{\mu} \left(\int \text{grad} \mu \cdot d\vec{s} \right) \cdot \text{grad} I + \frac{I}{\mu} \text{div} \left(\int \text{grad} \mu \cdot d\vec{s} \right) = -\alpha I \quad (2.7)$$

2.2 APPROXIMATIONS TO STEADY-STATE THERMAL BLOOMING

For thermal blooming problems, it is useful to divide the derivatives into axial directions, with z as the direction of propagation and t as the transverse direction

$$\nabla \equiv \frac{\partial}{\partial z} \hat{z} + \nabla_t \hat{r} \quad (2.8)$$

In arriving at a more useful expression it is customary to assume ray optics (or geometrical optics, i.e. the branch of optics that neglects the wavelength, corresponding to the limiting case as $\lambda \rightarrow 0$), neglect diffraction effects in the axial direction, and use the paraxial ray approximation [2]. The paraxial ray approximation uses dz in place of $d\vec{s}$ for the integration path. These assumptions result in

$$\int \nabla_t \mu dz \cdot \nabla_t I + \int \nabla_z \mu dz \cdot \nabla_z I + \frac{I}{\mu} \int \nabla_t^2 \mu dz = -\alpha I \quad (2.9)$$

or in integral form

$$\frac{I(r,z)}{I(r,0)} = \exp \left[-\alpha z - \int_0^z \left(\nabla_t + \frac{\nabla_t I}{I} \right) \cdot \int_0^{z'} \frac{\nabla_t \mu}{\mu_0} dz'' dz' \right] \quad (2.10)$$

Because thermal blooming results from absorbed laser power changing the index of refraction of the medium, this relationship is now examined. The Dale Gladstone Law relates the density of a gas to its index of refraction

$$\mu - 1 = K_p \rho \quad (2.11)$$

ρ is the density of the gas.

K_p is a constant for the gas, equal to $\frac{2}{3}$ the polarizability of the molecule or atom.

The Ideal Gas Law relates pressure, density, and temperature

$$P = \rho RT \quad (2.12)$$

P is the pressure. R is the gas constant. T is the temperature.

For steady-state isobaric conditions, the temperature change due to energy absorption is determined from the energy balance equation

$$\rho c_p \vec{v} \cdot \text{grad} T - K_T \nabla^2 T = \alpha I \quad (2.13)$$

c_p is the specific heat at constant pressure. \vec{v} is the gas velocity. K_T is the thermal conductivity.

Finally μ_T is defined as the rate of change of the index of refraction of the gas with respect to temperature at constant pressure

$$\text{grad}\mu = K\text{grad}\rho = \text{grad}T\left(\frac{\partial\mu}{\partial T}\right) = \mu_T\text{grad}T. \quad (2.14)$$

In this study the most common type of thermal distortion is examined, the wind dominated case. For a collimated (or unfocused) beam with a uniform wind from the x-direction, the energy equation is

$$\rho c_p v \frac{\partial T}{\partial x} = -\alpha I \quad (2.15)$$

After integration this becomes

$$T - T_0 = \frac{\alpha}{\rho c_p v} \int_{-\infty}^x I dx' \quad (2.16)$$

The intensity expression is then given by [2]

$$\frac{I(r, z)}{I(r, 0) \exp(-\alpha z)} = \exp \left\{ \frac{-\mu_T \alpha}{\mu \rho c_p v} \int_0^z \int_0^{z'} \left[\frac{\partial I}{\partial x} + \frac{1}{2} \frac{\partial^2}{\partial y^2} \int_{-\infty}^x I dx' + \frac{1}{2I} \frac{\partial I}{\partial y} \int_{-\infty}^x \frac{\partial I}{\partial y} dx' \right] dz' dz'' \right\} \quad (2.17)$$

The expression can be evaluated for an initially Gaussian beam and expressed in terms of the distortion parameter N_c defined below

$$\frac{I(x, y, z)}{I(x, y, 0) \exp(-\alpha z)} = \exp \left\{ -N_c \left[\frac{x}{a} e^{-\left(\frac{x^2+y^2}{a^2}\right)} + \frac{\sqrt{\pi}}{2} e^{\left(\frac{-y^2}{a^2}\right)} \left(1 - \frac{2y^2}{a^2} \right) \left(1 + \text{erf} \frac{x}{a} \right) \right] \right\} \quad (2.18)$$

$$N_c \equiv \frac{-\mu_T I_0 \alpha z^2}{\mu \rho c_p v a} \left[\frac{2}{\alpha z} - \frac{2}{(\alpha z)^2} (1 - e^{-\alpha z}) \right] \quad (2.19)$$

a is the $\frac{1}{e}$ beam radius for a Gaussian beam.

For a distortion parameter of 1, the wavefront of a steady-state bloomed wave is shown in Figure 2.1. Equal intensity contours of the steady-state bloomed wave are pictured as well. Note that the peak intensity is deflected into the wind which is incident from the left.

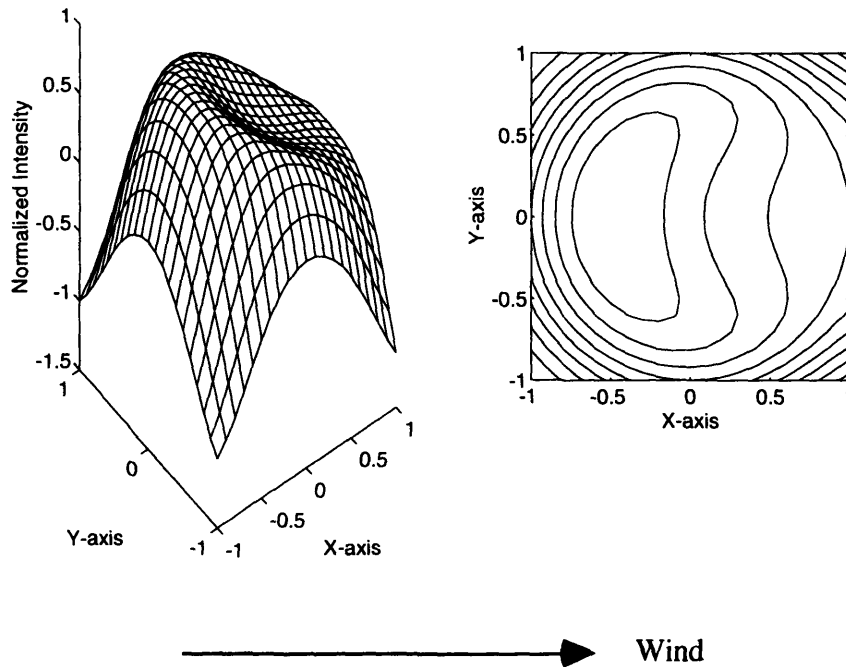


Figure 2.1. Wavefront and Equal Intensity Contours for a Thermally Bloomed Wave.

2.3 RELATIONSHIP BETWEEN PHASE ERROR AND INTENSITY

Adaptive optics systems attempt to increase the intensity on target by reducing the standard deviation of the wavefront distortion, also referred to as the wavefront error or the rms phase error. The relationship between wavefront error and intensity is now examined. Consider the coordinate system given in Figure 2.2.

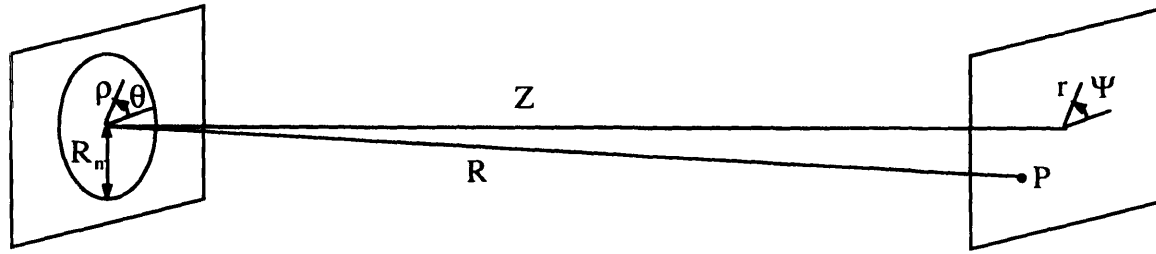


Figure 2.2. Coordinate System for Intensity Equations.

The intensity of light at a point P on the focal plane a distance z away is given by [10]

$$I(P) = \left(\frac{AR_m^2}{\lambda R^2} \right)^2 \left| \int_0^{2\pi} \int_0^1 \exp \left(i \left(k\Phi - v\rho \cos(\theta - \psi) - \frac{1}{2}u\rho^2 \right) \right) \rho d\rho d\theta \right|^2 \quad (2.20)$$

$\frac{A}{R}$ is the electric field amplitude and $\left(\frac{A}{R} \right)^2$ is the intensity in the pupil plane.

The pupil coordinates are ρ and θ , its radius is R_m .

The image coordinates are r and ψ , normalized to $u = \frac{2\pi}{\lambda} \left(\frac{R_m}{R} \right)^2 z$ and

$$v = \frac{2\pi}{\lambda} \left(\frac{R_m}{R} \right) r.$$

λ is the wavelength.

R is the slant angle from the center of the pupil to the point P.

$k\Phi$ is the phase deviation and represents the aberrations in the wave.

In the absence of aberrations, the intensity is maximum on axis. Increasing the aperture, decreasing the wavelength or decreasing the propagation distance increases the intensity in the focal plane.

$$I_{\Phi=0}(P_{r=0}) = \left(\frac{AR_m^2}{\lambda R^2} \right) \pi^2 = \left(\frac{\pi^2 R_m^4}{\lambda^2 R^2} \right) I_{z=0} \quad (2.21)$$

The Strehl ratio [10] is the ratio between the on-axis intensity of an aberrated beam and an unaberrated beam. The goal of an adaptive optics system is to increase the Strehl ratio

towards one, the ideal diffraction limited case. Using Equations 2.10 and 2.21, removing tilt, and displacing the focal plane to its Gaussian focus results in the following simplification

$$SR = \frac{I(P_{r=0})}{I_{\Phi=0}(P_{r=0})} = \frac{1}{\pi^2} \left| \int_0^{2\pi} \int_0^1 \exp(ik\Phi_p) \rho d\rho d\theta \right|^2 \quad (2.22)$$

Φ_p represents the aberrations centered about a sphere with respect to the point P.

For small wavefront aberration, it can be shown [10] that the Strehl ratio is closely related to the wavefront variance, $(\Delta\Phi_p)^2$

$$SR \approx 1 - \left(\frac{2\pi}{\lambda} \right)^2 (\Delta\Phi_p)^2 \quad (2.23)$$

$$(\Delta\Phi_p)^2 = \frac{\int_0^{2\pi} \int_0^1 (\Phi_p - \overline{\Phi_p})^2 \rho d\rho d\theta}{\int_0^{2\pi} \int_0^1 \rho d\rho d\theta} \quad (2.24)$$

$\overline{\Phi_p}$ is the average wavefront.

By reducing the wavefront variance it is possible to increase the Strehl ratio and accordingly the intensity on target. Figure 2.3 demonstrates the dependence of the Strehl ratio on wavefront error.

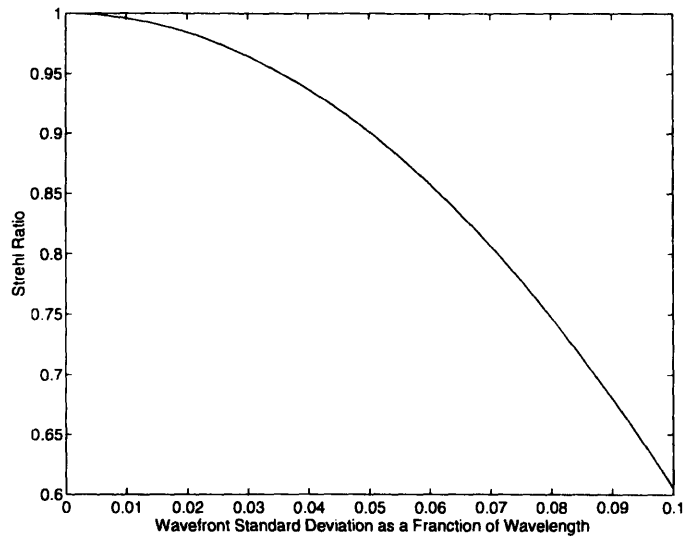


Figure 2.3 Strehl Ratio as a Function of Wavefront Error.

2.4 INTRODUCTION TO ZERNIKE POLYNOMIALS

A number of mathematical constructs are used to represent two dimensional wavefronts. Because many apertures and lenses are round, it is standard to use polar coordinates. The wavefront can be represented by a power series in polar coordinates [10]. However, the power series representation is not orthogonal over the unit circle. Zernike introduced a series of functions that are orthonormal over the unit circle and closely related to the classical aberrations of tilt, focus, astigmatism, and coma. Appendix A defines and plots the first twenty Zernike polynomials.

2.5 SUMMARY

In this chapter simple thermal blooming scaling laws were presented. The asymmetrical intensity pattern, bending into the wind, was derived and pictured. The important relationship between intensity and wavefront error was explained. This relationship is the basis for adaptive optics systems. By predistorting the outgoing laser wavefront to reduce

the wavefront error, intensity on target is increased. Finally, the Zernike method of representing two dimensional wavefronts was introduced. For the rest of the thesis, wavefronts are described in terms of their Zernike coefficients.

Chapter 3

Thermal Blooming Model

This chapter describes the thermal blooming model which is used for the remainder of the research. Unlike the equations developed in the previous chapter which considered collimated beams, the following model allows for the beam to be focused. Additionally, turbulence can easily be added to provide a more accurate description of the laser propagation. In Chapter 6, an extended Kalman filter is designed to estimate wind speed from return wavefront measurements. The relationship between wind speed and thermal blooming Zernike coefficients is described.

3.1 THERMAL BLOOMING MODEL PARAMETERS

The model was created by fitting scaling laws to a large body of data provided to Draper Laboratory by the Naval Research Laboratory. The data was generated by atmospheric propagation simulations using finite-difference wave-optics code [11]. Specific details describing the wave-optics code are unavailable. A total of nineteen parameters describe the thermal blooming process. The first eight parameters can be classified as atmospheric parameters and include wind speed, air density, and absorption coefficients. The next seven parameters describe the laser including aperture radius, power and wavelength. The

final four parameters are engagement-specific and describe the target's position and velocity. All of the parameters are listed in the table below along with their symbol and nominal value.

TABLE 3.1. Thermal Blooming Model Parameters.

| Parameter Description | Symbol | Nominal Value |
|----------------------------|---------------------------------|--|
| Transverse Wind Velocity | U_w | $7 \frac{m}{s}$ |
| Turbulence Constant | C_N^2 | $1 \times 10^{-15} m^{-\frac{2}{3}}$ |
| Absorption Coefficient | α | $2 \times 10^{-5} \frac{1}{m}$ |
| Scattering Coefficient | σ | $1 \times 10^{-5} \frac{1}{m}$ |
| Refractive Index | n_∞ | 1 |
| Refractive Index Gradient | $\frac{\partial n}{\partial T}$ | $-1.4 \times 10^{-5} \frac{1}{\text{Deg C}}$ |
| Air Density | ρ | $17.9 \frac{kg}{m^3}$ |
| Specific Heat | C_p | $860 \frac{J}{kg \text{ Deg C}}$ |
| Aperture Radius | R_m | .35m |
| Laser Power | P | $4 \times 10^5 W$ |
| Transmission | T | 1 |
| Wavelength | λ | $3.8 \times 10^{-6} m$ |
| Beam Quality | M | 1.4 |
| Beam Spread due to Jitter | σ_j^2 | $2 \times 10^{-11} \text{ rad}$ |
| Beam Spread due to Wander | σ_w^2 | $1 \times 10^{-11} \text{ rad}$ |
| Transverse Target Velocity | U_{TX} | $100 \frac{m}{s}$ |
| Axial Target Velocity | U_{TY} | $100 \frac{m}{s}$ |
| Target Distance | Z_T | 5000m |
| Focal Length | Z_F | 5000m |

3.2 PEAK INTENSITY

The purpose of a directed energy system is to deliver energy to a target. A standard measurement of the effectiveness of such a system is intensity - energy per unit time across a unit area - on target. Peak intensity on target is modeled as

$$I_p = \frac{PT}{\pi Z_T^2 \sigma^2} \quad (3.1)$$

σ^2 is the radial beam spread due to all dispersive effects.

Figure 3.1 shows the effects of beam spreading. Instead of focusing to a point, diffraction and other linear effects increase the spot size. Blooming causes a further increase, and as a result, decreases the intensity on target.

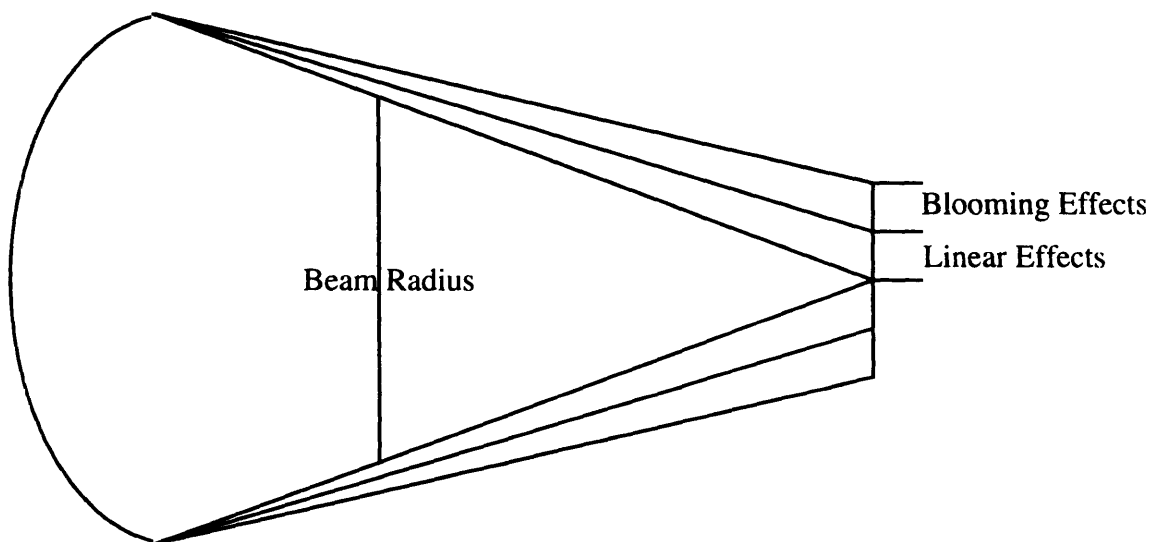


Figure 3.1. Effects of Diffraction and Thermal Blooming on Beam Spreading.

Dispersive effects can be divided into two categories - random linear effects and deterministic nonlinear effects. Random linear effects are independent and it is possible to

compensate for them with simple linear methods, such as phase conjugation. Distortions applied at the laser aperture do not feedback and change the linear effects. Linear effects include diffraction, high-frequency turbulence, high-frequency jitter, and low-frequency wander. The dispersions caused by random linear effects simply root-sum-square together as shown in Equation 3.3. It is not possible to compensate for nonlinear effects using linear methods. Distortions applied at the laser aperture do feedback and change nonlinear effects. The nonlinear effects include applied focus and thermal blooming. Equation 3.4 shows how their dispersions combine. As the name indicates, these effects are deterministic. It is possible to determine the distortion caused by thermal blooming if all of the parameters in Table 3.1 are known.

$$\sigma^2 = \sigma_L^2 + \sigma_R^2 \quad (3.2)$$

$$\sigma_L^2 = \sigma_D^2 + \sigma_T^2 + \sigma_J^2 + \sigma_W^2 \quad (3.3)$$

$$\sigma_R^2 = \sigma_F^2 + 2\sigma_F\sigma_B + \sigma_B^2 \quad (3.4)$$

The ratio of bloomed to unbloomed intensity on target can be modeled as

$$\frac{I_B(P)}{I_U(P)} = \frac{\sigma_L^2}{\sigma_L^2 + \sigma_B^2} \quad (3.5)$$

σ_L^2 is the beam dispersion in radians due to linear effects.

σ_B^2 is the beam dispersion in radians due to thermal blooming.

The blooming dispersion is a function of power. For power levels of interest, the following form is suggested [12]

$$\sigma_B^2 = C_B P^a \quad (3.6)$$

where a is a constant greater than 1, equal to 1.1777 for a uniform beam, and

C_B is a dimensionless coefficient dependent upon beam shape to be defined later.

3.3 CRITICAL POWER

The phenomenon of critical power - that there is a maximum intensity deliverable on target - can be deduced from the above equations. If the power of the laser is increased beyond the critical power, P_C , the intensity on target will actually decrease.

$$I_U(P) \propto P \quad (3.7)$$

$$I_B(P) = I_U(P) \frac{I_B(P)}{I_U(P)} \propto \frac{P\sigma_L^2}{\sigma_L^2 + C_B P^a} \quad (3.8)$$

Differentiating this expression with respect to P_C and setting the derivative to zero results in an expression for P_C

$$\frac{(\sigma_L^2 + C_B P_C^a)\sigma_L^2 - P_C\sigma_L^2 a C_B P_C^{a-1}}{(\sigma_L^2 + C_B P_C^a)^2} = 0$$

$$P_C = \left(\frac{\sigma_L^2}{(a-1)C_B} \right)^{\frac{1}{a}} \quad (3.9)$$

Power-Intensity curves are shown in Figure 3.2 for three wind speeds. Notice how the critical power increases with wind speed. As the wind speed increases the beam path is cooled more rapidly. As a result, more laser power can be used before the effects of thermal blooming dominate. With strong winds, the effect of thermal blooming is greatly decreased.

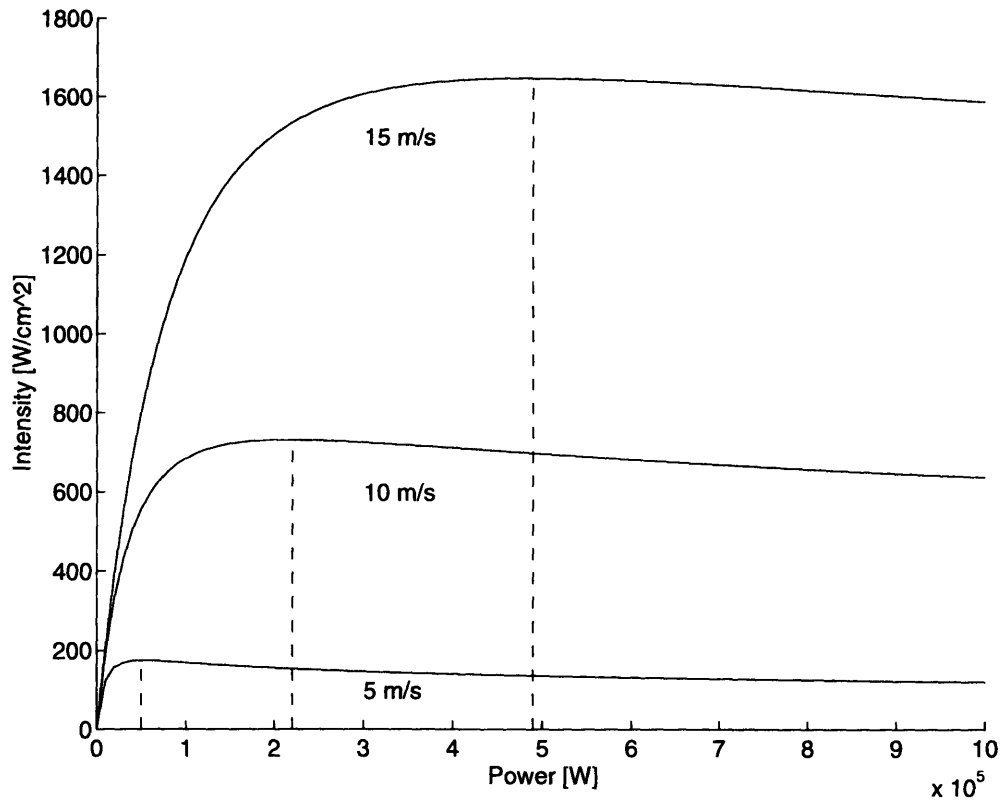


Figure 3.2. Intensity as a Function of Laser Power for Various Wind Speeds.

3.4 DISPERSIVE EFFECTS

3.4.1 RANDOM LINEAR EFFECTS

Diffraction, turbulence, jitter and wander all contribute to the beam spreading pictured in Figure 3.1. The formulae for diffraction and turbulence can be computed as functions of the parameters given in Table 3.1. The diffraction contribution, σ_D^2 , is a function of wavelength, aperture radius, beam quality, and beam shape [12].

$$\sigma_D^2 = 0.5 \left(\frac{m' M \lambda}{2R_m} \right)^2 \quad (3.10)$$

where m' is a beam shape dependent coefficient, equal to $\frac{\pi}{2}$ for an infinite Gaussian beam, 0.9166 for a truncated Gaussian beam, and 0.9202 for a uniform beam.

The turbulence contribution, σ_T^2 , is a function of wavelength, aperture radius, beam quality, beam shape, the turbulence constant, and the target distance [13].

$$\sigma_T^2 = \begin{cases} 0.182 \left(\frac{\sigma_D}{M} \right)^2 \left(\frac{D_e}{r_0} \right)^2 & \text{for } \frac{D_e}{r_0} < 3 \\ \left(\frac{\sigma_D}{M} \right)^2 \left[\left(\frac{D_e}{r_0} \right)^2 - 1.18 \left(\frac{D_e}{r_0} \right)^{\frac{5}{3}} \right] & \text{for } \frac{D_e}{r_0} > 3 \end{cases} \quad (3.11)$$

where r_0 is the Fried coherence length

$$r_0 = 2.10 \left[1.45 \left(\frac{2\pi}{\lambda} \right)^2 \int_0^{Z_t} c_n^2(z) \left(\frac{Z_t - Z}{Z_t} \right) dz \right]^{\frac{3}{5}} \quad (3.12)$$

and D_e is the effective aperture size, equal to $2.83R_m$ for an infinite Gaussian beam, $1.92R_m$ for a truncated Gaussian beam, and $2R_m$ for a uniform beam.

The turbulence equations are valid when turbulence is small enough not to cause speckling, $\sigma_T < 2\sigma_D$.

Jitter and wander are hardware dependent and must be determined by other means.

3.4.2 DETERMINISTIC NONLINEAR EFFECTS

The two deterministic effects are applied focus and thermal blooming. The focus dispersion is given by [14]

$$\sigma_F = \sqrt{\frac{1}{2}} (1 - N_R) \frac{R_m}{Z_T} \quad (3.13)$$

where N_R is the ratio of target range to focal range.

The physical phenomenon that causes thermal blooming is an accumulation of phase due to heating along the range. Blooming increases with power and decreases with the portion of σ_L^2 that experiences the heating, $\sigma_L^2 - \sigma_w^2$. The heating phase or phase integral, Ψ_h , represents the accumulation along the range of phase perturbation due to heating. It has been found to closely model the thermal blooming dispersion [14]

$$\sigma_B^2 = C_B' (\sigma_L^2 - \sigma_w^2) \Psi_h^u \quad (3.14)$$

where C_B' is a coefficient that depends on beam shape: equal to 0.010590 for an infinite Gaussian beam, 0.028727 for a truncated Gaussian beam, and 0.014264 for a uniform beam.

Referring back to (3.6),

$$C_B = C_B' (\sigma_L^2 - \sigma_w^2) \left(\frac{\Psi_h}{P} \right)^u. \quad (3.15)$$

3.4.3 HEATING PHASE

A number of authors derive scaling laws for the heating phase [14,15,16]. The starting point for each procedure is the same.

$$\Psi_h = \int_0^l \Psi_h(z) dz \quad (3.16)$$

$$z = \frac{Z}{Z_t} \quad (3.17)$$

$$\Psi_h(z) = \frac{N_D N_F e^{-\epsilon z} \int I[x_0(z,t), y_0(z,t)] dt}{N_Q \left[\frac{R_s(z)}{R_m} \right]^2 \left(\frac{2R_m}{U_w} \right) \left(\frac{P}{\pi R_m^2} \right)} \quad (3.18)$$

N_D is the distortion number

$$N_D = -2 \left(\frac{\partial n}{\partial T} \right) \frac{P Z_f^2 \alpha}{R_m^3 U_w C_p \rho n_\infty} \quad (3.19)$$

N_F is the Fresnel number

$$N_F = \frac{2\pi R_m^2}{\lambda Z_f} \quad (3.20)$$

N_Q' is the modified effective beam quality

$$N_Q' = \frac{\sqrt{\sigma_L^2 - \sigma_w^2}}{\frac{\sigma_D}{M}} \quad (3.21)$$

$e^{-\epsilon Z}$ represents extinction along the propagation path.

$R_s(Z)$ approximates the spot radius by considering focus and diffraction effects

$$R_s(z) = R_m \sqrt{(1-z)^2 + \left(\frac{2zN_Q}{N_F} \right)^2} \quad (3.22)$$

$\frac{2R_m}{U_w}$ is the clearing time at the aperture.

$\frac{P}{\pi R_m^2}$ is a normalization for the intensity.

x_0 and y_0 are normalized coordinates of a point in the focal plane.

A general and complete approximation for the heating phase is [14]

$$\Psi_h = \left[\frac{N_D N_F N_R}{N_Q \gamma} \right] \left\{ \ln_0 - (1 - e^{-\epsilon Z_1}) \ln_{\frac{N_R}{2}} - e^{-\epsilon Z_1} \ln_{N_R} \right\} \quad (3.23)$$

N_Q is the effective beam quality

$$N_Q = \frac{\sqrt{m^2 \sigma_D^2 + \sigma_T^2 + \sigma_J^2}}{\frac{\sqrt{.5\lambda m'}}{\pi R_m}} \quad (3.24)$$

m and m' are coefficients dependent upon beam shape: equal to 2.0 and 1.0 for an infinite Gaussian beam, 4.0 and 0.8893 for a truncated Gaussian beam, and 1.0 and 1.124 for a uniform beam

$$\varepsilon = \alpha + \sigma \quad (3.25)$$

$$\ln_z = \ln \left| \frac{\left[-N_S - N_R + \left(\frac{2N_Q}{N_F} \right)^2 N_R \right] z + N_S + N_R + \gamma \sqrt{(1-z)^2 + \left(\frac{2zN_Q}{N_F} \right)^2}}{(zN_S + N_R)} \right| \quad (3.26)$$

where

$$N_S = \frac{U_T}{U_w} \quad (3.27)$$

3.5 PARAMETERIZATION OF ABERRATED BEAM

The standard method for parameterizing a beam is in terms of Zernike coefficients

$$\Psi(r, \theta) = \sum_{i=1}^N C_i \cdot P_i(r, \theta) \quad (3.28)$$

This section describes the four basic optical modes and the method used to calculate the corresponding Zernike coefficients.

The wavefront aberration at the target is a combination of aberration applied at the aperture and aberration acquired along the propagation path. For small total aberrations this becomes

$$\sigma_{Ri} = \sigma_{Fi} + \sigma_{Bi} \quad (3.298)$$

σ_{Fi} are the applied aberration dispersions: $i=1,2$ for X-axis and 3,4 for Y-axis

σ_{Bi} are the blooming dispersions expressed in terms of the parameter σ_B [11]

$$\sigma_{B1} = 0 \quad (3.30)$$

$$\sigma_{B2} = \sigma_B \quad (3.31)$$

$$\sigma_{B3} = \sigma_{B4} = \frac{\sigma_B}{\sqrt{2}} \quad (3.32)$$

In Chapter 6, an extended Kalman filter is designed to estimate wind speed from return wavefront measurements. The return wavefront is decomposed in a Zernike polynomial expansion. The Kalman filter uses the focus, astigmatism, coma, and spherical coefficients. The relationship between wind speed and these coefficients is now examined. Equations 3.6 and 3.15 show that σ_B^2 is proportional to Ψ_h^a . Equation 3.23 shows that wind speed enters into Ψ_h in several ways, but primarily through the denominator of the distortion number, N_D . As a result, an increasing wind speed will decrease σ_B . Equations 3.29-3.31 show how σ_B is related to the four blooming dispersions. The next four sections will show these dispersions are related to the relevant Zernike coefficients. Appendix B shows how the focus and astigmatism Zernike coefficients vary as a function of the atmospheric and target parameters. The relationship between wind speed and Zernike coefficients is shown in Figure B.1.

3.5.1 FOCUS

Focus aberration is caused by all rays converging to a single point. The corresponding Zernike coefficient is proportional to the sum of the dispersion parameters.

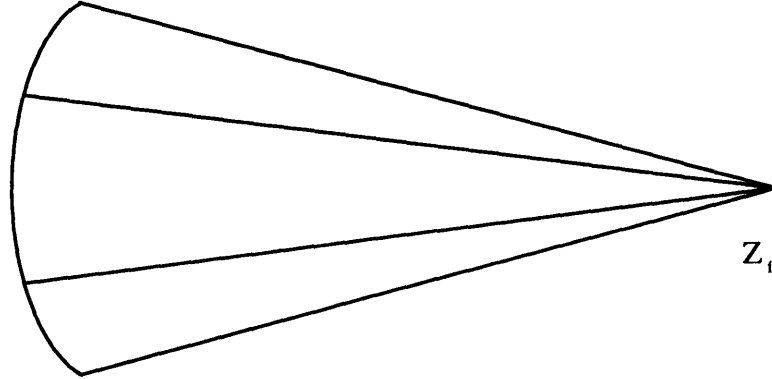


Figure 3.3. Ray Diagram for Focus Aberration.

$$C_3 = \alpha_3(\sigma_{R1} + \sigma_{R2} + \sigma_{R3} + \sigma_{R4}) \quad (3.33)$$

The proportionality constant is a function of beam shape. For a uniform beam, the following form is suggested [17]

$$\alpha_i = \left[\sigma_D k \left(\int P_i^2 r \, dr \, d\theta \right)^{\frac{1}{2}} \right]^{-1} \quad (3.34)$$

$$\int P_3^2 r \, dr \, d\theta = \int_0^{2\pi} \int_0^1 (4r^5 - 4r^3 + r) \, dr \, d\theta = \frac{\pi}{3} \quad (3.35)$$

3.5.2 ASTIGMATISM

Astigmatism aberration is caused by having two focal lengths, one for the x-axis and one for the y-axis. The corresponding Zernike coefficient is proportional to the difference between the x and y dispersions.

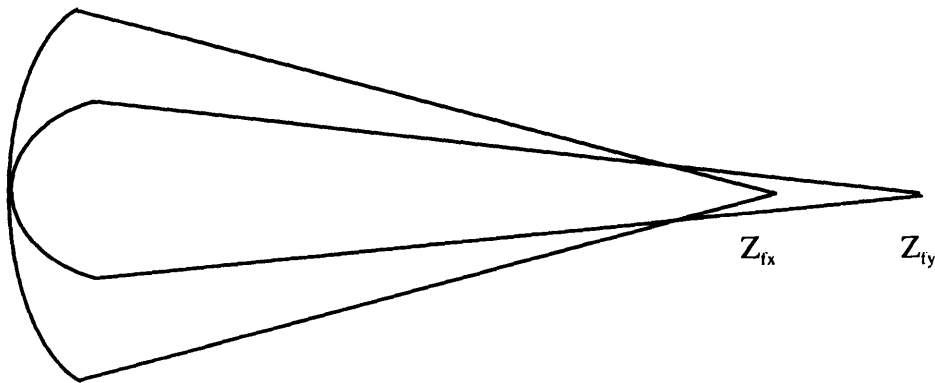


Figure 3.4. Ray Diagram for Astigmatism Aberration.

$$C_4 = \alpha_4 (\sigma_{R1} + \sigma_{R2} - \sigma_{R3} - \sigma_{R4}) \quad (3.36)$$

$$\int P_4^2 r \, dr \, d\theta = \int_0^{2\pi} \int_0^1 r^5 \cos^2 2\theta \, dr \, d\theta = \frac{\pi}{5} \quad (3.37)$$

3.5.3 COMA

Coma aberration is caused by having the focal length be a function of the x-position. There is a dissimilarity between the maximum and minimum focal ranges on one of the axes.

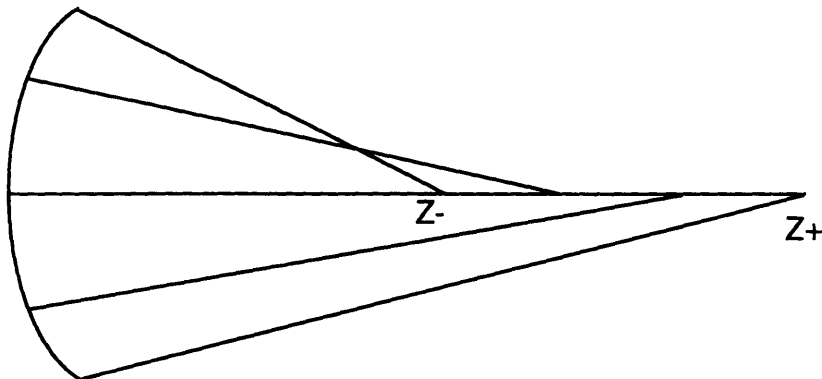


Figure 3.5. Ray Diagram for Coma Aberration.

$$C_6 = \alpha_6 (\sigma_{R1} - \sigma_{R2} - \sigma_{R3} + \sigma_{R4}) \quad (3.38)$$

$$\int P_6^2 r dr d\theta = \int_0^{2\pi} \int_0^1 (9r^7 - 6r^5 + 4r^3) \cos^2 \theta dr d\theta = \frac{35\pi}{24} \quad (3.39)$$

3.5.4 SPHERICAL

Spherical aberration is caused by having the focal length be a function of the radius. There is an axially symmetric dissimilarity between the maximum and minimum focal ranges.

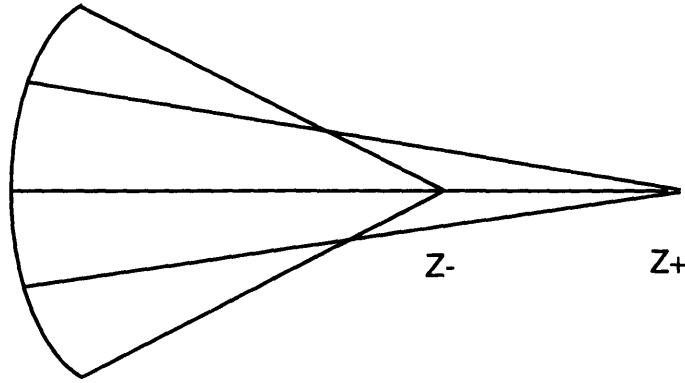


Figure 3.6. Ray Diagram for Spherical Aberration.

$$C_{10} = \alpha_{10} (\sigma_{R1} - \sigma_{R2} + \sigma_{R3} - \sigma_{R4}) \quad (3.40)$$

$$\int P_{10}^2 r dr d\theta = \int_0^{2\pi} \int_0^1 (36r^9 - 24r^7 + 48r^5 - 12r^3 + r) dr d\theta = \frac{251\pi}{35} \quad (3.41)$$

3.6 SIMULATIONS

The thermal blooming model produces Zernike coefficients for focus, astigmatism, coma, and spherical modes. The following sets of figures show two typical thermal blooming wavefronts at the target, no atmospheric turbulence is added.

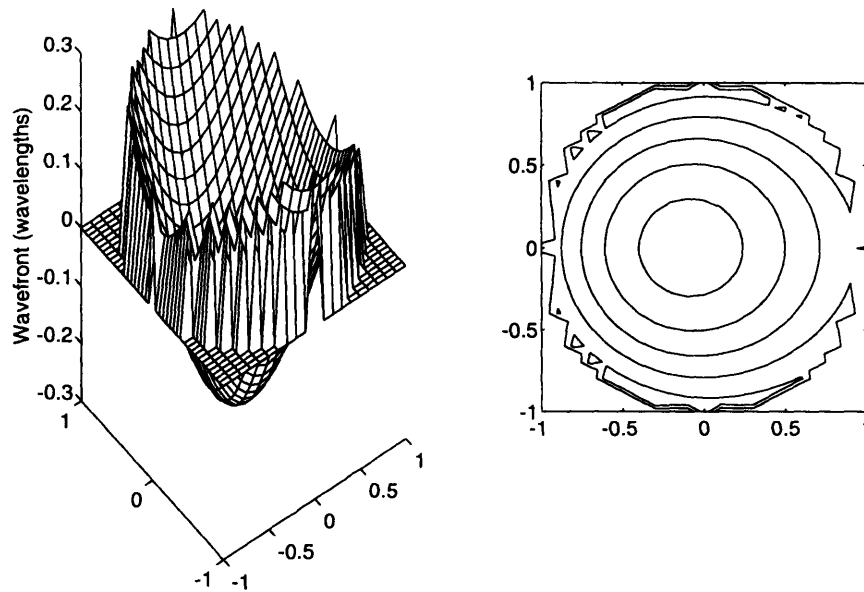


Figure 3.7. Typical Wavefront for Light Thermal Blooming.

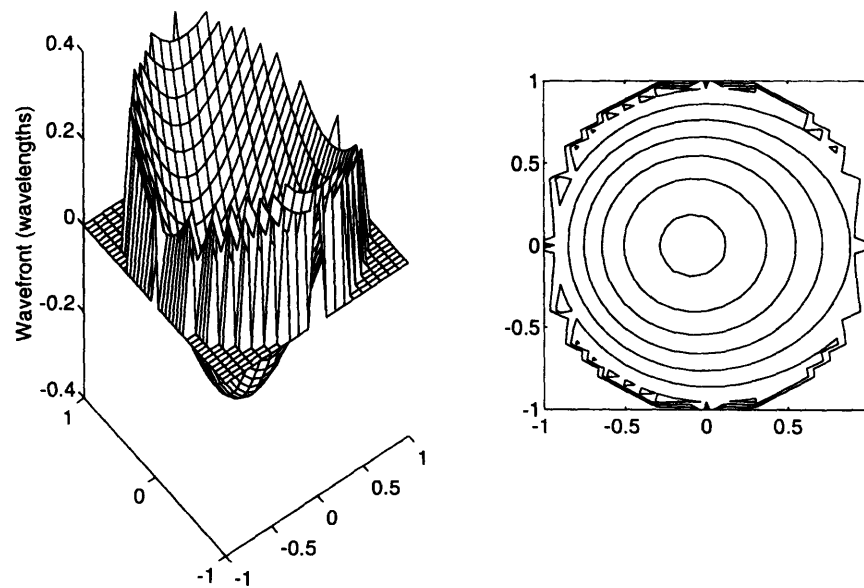


Figure 3.8. Typical Wavefront for Heavy Thermal Blooming.

3.7 SUMMARY

In this chapter a model for thermal blooming was presented. At the heart of the model is data generated by a wave optics code at the Naval Research Laboratory. Using this data, a number of researchers derived models for thermal blooming in terms of intensity on target and laser wavefront. This chapter brought together equations from a number of these models to create a general thermal blooming model that allows for beam focusing. For inputs, the model takes nineteen atmospheric and target parameters. The primary outputs of the model are peak intensity on target and the laser wavefront. The wavefront is expressed in terms of Zernike coefficients corresponding to the focus, astigmatism, coma, and spherical aberrations.

Chapter 4

Atmospheric Turbulence Model

In addition to thermal blooming, turbulence is an important atmospheric effect that must be considered when evaluating directed energy systems. This chapter presents a dynamic model of atmospheric turbulence represented in terms of twenty Zernike polynomial coefficients. In Chapter 6, an extended Kalman filter will be designed to estimate the wind speed from return wavefront measurements. The Kalman filter does not attempt to estimate turbulence, but instead uses the turbulence distortion to model measurement noise since it is likely the most significant contribution.

4.1 TURBULENCE MODEL PARAMETERS

A total of six parameters describe turbulence. The first two parameters can be classified as atmospheric parameters: wind velocity and the Kolmogorov turbulence structure constant. The next two parameters describe the laser: aperture radius and wavelength. The final two parameters are engagement-specific and describe the target's position and velocity. All of the parameters are listed in the following table along with their symbol and nominal value.

TABLE 4.1. Atmospheric Turbulence Model Parameters

| Parameter Description | Symbol | Nominal Value |
|----------------------------|-----------|--------------------------------------|
| Transverse Wind Velocity | U_w | $7 \frac{m}{s}$ |
| Turbulence Constant | C_N^2 | $1 \times 10^{-15} m^{-\frac{2}{3}}$ |
| Aperture Radius | R_m | .35m |
| Wavelength | λ | $3.8 \times 10^{-6} m$ |
| Transverse Target Velocity | U_{TX} | $100 \frac{m}{s}$ |
| Target Distance | Z_T | 5000m |

4.2 ZERNIKE COEFFICIENT MODELING

Turbulence is a random process that causes the index of refraction of the atmosphere and hence the laser phase profile to be random processes. The phase aberration function, Ψ , can be expressed in terms of Zernike polynomials, P_i , and the corresponding Zernike coefficients, C_i

$$\Psi(r, \theta) = \sum_{i=1}^N C_i \cdot P_i(r, \theta) \quad (4.1)$$

Each Zernike coefficient is modeled as a random process, the output of a linear filter driven by unity variance continuous-time white noise. Linear system theory prescribes how to determine the transfer function of the i^{th} filter, $H_i(j\omega)$, given the desired power spectral density function, $S_{ii}(\omega)$ [18]. The power spectral density function, $S_{ii}(\omega)$, is factored into $S_i(j\omega)S_i(-j\omega)$, where $S_i(j\omega)$ is a stable transfer function. The linear filter transfer function is $S_i(j\omega) = K_i H_i(j\omega)$.

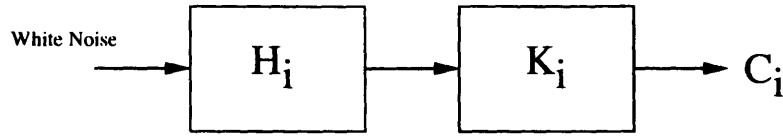


Figure 4.1. Model for Zernike Turbulence Coefficient.

4.2.1 POWER SPECTRAL DENSITY

It has been shown that the power spectral density of the i^{th} Zernike mode is well represented by Equation 4.2 [19].

$$S_{ii}(\omega) = 4\pi^2 k^2 Z_i R_m \int_0^1 \frac{d\eta}{v} \int_{\frac{\omega R}{v}}^{\infty} \xi d\xi \Phi\left(\frac{\xi}{R_m}\right) \frac{|h_i(\alpha, \beta)|^2}{\sqrt{\xi^2 - \left(\frac{\omega R_m}{v}\right)^2}} \quad (4.2)$$

The various functions and parameters used in Equation 4.2 are defined below.

$$\eta = 1 - \frac{z}{Z_T} \quad (4.3)$$

$$\Phi(\xi) = 0.033 C_n^2 \xi^{-\frac{11}{3}} \quad (4.4)$$

$$\alpha = \frac{\omega R_m z}{2\pi v} \quad (4.5)$$

$$\beta = \frac{1}{2\pi} z \sqrt{\xi^2 - \left(\frac{\omega R_m}{v}\right)^2} \quad (4.6)$$

ω is frequency in $\frac{\text{rad}}{\text{s}}$.

z is the along-path distance measurement.

v is the velocity of the beam relative to the air at range z .

h_i is the two-dimensional Fourier transform of the i^{th} Zernike polynomial, given in Table 4.2.

TABLE 4.2. h-Functions

| i | $h_i(\alpha, \beta)$ | i | $h_i(\alpha, \beta)$ |
|-----|--|-----|---|
| 1 | $\frac{\sqrt{2}}{\sqrt{\pi}} \left(\frac{\alpha}{\sigma^2} \right) J_2$ | 11 | $\frac{\sqrt{10}}{\sqrt{\pi}} \left(\frac{\alpha^2 - \beta^2}{\sigma^4} \right) J_4$ |
| 2 | $\frac{\sqrt{2}}{\sqrt{\pi}} \left(\frac{\beta}{\sigma^2} \right) J_2$ | 12 | $\frac{\sqrt{10}}{\sqrt{\pi}} \left(\frac{2\alpha\beta}{\sigma^4} \right) J_4$ |
| 3 | $\frac{\sqrt{3}}{\sqrt{\pi}} \left(\frac{1}{\sigma} \right) J_3$ | 13 | $\frac{\sqrt{10}}{\sqrt{\pi}} \left(\frac{1}{\sigma} - \frac{8\alpha^2}{\sigma^3} + \frac{8\alpha^4}{\sigma^5} \right) J_5$ |
| 4 | $\frac{\sqrt{6}}{\sqrt{\pi}} \left(\frac{\alpha^2 - \beta^2}{\sigma^4} \right) J_4$ | 14 | $\frac{\sqrt{10}}{\sqrt{\pi}} \left(\frac{4\alpha\beta}{\sigma^4} - \frac{8\alpha\beta^3}{\sigma^6} \right) J_5$ |
| 5 | $\frac{\sqrt{6}}{\sqrt{\pi}} \left(\frac{2\alpha\beta}{\sigma^4} \right) J_4$ | 15 | $\frac{\sqrt{12}}{\sqrt{\pi}} \left(\frac{\alpha}{\sigma^2} \right) J_6$ |
| 6 | $\frac{\sqrt{8}}{\sqrt{\pi}} \left(\frac{\alpha}{\sigma^2} \right) J_4$ | 16 | $\frac{\sqrt{12}}{\pi} \left(\frac{\beta}{\sigma^2} \right) J_6$ |
| 7 | $\frac{\sqrt{8}}{\sqrt{\pi}} \left(\frac{\beta}{\sigma^2} \right) J_4$ | 17 | $\frac{\sqrt{12}}{\pi} \left(-\frac{3\alpha}{\sigma^2} + \frac{4\alpha^3}{\sigma^4} \right) J_6$ |
| 8 | $\frac{\sqrt{8}}{\sqrt{\pi}} \left(\frac{3\alpha}{\sigma^2} - \frac{4\alpha^3}{\sigma^4} \right) J_4$ | 18 | $\frac{\sqrt{12}}{\pi} \left(\frac{3\beta}{\sigma^2} - \frac{4\beta^3}{\sigma^4} \right) J_6$ |
| 9 | $\frac{\sqrt{8}}{\sqrt{\pi}} \left(-\frac{3\beta}{\sigma^2} + \frac{4\beta^3}{\sigma^4} \right) J_4$ | 19 | $\frac{\sqrt{12}}{\pi} \left(\frac{5\alpha}{\sigma^2} - \frac{20\alpha^3}{\sigma^4} + \frac{16\alpha^5}{\sigma^6} \right) J_6$ |
| 10 | $\frac{\sqrt{5}}{\sqrt{\pi}} \left(\frac{1}{\sigma} \right) J_5$ | 20 | $\frac{\sqrt{12}}{\pi} \left(\frac{5\beta}{\sigma^2} - \frac{20\beta^3}{\sigma^4} + \frac{16\beta^5}{\sigma^6} \right) J_6$ |

J_i is the i^{th} -order Bessel function of the first kind with argument $2\pi\sigma$ where $\sigma = \sqrt{\alpha^2 + \beta^2}$.

$$J_0(x) = \frac{\sin x}{x}$$

$$J_1(x) = \frac{\sin x}{x^2} - \frac{\cos x}{x}$$

$$J_{n+1}(x) = \frac{2n-1}{x} J_{n-1}(x) - J_{n-2}(x)$$

$$J_n(0) = \begin{cases} 1, & n = 0 \\ 0, & n > 0 \end{cases} \quad (4.7)$$

If the target is stationary, or the transverse velocity component is zero, v is simply equal to the transverse wind velocity, U_w . When the target has a non-zero transverse velocity, v has a component due to the slewing of the beam.

$$v = U_w + U_{TX}(1 - \eta) \quad (4.8)$$

4.2.2 POWER SPECTRAL DENSITY APPROXIMATION

Researchers at TASC numerically evaluated the power spectral density function given in Equation 4.2 and used a straight line approximation to more easily represent the data [18]. The intersections of the line segments are the corner frequencies of the transfer functions and correspond to poles and zeros of the transfer functions. Table 4.3 lists the corner frequencies of the first twenty Zernike modes: f_{1a} , f_{1b} , f_{1d} , and f_{1g} . These modes all have lowpass or bandpass spectra.

TABLE 4.3. Atmospheric Turbulence Scaled Corner Frequencies (Hertz).

| Mode | Spectra | f_{la} | f_{lb} | f_{ld} | f_{lg} |
|------|----------|----------|----------|----------|----------|
| 1 | lowpass | 28.84 | 0.372 | | |
| 2 | lowpass | 28.84 | 0.372 | | |
| 3 | lowpass | 25.12 | 0.214 | | |
| 4 | lowpass | 28.84 | 0.141 | | |
| 5 | bandpass | 50.12 | 0.977 | 0.0051 | .0001 |
| 6 | bandpass | 4.467 | 0.0501 | 0.0117 | .0001 |
| 7 | lowpass | 2.239 | 0.0288 | | |
| 8 | bandpass | 4.169 | 0.0501 | 0.0051 | .0001 |
| 9 | lowpass | 3.388 | 0.0354 | | |
| 10 | lowpass | 3.162 | 0.0436 | | |
| 11 | lowpass | 2.399 | 0.0355 | | |
| 12 | bandpass | 1.698 | 0.0501 | 0.0072 | .0001 |
| 13 | lowpass | 1.819 | 0.0331 | | |
| 14 | bandpass | 1.949 | 0.0468 | .0001 | .0001 |
| 15 | bandpass | 2.754 | 0.0708 | 0.011 | .0001 |
| 16 | lowpass | 1.288 | 0.0309 | | |
| 17 | bandpass | 1.949 | 0.0501 | 0.0048 | .0001 |
| 18 | lowpass | 1.698 | 0.0309 | | |
| 19 | bandpass | 1.698 | 0.0380 | 0.0036 | .0001 |
| 20 | lowpass | 1.819 | 0.0407 | | |

To convert the scaled frequency given in Table 4.3 to actual frequency, it is necessary to use the following transformation

$$f = \left(\frac{U_w}{R_m} \right) f_i \quad (4.9)$$

As described in Section 3.2, the Zernike coefficients are modeled as the output of a linear filter driven by white noise. The transfer functions of the filters are given by

$$H_i(s) = \begin{cases} \frac{1}{(sa_i + 1)(sb_i + 1)}, & i = 1, 2, 3, 4, 7, 9, 10, 11, 13, 16, 18, 20 \\ \frac{sg_i + 1}{(sa_i + 1)(sb_i + 1)(sd_i + 1)}, & i = 5, 6, 8, 12, 14, 15, 17, 19 \end{cases} \quad (4.10)$$

The time constants are given by

$$a_i = \left(\frac{R_m}{U_w} \right) \frac{1}{f_{1a}} \quad (4.11)$$

$$b_i = \left(\frac{R_m}{U_w} \right) \frac{1}{f_{1b}} \quad (4.12)$$

$$d_i = \left(\frac{R_m}{U_w} \right) \frac{1}{f_{1d}} \quad (4.13)$$

$$g_i = \left(\frac{R_m}{U_w} \right) \frac{1}{f_{1g}} \quad (4.14)$$

4.2.3 TRANSFER FUNCTION GAIN

The final step in creating the turbulence model is to determine the appropriate gain for each transfer function. Recalling that the linear filter transfer function is $S_i(j\omega) = K_i H_i(j\omega)$ and

using Parseval's Theorem, the variance of the i^{th} Zernike coefficient is given by

$$\sigma_i^2 = \frac{1}{2\pi} \int_{-\infty}^{\infty} |K_i H_i(\omega)|^2 d\omega = \frac{K_i^2}{2\pi} \int_{-\infty}^{\infty} |H_i(\omega)|^2 d\omega \quad (4.15)$$

So the gain K_i is found to be

$$K_i = \frac{\sigma_i}{\sqrt{\frac{1}{2\pi} \int_{-\infty}^{\infty} |H_i(\omega)|^2 d\omega}} \quad (4.16)$$

The angle variance for X-tilt, Zernike mode 1, is known to be [20]

$$\sigma_\theta^2 = 0.9 c_n^2 \frac{Z_t}{R_m^3} \quad (4.17)$$

Zernike mode 1 is equal to $R_m \theta_x$ so the corresponding variance is

$$\sigma_1^2 = R_m^2 \sigma_\theta^2 = 0.9 c_n^2 Z_t R_m^{\frac{5}{3}} \quad (4.18)$$

The variances for the other Zernike modes can be expressed in terms of the first Zernike mode variance [18].

TABLE 4.4. Zernike Mode Variance Relative to σ_1 .

| Mode | $\frac{\sigma_i}{\sigma_1}$ |
|-------------------|-----------------------------|
| 1,2 | 1.0000 |
| 3 | 0.1957 |
| 4,5 | 0.2768 |
| 6,7,8,9 | 0.1655 |
| 10 | 0.0835 |
| 11,12,13,14 | 0.1181 |
| 15,16,17,18,19,20 | 0.0895 |

Using the values of H_i found in Equation 4.10 and the values of σ_i given in Table 4.4, the gains are

$$K_i(\omega) = \begin{cases} \sigma_i \sqrt{2(a_i + b_i)}, i = 1, 2, 3, 4, 7, 9, 10, 11, 13, 16, 18, 20 \\ \sigma_i \sqrt{\frac{2(a_i + b_i)(a_i b_i + a_i d_i + b_i d_i + d_i^2)}{a_i b_i + a_i d_i + b_i d_i + g_i^2}}, i = 5, 6, 8, 12, 14, 15, 17, 19 \end{cases} \quad (4.19)$$

4.3 Simulations

The following series of figures shows typical turbulence phase distortions. The first figure in each pair corresponds to a stationary target in light winds. The second figure corresponds to a moving target in moderate winds. Figures 4.2 and 4.3 show three-dimensional mesh plots and corresponding two dimensional contour plots of the same wavefront. For both cases, the predominant effect of turbulence is to distort the X and Y tilt of the laser wavefront. This distortion can be countered with appropriate action by the tilt mirror, see Figure 1.1. In further simulations it will be assumed that the X and Y tilt distortions have been corrected.

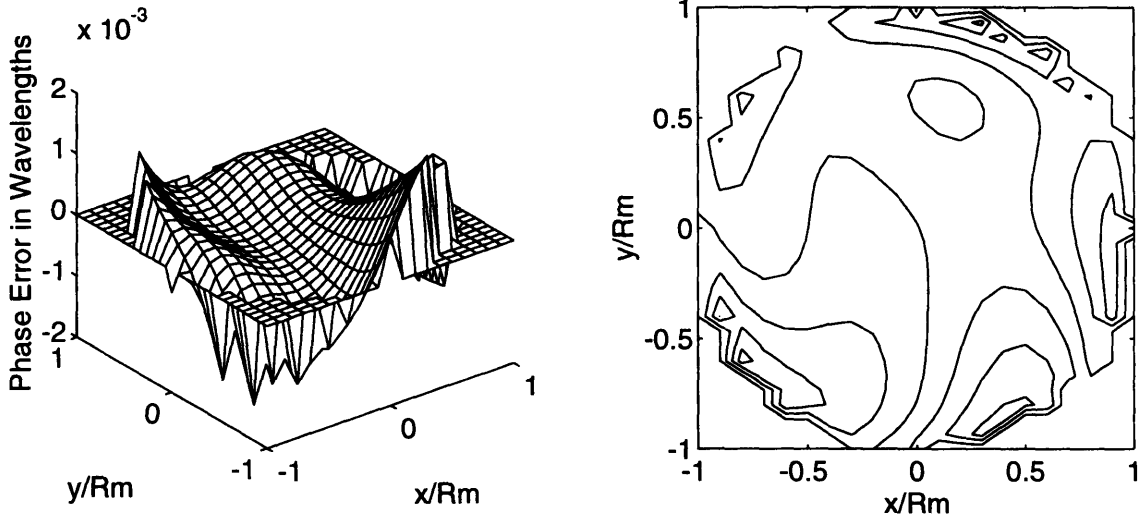


Figure 4.2. Wavefront Distortion Due to Turbulence, Stationary Target Light Wind.

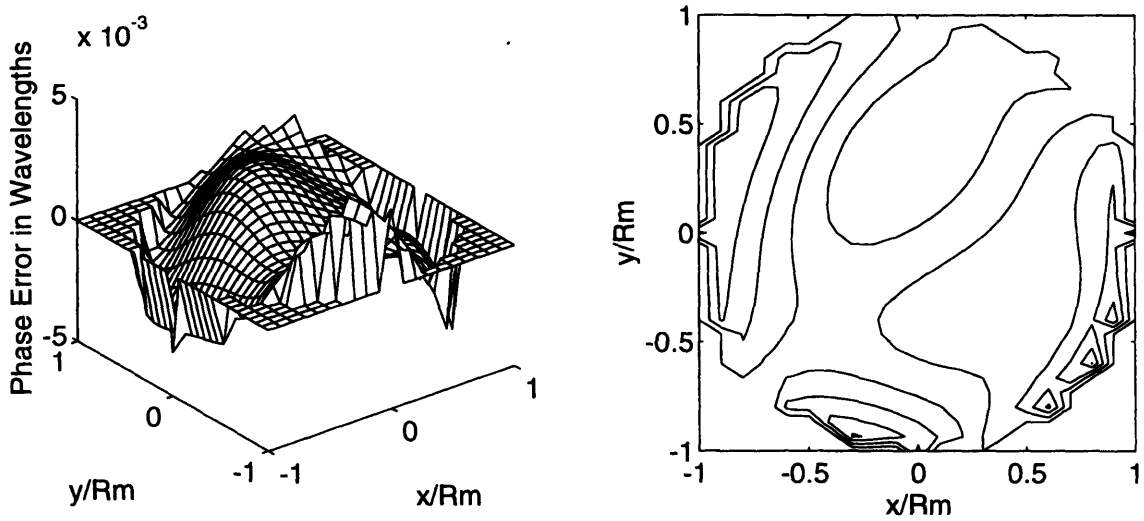


Figure 4.3. Wavefront Distortion Due to Turbulence, Moving Target Moderate Wind.

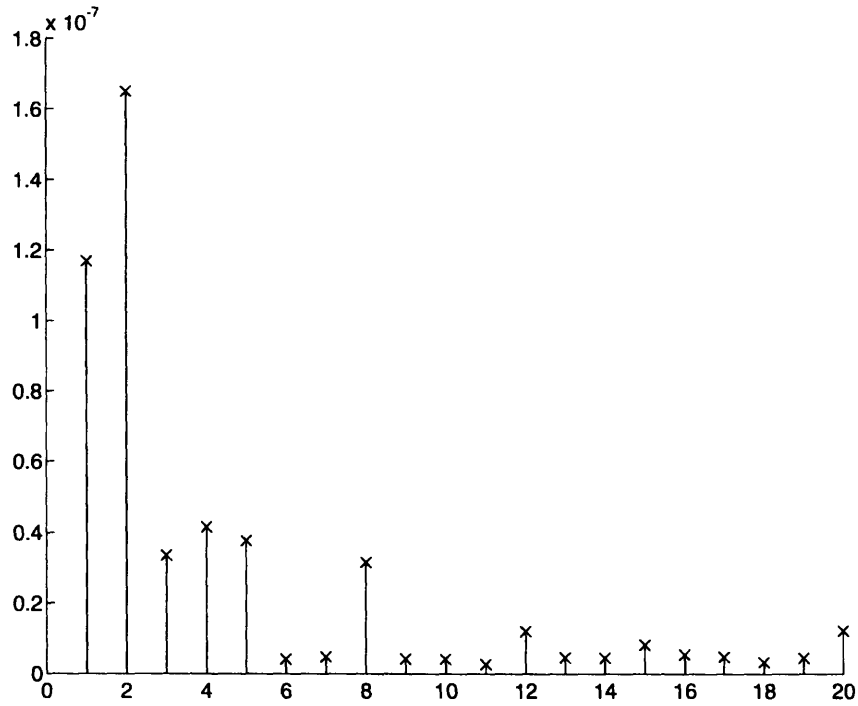


Figure 4.4. RMS Zernike Coefficient Values Corresponding to Figure 4.2.

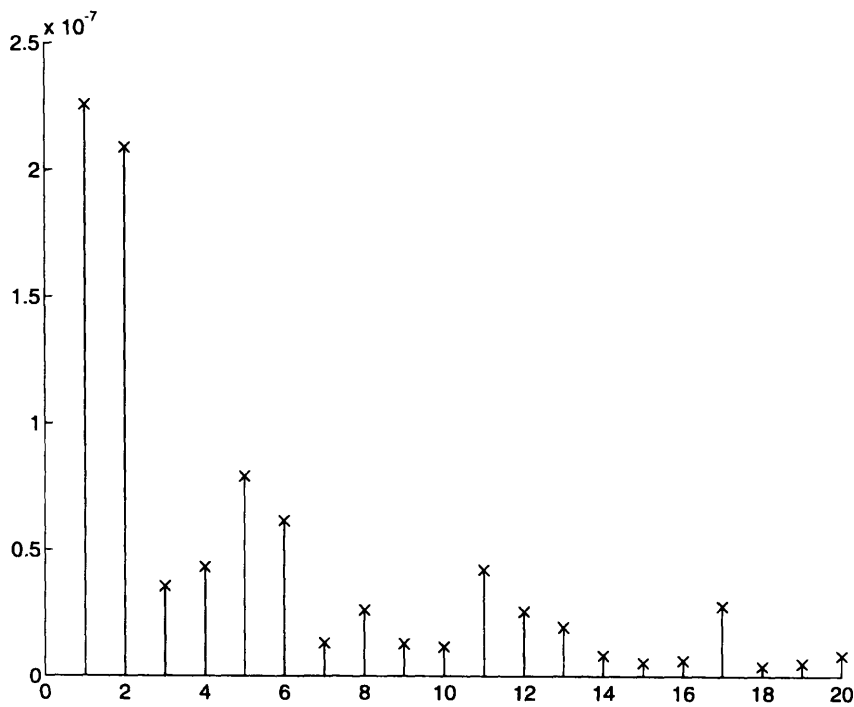


Figure 4.5. RMS Zernike Coefficient Values Corresponding to Figure 4.3.

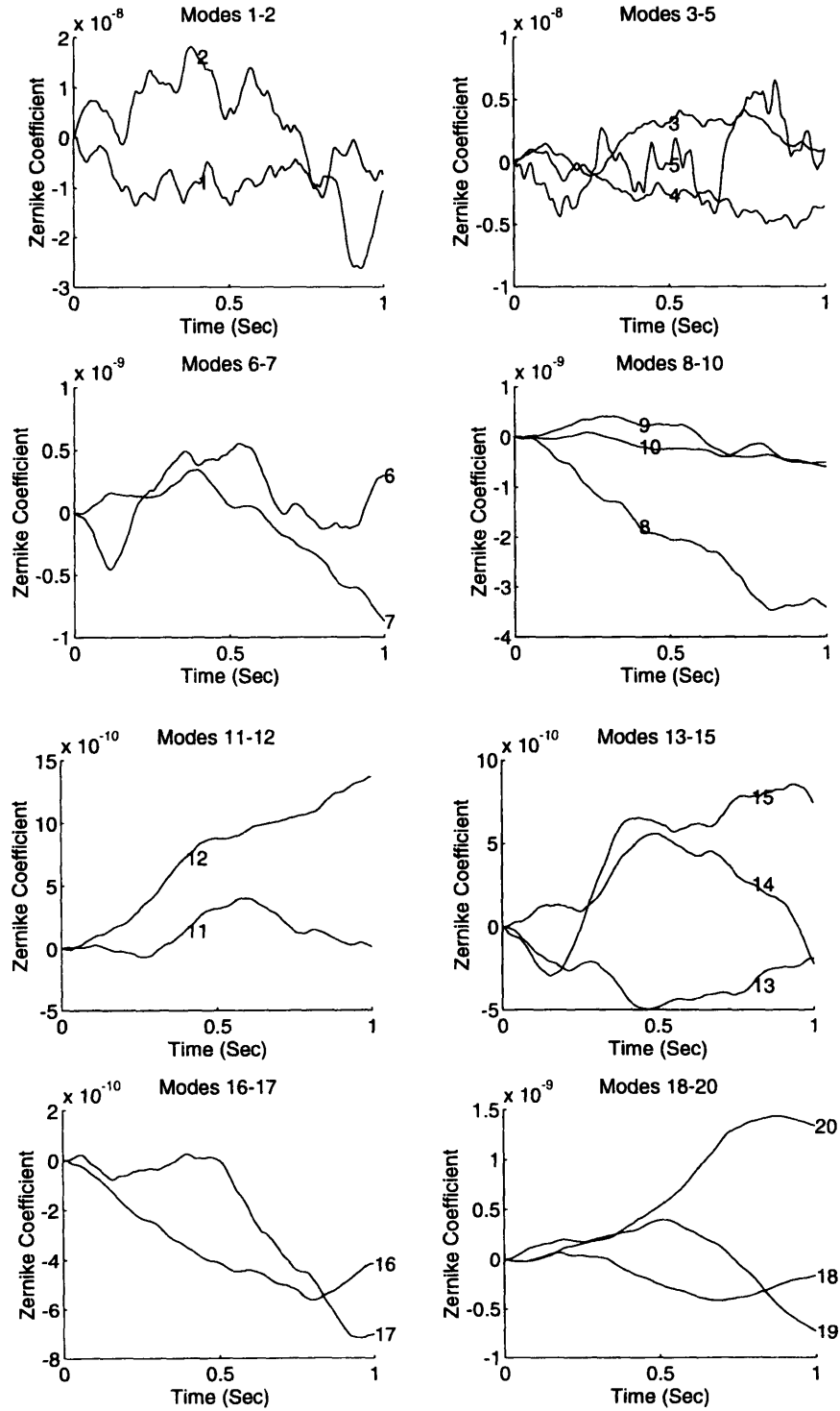


Figure 4.6. Zernike Coefficient Time History Corresponding to Figure 4.2.

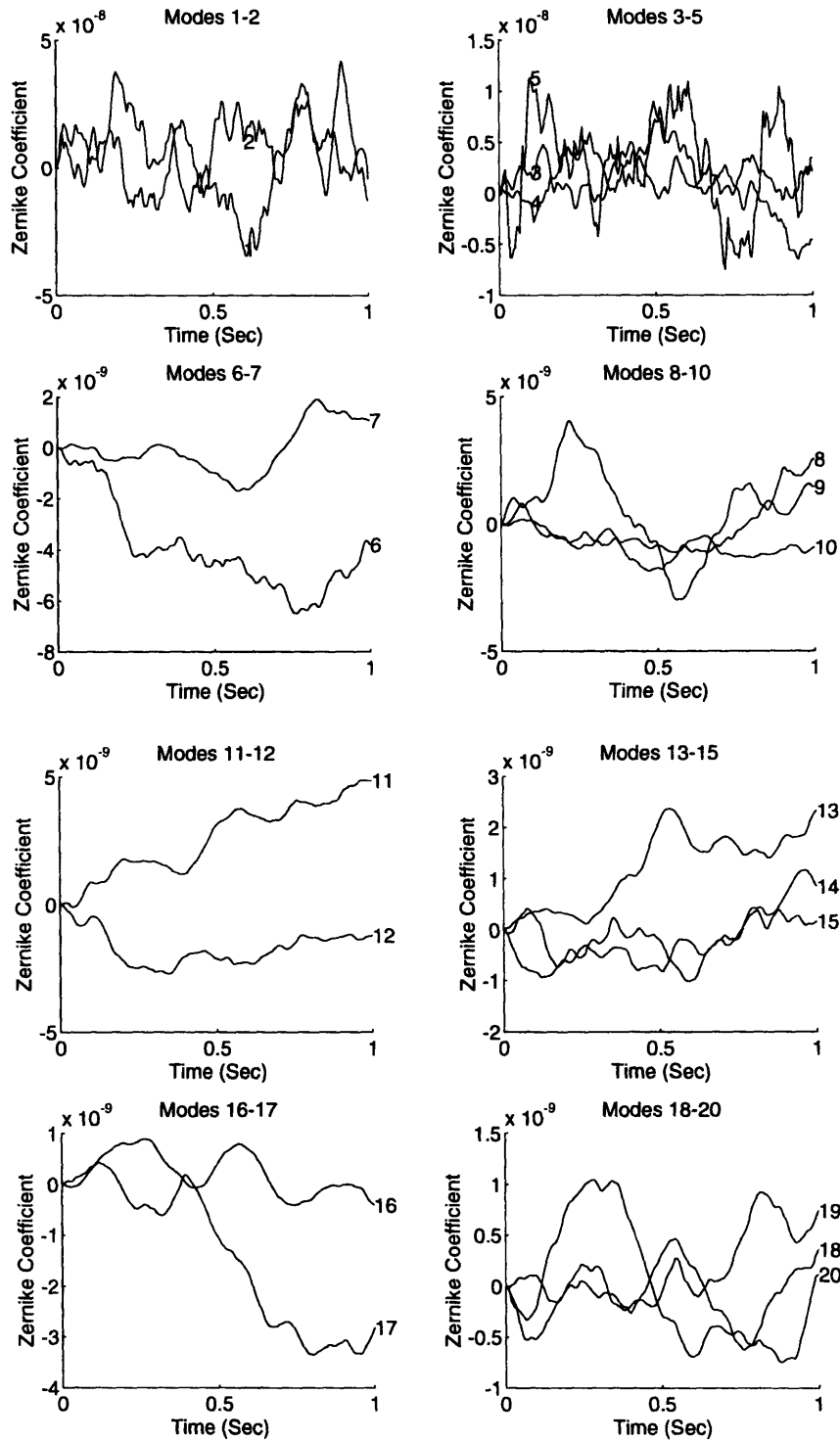


Figure 4.7. Zernike Coefficient Time History Corresponding to Figure 4.3.

4.4 COVARIANCE OF PRIMARY MODES

In Chapter 6, an extended Kalman filter will be designed to estimate the transverse wind velocity from return wavefront measurements. In this section the covariances of the focus, astigmatism, coma, and spherical modes will be derived for use in that design.

Recall that each turbulence Zernike coefficient is modeled as the output of a linear filter $S_i(j\omega) = K_i H_i(j\omega)$ driven by unity variance continuous-time white noise. Equation 4.10 gives $H_i(j\omega)$ and Equation 4.19 gives K_i . The transfer functions for the relevant modes are then converted into discrete-time state space representation. Using the state space A, B, C, D matrices it is possible to determine the noise covariances needed in the Kalman filter implementation. Letting x_{T_k} represent the turbulence state, w_{T_k} the noise input, and y_{T_k} the turbulence Zernike coefficient

$$x_{T_{k+1}} = Ax_{T_k} + Bw_{T_k} \quad (4.20)$$

$$y_{T_k} = Cx_{T_k} + Dw_{T_k} \quad (4.21)$$

The turbulence coefficients have zero mean, so the state covariance is

$$P_{x_{T_k}} = E[x_{T_k} x_{T_k}^T] \quad (4.22)$$

$$P_{x_{T_{k+1}}} = E[x_{T_{k+1}} x_{T_{k+1}}^T] = E[(Ax_{T_k} + Bw_{T_k})(Ax_{T_k} + Bw_{T_k})^T] = AP_{x_{T_k}}A^T + BB^T \quad (4.23)$$

In steady state,

$$P_{x_T} = P_{x_{T_{k+1}}} = P_{x_{T_k}} = AP_{x_{T_k}}A^T + BB^T \quad (4.24)$$

Equation 4.24 is a Lyapunov equation and can be solved using standard techniques [21].

The covariance of the output, P_{Y_T} , can be determined from P_{X_T}

$$P_{Y_T} = E[yy^T] = E[(Cx_{T_k} + Dw_{T_k})(Cx_{T_k} + Dw_{T_k})^T] = CP_{X_T}C^T + DD^T \quad (4.25)$$

Assuming the nominal parameter values, for the turbulence focus Zernike coefficient

$$A = \begin{bmatrix} -6.329 \times 10^{-3} & -2.271 \\ 2.070 \times 10^{-3} & 7.429 \times 10^{-1} \end{bmatrix} \quad B = \begin{bmatrix} 2.070 \times 10^{-3} \\ 2.343 \times 10^{-4} \end{bmatrix} \quad (4.26)$$

$$C = [0.000 \quad 1.385 \times 10^{-4}] \quad D = [0.000]$$

$$P_{Y_{T_f}} = 2.387 \times 10^{-15} \text{ m}^2 = 1.653 \times 10^{-4} \text{ wavelengths}^2 \quad (4.27)$$

For the turbulence astigmatism Zernike coefficient

$$A = \begin{bmatrix} -4.017 \times 10^{-3} & -1.655 \\ 1.994 \times 10^{-3} & 8.216 \times 10^{-1} \end{bmatrix} \quad B = \begin{bmatrix} 1.994 \times 10^{-3} \\ 2.150 \times 10^{-4} \end{bmatrix} \quad (4.28)$$

$$C = [0.000 \quad 1.822 \times 10^{-4}] \quad D = [0.000]$$

$$P_{Y_{T_a}} = 4.801 \times 10^{-15} \text{ m}^2 = 3.325 \times 10^{-4} \text{ wavelengths}^2 \quad (4.29)$$

For the turbulence coma Zernike coefficient

$$A = \begin{bmatrix} -1.127 \times 10^{-2} & -8.292 \times 10^{-1} & -1.108 \times 10^{-1} \\ 1.451 \times 10^{-2} & 9.278 \times 10^{-1} & -9.711 \times 10^{-3} \\ 1.272 \times 10^{-3} & 9.682 \times 10^{-2} & 1.000 \end{bmatrix} \quad B = \begin{bmatrix} 1.451 \times 10^{-2} \\ 1.272 \times 10^{-3} \\ 5.615 \times 10^{-5} \end{bmatrix} \quad (4.30)$$

$$C = [0.000 \quad 1.122 \times 10^{-5} \quad 1.603 \times 10^{-8}] \quad D = [0.000]$$

$$P_{Y_{T_c}} = 1.712 \times 10^{-15} \text{ m}^2 = 1.186 \times 10^{-4} \text{ wavelengths}^2 \quad (4.31)$$

For the turbulence spherical Zernike coefficient

$$A = \begin{bmatrix} -2.064 \times 10^{-3} & -5.865 \times 10^{-1} \\ 2.085 \times 10^{-2} & 9.526 \times 10^{-1} \end{bmatrix} \quad B = \begin{bmatrix} 2.085 \times 10^{-2} \\ 1.685 \times 10^{-3} \end{bmatrix} \quad (4.32)$$

$$C = [0.000 \quad 3.366 \times 10^{-6}] \quad D = [0.000]$$

$$P_{Y_{T_s}} = 4.364 \times 10^{-16} \text{ m}^2 = 3.022 \times 10^{-5} \text{ wavelengths}^2 \quad (4.33)$$

4.5 SUMMARY

A highly detailed model for atmospheric turbulence has been presented. The inputs are six atmospheric and target parameters. The outputs are twenty Zernike coefficients. The primary equations were derived by researchers at TASC. The covariances of the focus, astigmatism, coma, and spherical modes were computed for use in the extended Kalman filter design in Chapter 6.

Chapter 5

Optimal Atmospheric Correction

The purpose of a directed energy system is to deliver energy to a target. In this chapter the extent to which various control strategies meet that objective will be examined. The control strategies to be examined are: open loop, phase conjugation, optical focal length, and optimal focal length with optimal power. The optimal corrections maximize over intensity on target. The control techniques deal solely with the focus distortion; the other modes are not corrected. Correcting other modes would increase intensity on target, but focus is by far the most important aberration causing 73% of the thermal blooming beam spreading [11]. In each of the simulations, all measurements are assumed perfect and all atmospheric parameters are known.

The assumption that all parameters are perfectly known is unrealistic and exaggerates the benefits of using optimal focus and power control techniques, but it does provide an upper bound for the benefits of the alternative control strategies. Chapter 6 presents an estimator which attempts to determine transverse wind velocity from return wave measurements. The same scenarios that are presented here are presented again in Chapter 7, but instead of

having perfect knowledge of the parameters, the parameters are perturbed and estimated wind velocities are used.

Currently, no control systems contain an internal model of thermal blooming. Phase conjugation, open loop, and dithering techniques are the only methods currently being used to counter the effects of thermal blooming.

5.1 CONTROL STRATEGIES

5.1.1 OPEN LOOP

For the open loop simulation, the laser focus is set to the target distance. No other target knowledge or atmospheric information is considered in determining the focus command.

5.1.2 PHASE CONJUGATION

For the phase conjugation simulation, the laser focus is nominally set to the target distance, then adjusted to negate the atmospheric effects by applying the conjugate of the measured return wave. The return wave is assumed to be a glint off the target. It starts out as a plane wave and travels back to the laser becoming distorted by both blooming and turbulence effects. The return wave is decomposed in a Zernike polynomial expansion and the focus coefficient is mapped to a corresponding focal length using the relationship for the sag of a parabola

$$c = \frac{1}{2f} \tag{5.1}$$

Using the lens formula [22], the target distance and the negative of the atmospheric focus are combined to give the phase conjugate focus command

$$\frac{1}{f_{\text{command}}} = \frac{1}{f_{\text{target}}} - \frac{1}{f_{\text{atmosphere}}} \quad (5.2)$$

5.1.3 OPTIMAL FOCAL LENGTH

For the optimal focal length simulation, the model of thermal blooming presented in Chapter 3 and the model of atmospheric turbulence presented in Chapter 4 are used to determine the focal length required to maximize intensity on target. Figure 5.1 shows a typical shape of a focal length - intensity curve. This control strategy internally climbs to the top of the curve and generates the appropriate focal length to send to the deformable mirror. The MATLAB™ function "**fmins**", found in the Optimization toolbox, is used to find the optimal focal length. **Fmins** uses the Nelder and Mead Simplex search algorithm [23].

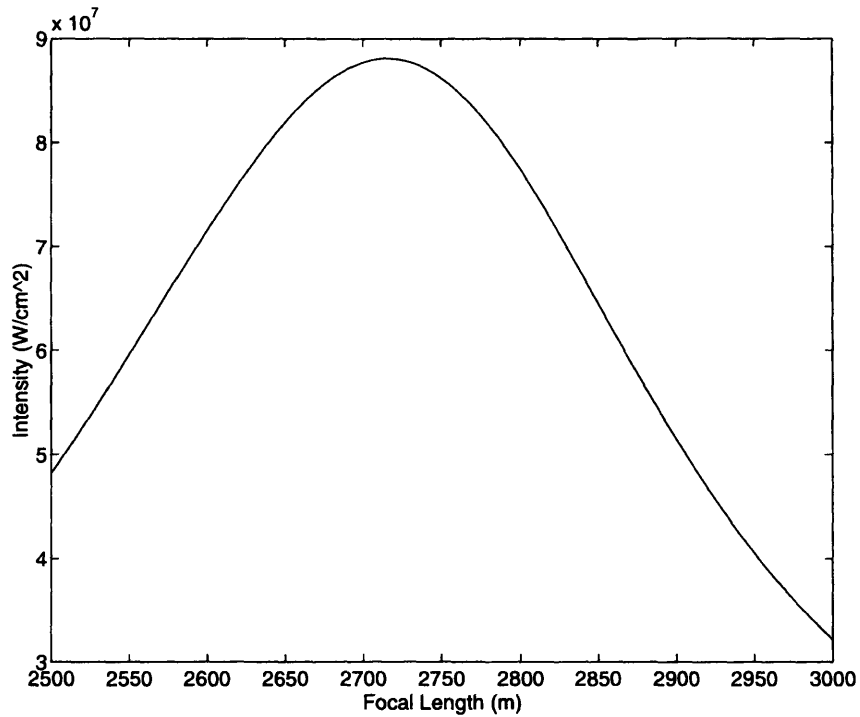


Figure 5.1. Intensity as a Function of Focal Length.

5.1.4 OPTIMAL FOCAL LENGTH WITH OPTIMAL POWER

The final strategy to be considered allows for power throttling. It is identical to the previous method with the additional capability of allowing for modification of the laser power. As a result, the maximization of intensity is now over two variables. It is assumed that the laser power can be decreased below the nominal value, but not increased. As a result, the optimal power technique only differs from optimal focus when the nominal power is greater than the critical power. Figure 5.2 shows a typical shape of a focal length - power - intensity surface.

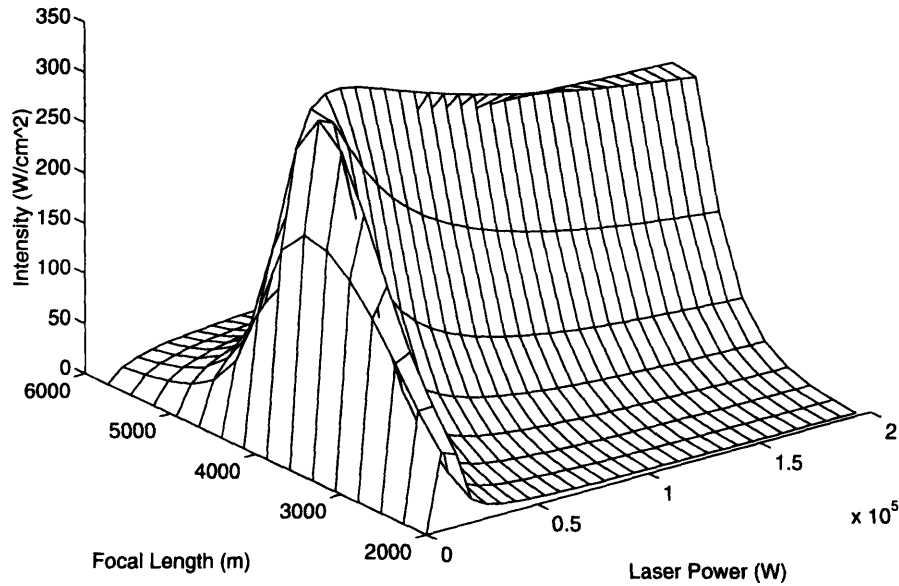


Figure 5.2. Intensity as a Function of Focal Length and Laser Power.

5.2 SIMULATIONS

In this section, three scenarios are used to compare the various control strategies. It is shown that for light thermal blooming, phase conjugation does a good job in maximizing intensity on target. However, for moderate thermal blooming, it is possible to significantly increase intensity on target by modifying the focal length and laser power. For heavy thermal blooming, phase conjugation overcompensates for thermal blooming leading to a reduction in target intensity from open loop. By properly accounting for the nonlinearities, the optimal model based strategies can improve performance even in the case of heavy thermal blooming.

5.2.1 LIGHT THERMAL BLOOMING

The target route for the first scenario is shown in Figure 5.3. The target X-velocity is 100 m/s (224 mph) and the wind speed is 15 m/s (34 mph). The target and wind are both moving to the right. The crosswind and beam slewing keep thermal blooming to a minimum.

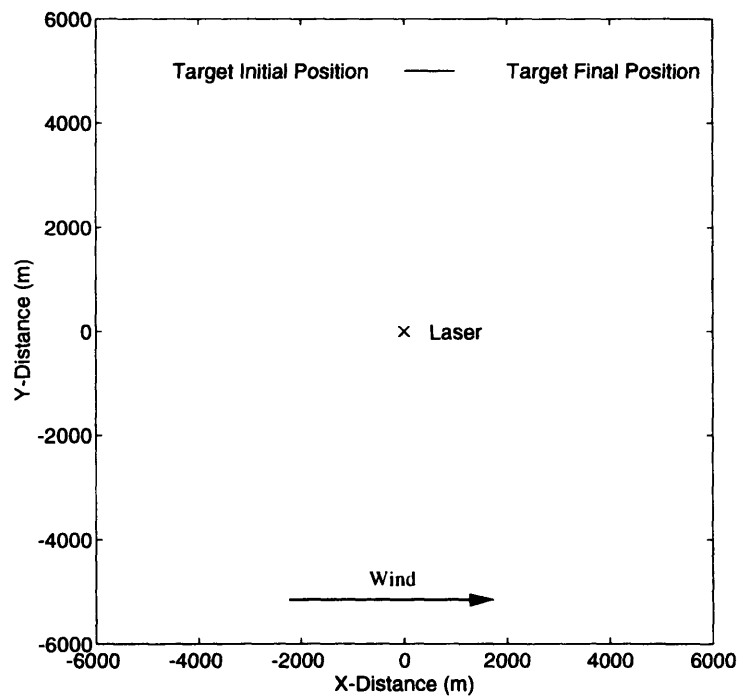


Figure 5.3. Target Route for Light Thermal Blooming Scenario.

The performance indicators are shown in Figure 5.4. Note that the laser power - intensity plot is calculated for the final time instant of the scenario. Because the system is operating at less than critical power, it is not possible to increase performance by reducing laser power. As a result, the optimal power technique and the optimal focus technique are identical for this scenario. By decreasing the focal range 200 meters less than the target range it is possible to increase intensity on target 8% over open loop. Phase conjugation

under compensates for thermal blooming and decreases the focal range only 50 meters, resulting in a 2.5% increase in intensity on target over open loop.

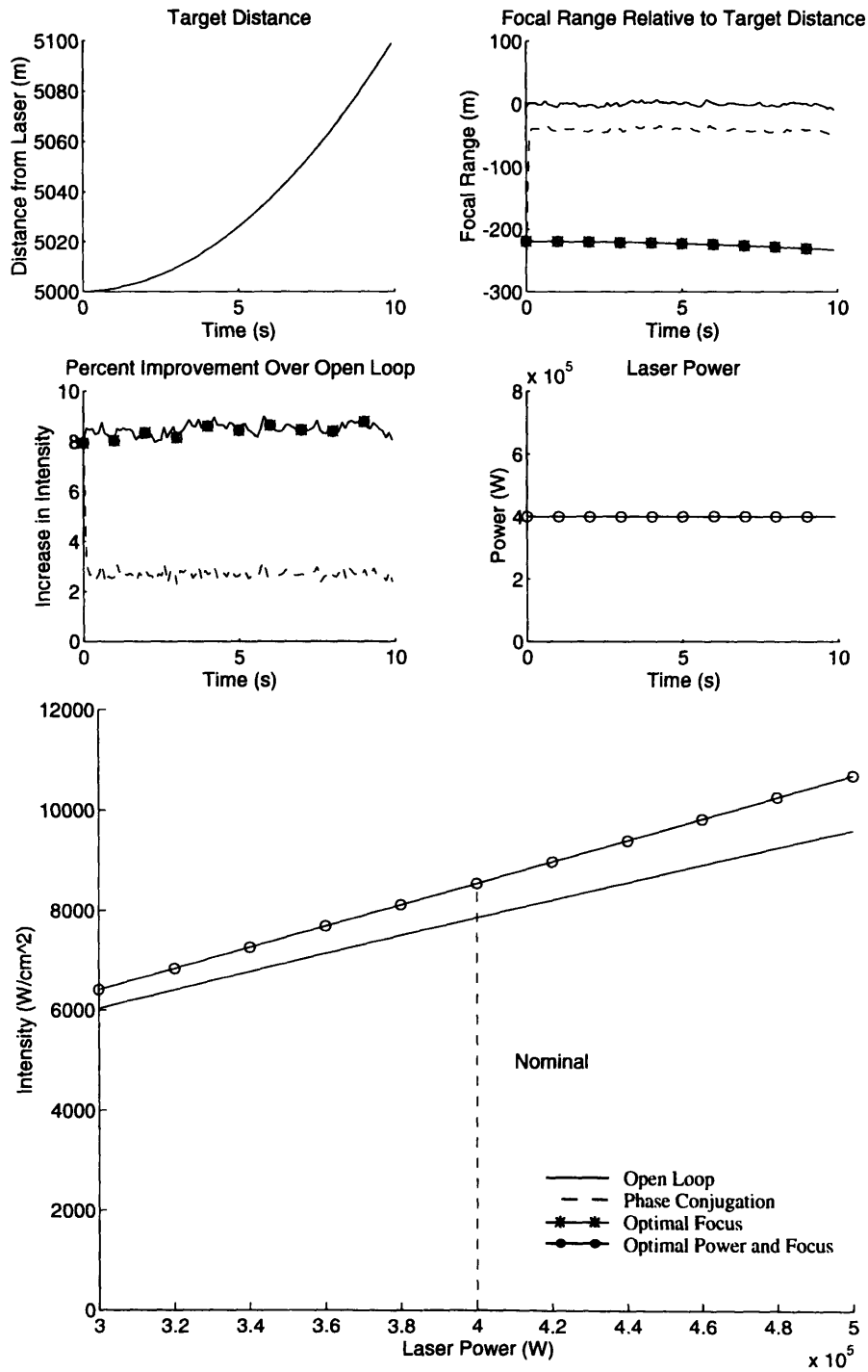


Figure 5.4. Performance Comparison for Light Thermal Blooming.

Figure 5.5. shows the focal range - intensity curve for the final time instant of the scenario. The open loop, phase conjugate, and optimal focus focal ranges and the corresponding peak intensity levels are indicated. Because intensity does not change much with focal range, the three control strategies result in similar performance. If there is a strong wind and beam slewing, there is no significant advantage to using a complicated technique to choose the focal range.

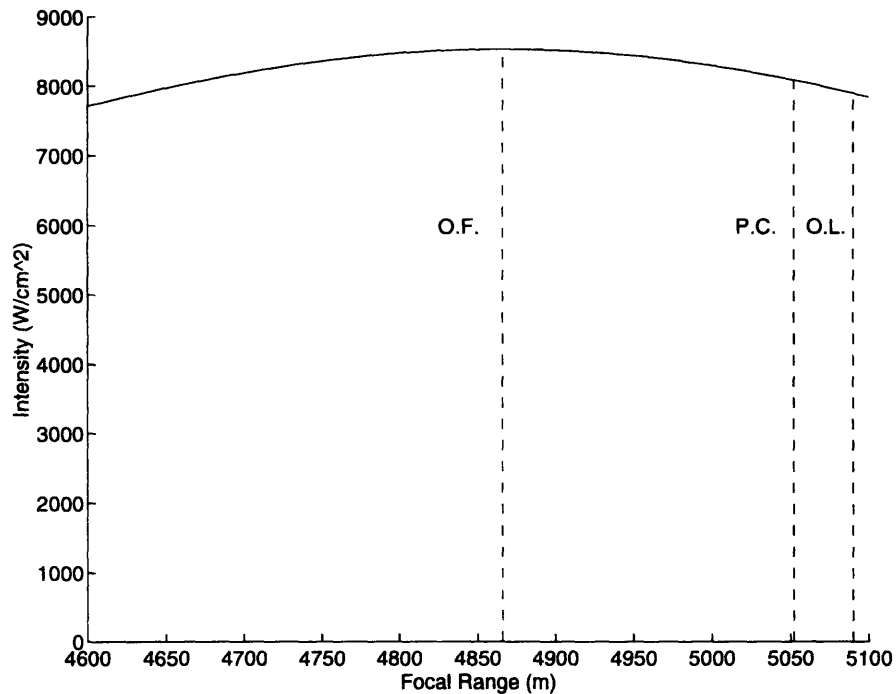


Figure 5.5. Intensity as a Function of Focal Range for Light Thermal Blooming Indicating Open Loop, Phase Conjugate, and Optimal Focus Focal Ranges.

5.2.2 MODERATE THERMAL BLOOMING

The target route for the second scenario is shown in Figure 5.6. The target X-velocity and Y-velocity are 71 m/s (159 mph) and the wind speed is 5 m/s (11 mph). The target and wind are both moving to the right. The slower wind speed in combination with the new target location result in much less clearing of heated air along the beam. This results in

greater thermal blooming and increases the benefits of using optimal focal length correction.

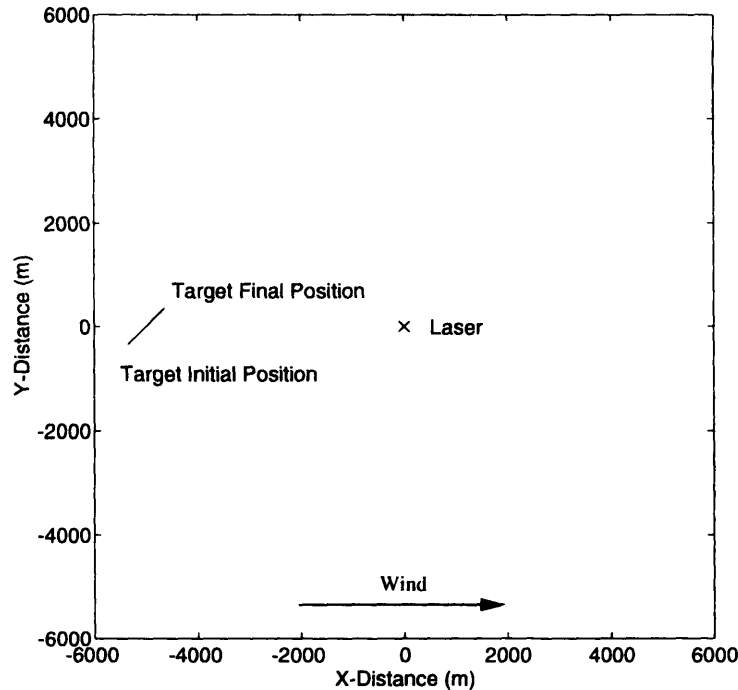


Figure 5.6. Target Route for Moderate Thermal Blooming Scenario.

The performance indicators are shown in Figure 5.7. The spike in the middle of the simulation occurs when the target crosses the X-axis and the wind is orthogonal to the beam. This is the only point where the nominal power is greater than critical power - nominal power is 400,000 Watts and critical power is 250,000 Watts. By decreasing the focal range 400-700 meters less than the target range it is possible to increase intensity on target 25-45% over open loop. Phase conjugation under compensates for thermal blooming and decreases the focal range only 100 meters, resulting in a 10% increase in intensity on target over open loop.

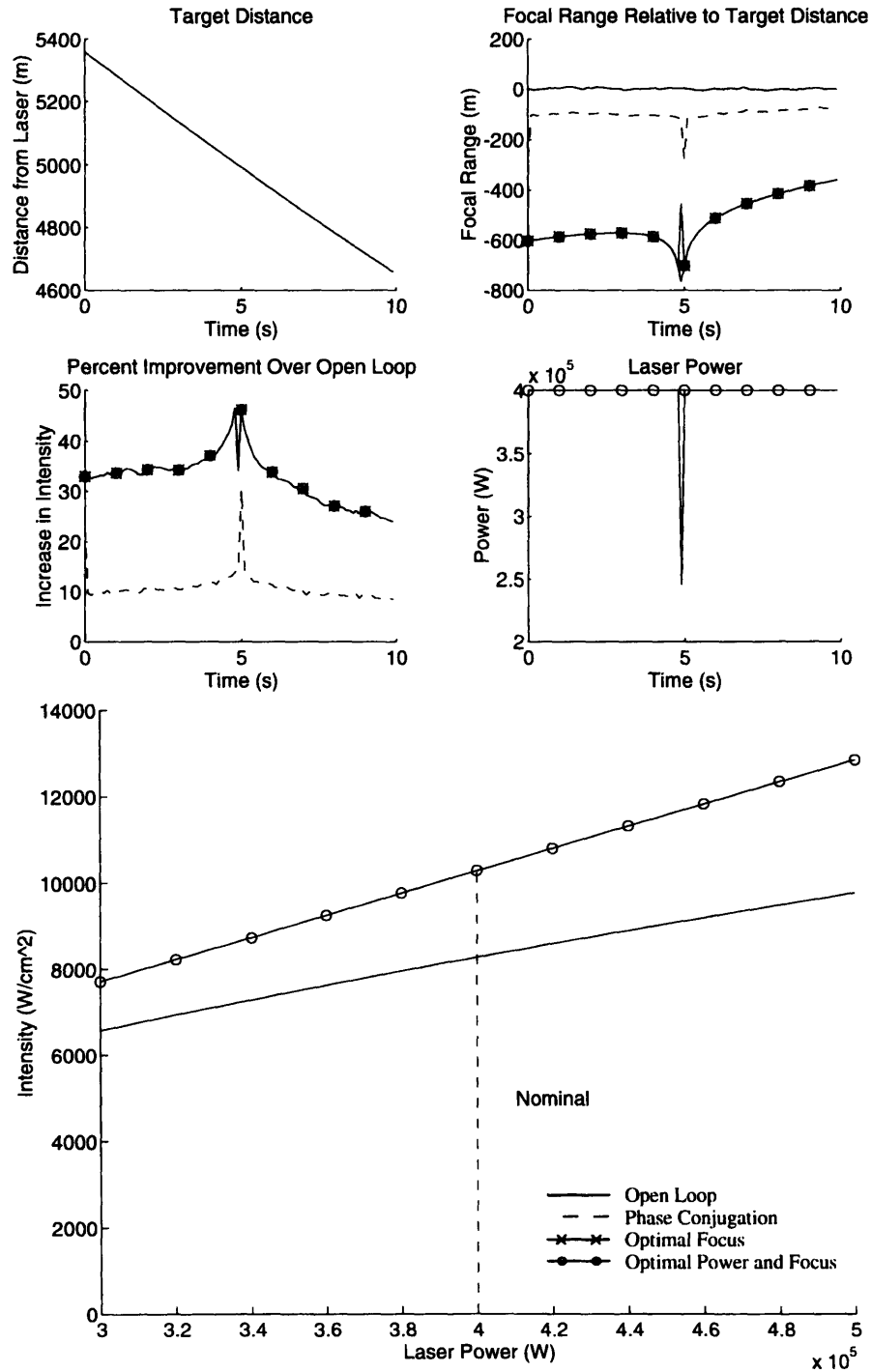


Figure 5.7. Performance Comparison for Moderate Thermal Blooming.

Figure 5.8. shows the focal range - intensity curve for the final time instant of the scenario. The open loop, phase conjugate, and optimal focus focal ranges and the corresponding peak intensity levels are indicated. Because intensity is much more dependent upon focal range, the performance of the different control strategies becomes more evident. For moderate thermal blooming, it begins to make sense to explore alternative control strategies.

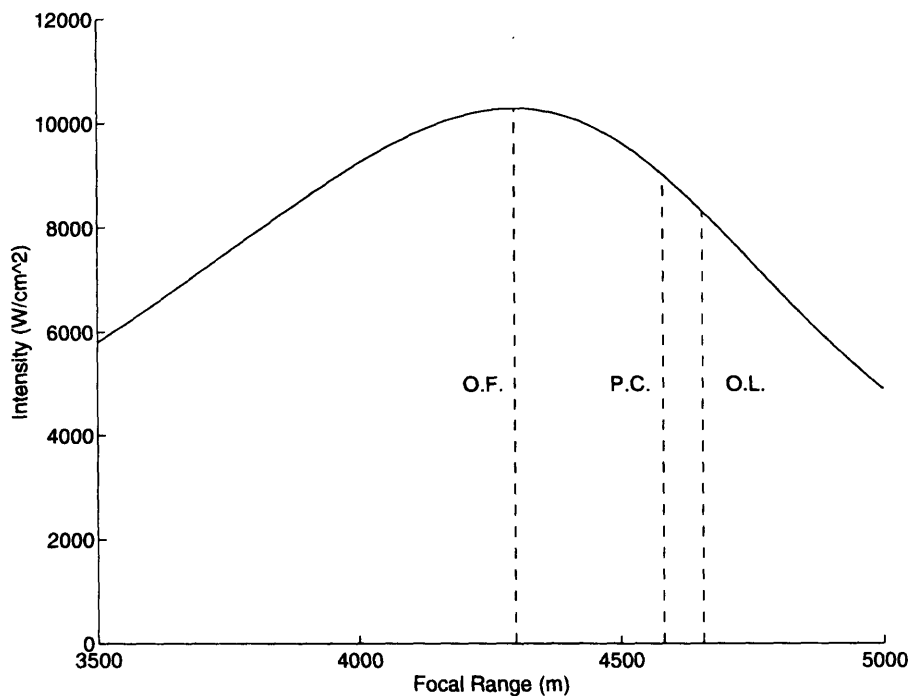


Figure 5.8. Intensity as a Function of Focal Range for Moderate Thermal Blooming Indicating Open Loop, Phase Conjugate, and Optimal Focus Focal Ranges.

5.2.3 HEAVY THERMAL BLOOMING

The target route for the third scenario is shown in Figure 5.9. The target Y-velocity is 100 m/s (224 mph). There is no wind. The target is moving towards the laser. As would be expected, with neither wind nor slewing thermal blooming is severe. Only by decreasing the laser power can the performance be improved.

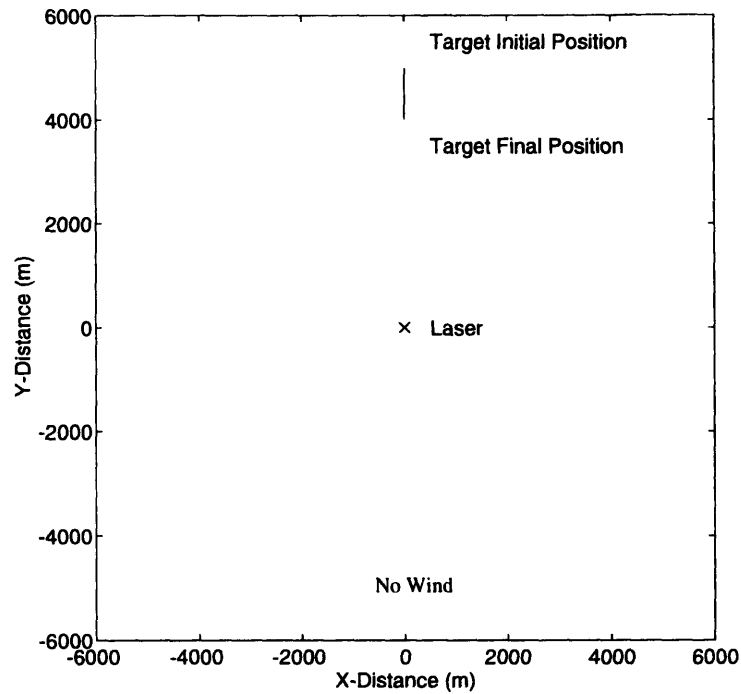


Figure 5.9. Target Route for Heavy Thermal Blooming Scenario.

The performance indicators are shown in Figure 5.10. For the entire simulation, critical power is less than nominal power. Correspondingly, the optimal power and optimal focus strategies result in different performance. For heavy thermal blooming, phase conjugation significantly overcompensates for blooming and actually performs worse than open loop. Because blooming is so severe, even optimal focus correction is not able to improve on open loop performance. Greater intensity on target can only be achieved by decreasing the laser power to a fraction of its nominal value.

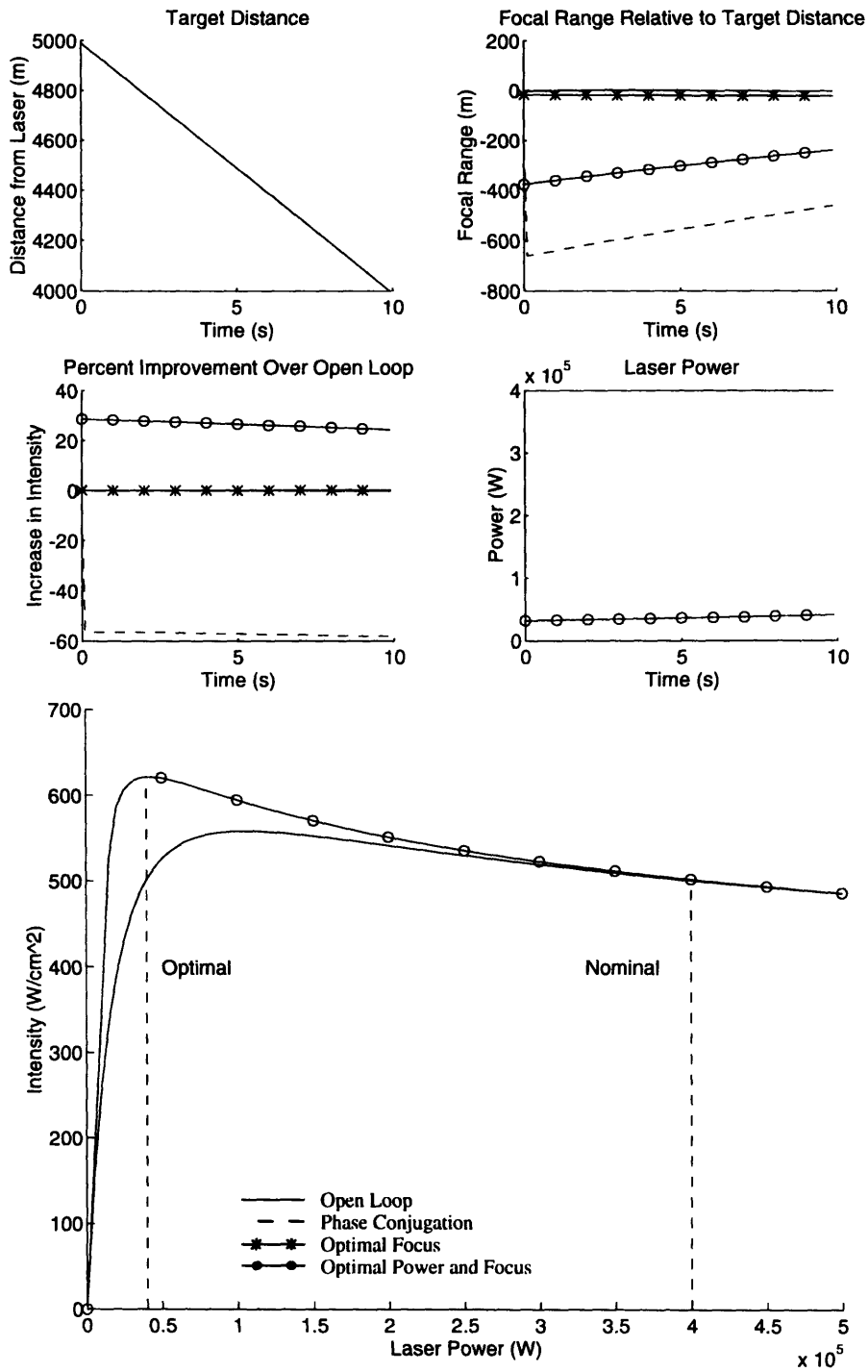


Figure 5.10. Performance Comparison for Heavy Thermal Blooming.

Figure 5.11 shows the focal range - intensity curve for the final time instant of the scenario. The open loop, phase conjugate, and optimal focus focal ranges and the corresponding peak intensity levels are indicated. The optimal focal range is virtually the same as the target range - open loop control. It is not possible to do any better than open loop, but it is possible to do worse. Phase conjugation decreases the focal range 450 meters less than open loop and results in a 50% drop in intensity on target.

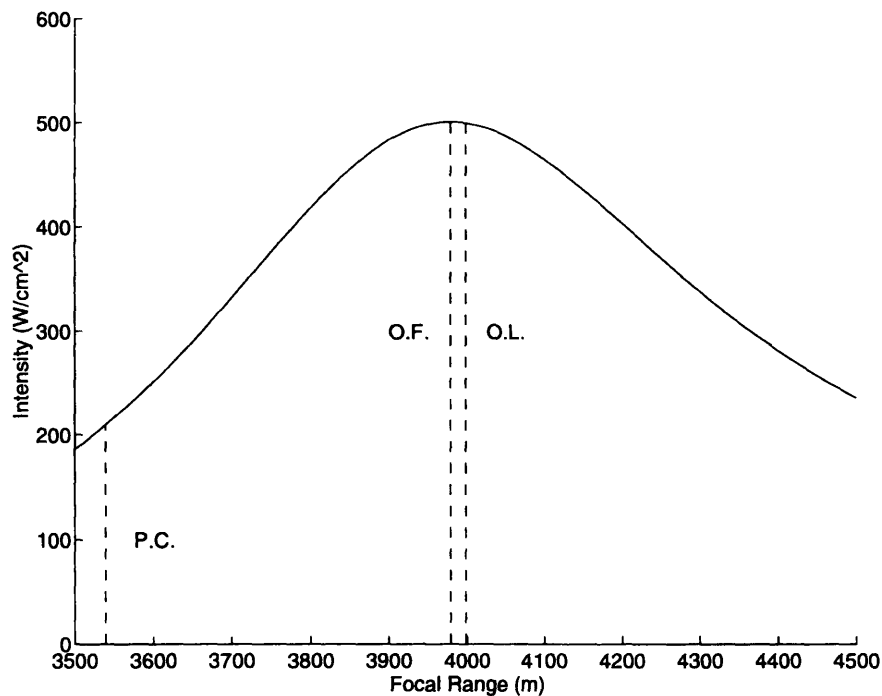


Figure 5.11. Intensity as a Function of Focal Range for Heavy Thermal Blooming Indicating Open Loop, Phase Conjugate, and Optimal Focus Focal Ranges.

5.3 SUMMARY

A novel, model-based control technique has been presented and shown to have the capability to significantly improve the performance of directed energy systems in the atmosphere.

Phase conjugation has been seen to be a reasonable control method when dealing with light thermal blooming. However when the level of blooming increased, phase conjugation steadily worsened. For heavy thermal blooming, phase conjugation resulted in only half the intensity on target that simple open loop control delivers.

When optimal focus was used, the performance was guaranteed to be better than open loop, assuming an accurate model. For moderate blooming, optimal focus increased intensity on target 25-45% over open loop. As blooming increased, such that critical power became less than nominal power, the difference between optimal focus with nominal laser power and open loop became negligible.

For heavy blooming, reducing the laser power was the only way to improve the system performance. A dramatic reduction in laser power resulted in a 20-30% improvement over open loop.

The optimal correction results presented in this chapter assume an accurate model and complete knowledge of the state of the laser, atmosphere, and target. In Chapter 6, the sensitivity of the optimal correction to model parameter errors is analyzed and an estimator is designed for determining transverse wind speed from return wave measurements. Chapter 7 presents the complete model-based controller which uses the estimator to determine wind speed. Using the same scenarios presented in this chapter, the performance of the controller is compared to phase conjugation and open loop control methods assuming model parameter errors.

Chapter 6

Parameter Sensitivity and Estimation

This chapter analyzes the sensitivity of optimal, model-based focus correction to errors in the model parameters. Optimal focus correction is shown to have superior performance to open loop control for a wide range of parameter uncertainty. The most critical parameter for all control techniques is target distance. Errors in target distance will cause the performance of all control methods to degrade. It is assumed that a measurement of target range and velocity is available from a tracker. Wind speed is the one parameter other than target information that will significantly change between and during scenarios. A variety of techniques to measure wind speed exist. However, it will be assumed that accurate measurements are not available. To arrive at an estimate for wind speed, an extended Kalman filter is designed to estimate transverse wind velocity from the return wave measurements.

6.1 PARAMETER SENSITIVITY

The sensitivity of the wavefront control to parameters that are likely to change during or between engagements are presented in detail in Appendix B. The optimal focus correction and open loop focus correction is calculated using the nominal parameter values. Using these nominal control values, peak intensity is calculated, along with the focus and astigmatism Zernike coefficients for the return wave, as a function of each parameter as the parameter varies between 50% and 150% of its nominal value. This is a way of determining the effects of incorrect parameter values on the different control methods. To see the degradation in performance due to incorrect parameter values, the optimal focal range correction is also computed at each point having perfect parameter knowledge and the corresponding peak intensity is calculated.

Except for variations in target distance, optimal focus correction results in better performance than open loop correction for the entire range of parameter variation for every parameter. Errors in target distance are particularly significant because the command being generated is focal range. A 10% error in target range will cause a corresponding error in focal range. As shown in Figures 5.5, 5.8, and 5.11 the difference between optimal focal correction and phase conjugate or open loop correction is only 300 or 400 meters, about 10% of the target distance. A typical sensitivity plot is shown in Figure 6.1. It shows the general trend for modeling errors in the refractive index. The range of 50% error is excessive, under no circumstances would the actual refractive index be nearly that far off from its nominal value.

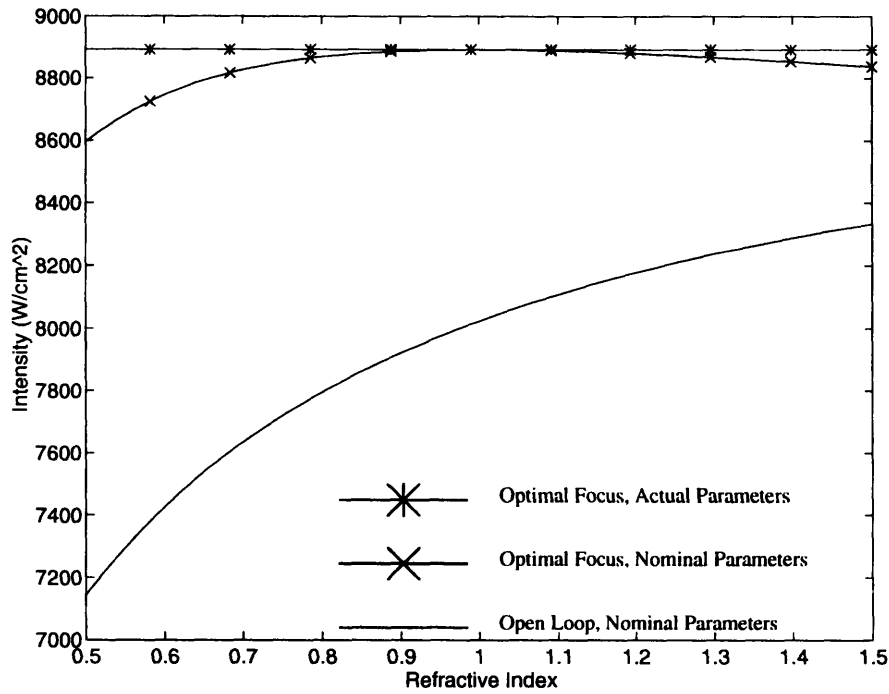


Figure 6.1. Sensitivity to Refractive Index.

The atmospheric variables used in the model have been studied extensively [24,25,26]. Complex models for these parameters exist and could be incorporated into the existing model of thermal blooming. For a given location and season, variations in these variables are quite small. Due to the small changes in performance caused by significant variations in parameter value, no attempt is made to estimate them. These errors could be reduced by taking physical measurements of the atmosphere on the day the system is used, or simply by entering in data from a reference table.

The variables that cannot simply be found in a table are the wind velocity and the target position and velocity. A radar tracking system is assumed to provide position and velocity measurements of the target. Therefore, wind speed is the only variable that must be measured or estimated. The sensitivity plot for wind speed is shown in Figure 6.2. Natural variations in wind speed along with changing target routes significantly effect the

transverse wind velocity. While a direct measurement of the wind speed is preferable, the next section presents an extended Kalman filter to estimate the transverse wind velocity from return wave measurements. Estimating wind speed in this fashion is inefficient, but demonstrates the ability to extract atmospheric data from return wavefront measurements.

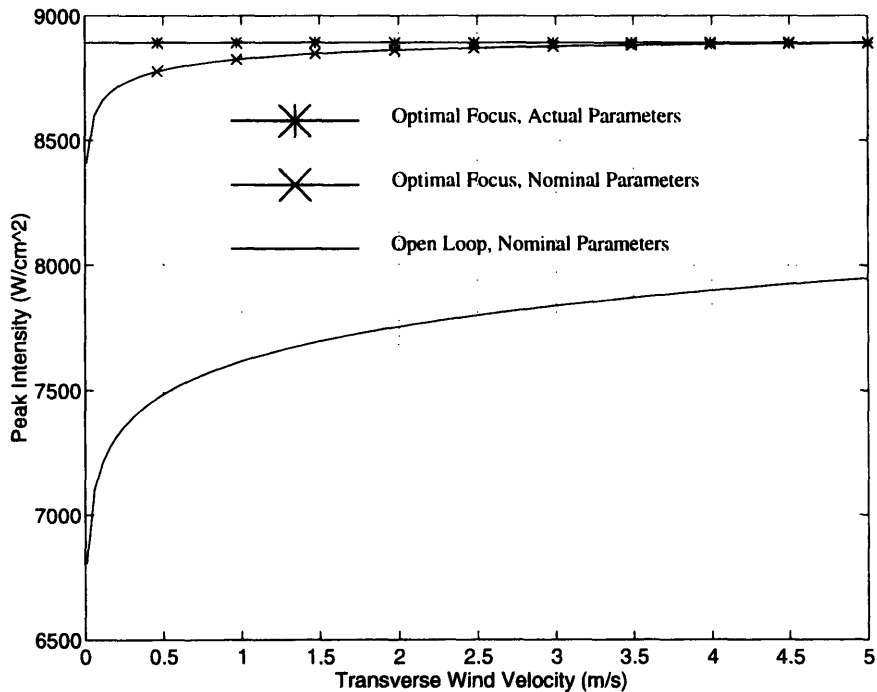


Figure 6.2. Sensitivity to Transverse Wind Velocity.

6.2 EXTENDED KALMAN FILTER DESIGN

6.2.1 BASIC EQUATIONS

This section presents the general equations for an extended Kalman filter with discrete measurements [27]. The next section puts the wind estimation problem into the same format.

The system model is

$$x_{k+1} = f(x_k) + w_k \quad (6.1)$$

$$w_k \sim N(0, Q_k) \quad (6.2)$$

where Equation 6.2 indicates that w is a Gaussian random variable with mean 0 and covariance Q_k .

The measurement model is

$$z_k = h_k(x(t_k)) + v_k \quad (6.3)$$

$$v_k \sim N(0, R_k) \quad (6.4)$$

The initial condition is

$$x(0) \sim N(\hat{x}_0, P_0) \quad (6.5)$$

The other assumptions are

$$E[w_i w_j^T] = 0, \forall i, j \quad (6.6)$$

$$E[v_i v_j^T] = 0, \forall i, j \quad (6.7)$$

$$E[v_k w_k^T] = 0, \forall k \quad (6.8)$$

where $E[\cdot]$ is the expected value operator.

Propagation of the state estimate is given by

$$\hat{x}_{k+1}(-) = f(\hat{x}_k(+)) \quad (6.9)$$

where $\hat{x}_k(-)$ denotes an estimate of the state before the measurement and $\hat{x}_k(+)$ denotes an estimate of the state after the measurement.

Propagation of the error covariance is given by

$$P_{k+1}(-) = F(\hat{x}_k(+))P_k(+)+F^T(\hat{x}_k(+))Q_k \quad (6.10)$$

where

$$F(x) = \frac{\partial f(x)}{\partial x} \quad (6.11)$$

The gain matrix is given by

$$K_k = P_k(-)H_k^T(\hat{x}_k(-))\left[H_k(\hat{x}_k(-))P_k(-)H_k^T(\hat{x}_k(-))+R_k\right]^{-1} \quad (6.12)$$

where

$$H_k(x) = \frac{\partial h_k(x)}{\partial x} \quad (6.13)$$

The state estimate update is

$$\hat{x}_k(+) = \hat{x}_k(-) + K_k[z_k - h_k(\hat{x}_k(-))] \quad (6.14)$$

The error covariance update is

$$P_k(+) = [I - K_k H_k(\hat{x}_k(-))]P_k(-) \quad (6.15)$$

6.2.2 IMPLEMENTATION

In this section, the equations for estimating wind speed from return wavefront measurements are put into the above framework. The transverse wind speed is to be estimated, so x_k represents the wind speed at time k . The wind is modeled as a random walk process, so $f(x_k) = x_k$. Q_k is the covariance of the driving noise. In order to keep the wind variation relatively small over the 0.1 second time step, Q_k is chosen to be $0.01 \text{ m}^2/\text{s}^2$.

Thus, the system model is given by

$$x_{k+1} = x_k + w_k \quad (6.16)$$

$$w_k \sim N(0, 0.01) \quad (6.17)$$

The return wavefront is decomposed into Zernike coefficients. The observation, z_k , is the coefficients corresponding to focus, astigmatism, coma, and spherical modes. The actual observation noise contains various components including sensor noise and turbulence effects. Since turbulence is not being estimated and is likely larger than the noise in a wavefront sensor, the existing model for atmospheric turbulence is used for v_k . Figures 4.6 and 4.7 show typical time histories for turbulence Zernike coefficients. Focus, astigmatism, coma, and spherical modes correspond to the numbers 3, 4, 6, and 10 respectively. Since each Zernike mode is modeled by separate shaping filters, and the time correlation of each turbulence mode is small over the 0.1 second sampling interval, the turbulence based sensor noise is modeled as a white Gaussian sequence.

The map from parameter values to return wave Zernike coefficients, with parameters other than wind speed held to their nominal values is given by $h_k(\cdot)$. Recall from Chapter 3 that

wind speed effects the Zernike coefficients through the heating phase, Ψ_h . Once again, the focus Zernike coefficient is given by

$$C_3 = \alpha_3(\sigma_{R1} + \sigma_{R2} + \sigma_{R3} + \sigma_{R4}) \quad (6.18)$$

where

$$\sigma_{Ri} = \sigma_{Fi} + \sigma_{Bi} \quad (6.19)$$

$$\sigma_{Bi} = K_B \sigma_B \quad (6.20)$$

$$\sigma_B^2 = C_B' (\sigma_L^2 - \sigma_w^2) \Psi_h^a \quad (6.21)$$

The heating phase is given by

$$\Psi_h = \left[\frac{N_D N_F N_R}{N_Q \gamma} \right] \left\{ \ln_0 - (1 - e^{-\epsilon z}) \ln_{\frac{N_R}{2}} - e^{-\epsilon z} \ln_{N_R} \right\} \quad (6.22)$$

and

$$\ln_z = \ln \left| \frac{\left[-N_S - N_R + \left(\frac{2N_Q}{N_F} \right)^2 N_R \right] z + N_S + N_R + \gamma \sqrt{(1-z)^2 + \left(\frac{2zN_Q}{N_F} \right)^2}}{(zN_S + N_R)} \right| \quad (6.23)$$

Wind speed, U_w , enters into the distortion number

$$N_D = -2 \left(\frac{\partial n}{\partial T} \right) \frac{P Z_f^2 \alpha}{R_m^3 U_w C_p \rho n_\infty} \quad (6.24)$$

and the slew number

$$N_S = \frac{U_T}{U_w} \quad (6.25)$$

Thus the measurement model is

$$z_k = h_k(x(t_k)) + v_k \quad (6.26)$$

$$v_k \sim N(0, R_k) \quad (6.27)$$

where R_k is the diagonal matrix of turbulence covariances given in Chapter 4

$$R_k = \begin{bmatrix} P_{Y_{T_1}} & 0 & 0 & 0 \\ 0 & P_{Y_{T_2}} & 0 & 0 \\ 0 & 0 & P_{Y_{T_3}} & 0 \\ 0 & 0 & 0 & P_{Y_{T_4}} \end{bmatrix} \quad (6.28)$$

To run a simulation of the extended Kalman filter, it is necessary to choose an initial guess for the wind speed, $\hat{x}_0(-)$ and the variance of the initial guess, P_0 .

6.3 SIMULATIONS

Several typical simulations of the extended Kalman filter demonstrate that wind speed can be estimated with less than 1 m/s (2.24 mph) rms error. Plots of actual wind speed and estimated wind speed are shown below. The Kalman filter requires that values of all of the parameters other than wind speed be known. If these parameters are not known exactly, the Kalman filter's ability to accurately estimate the wind speed will be diminished. In Figure 6.2, the parameters other than wind speed are known exactly. In Figure 6.3, an error is introduced into the atmospheric and target model parameters by randomly choosing the value for each model parameter between 97.5% and 102.5% of its real value. A uniform probability distribution is used. Figures 6.4 and 6.5 introduce errors similarly by choosing the maximum parameter guess errors as 5% and 10% respectively. The initial estimate of the wind speed could be reasonably far from the actual wind speed, so P_0 is

chosen to be $4 \text{ m}^2/\text{s}^2$. In the following simulations, the initial wind speed is 5 m/s (11.2 mph), the initial wind estimate is 10 m/s (22.4 mph).

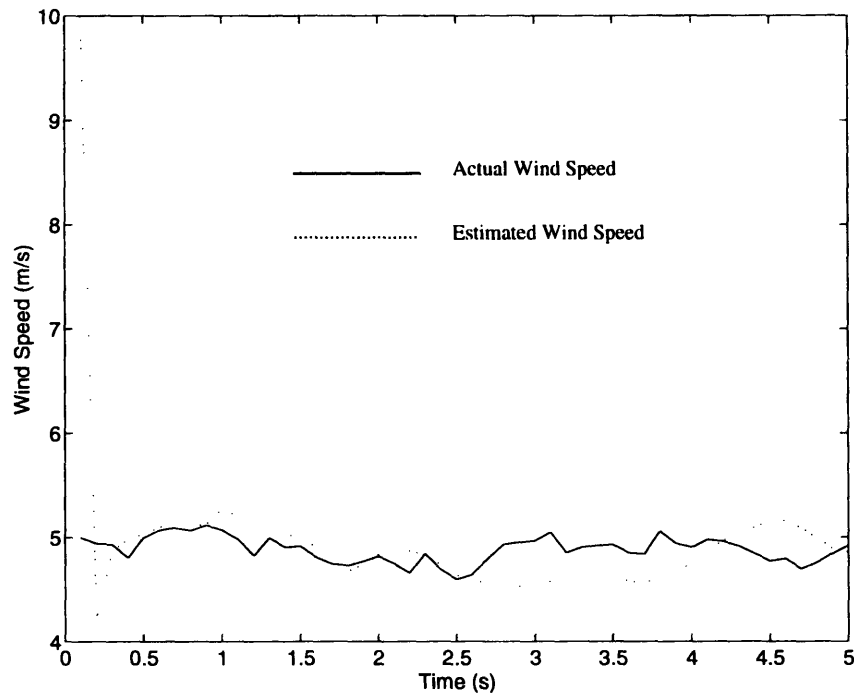


Figure 6.3. Kalman Filter Performance with Parameters Known Exactly.

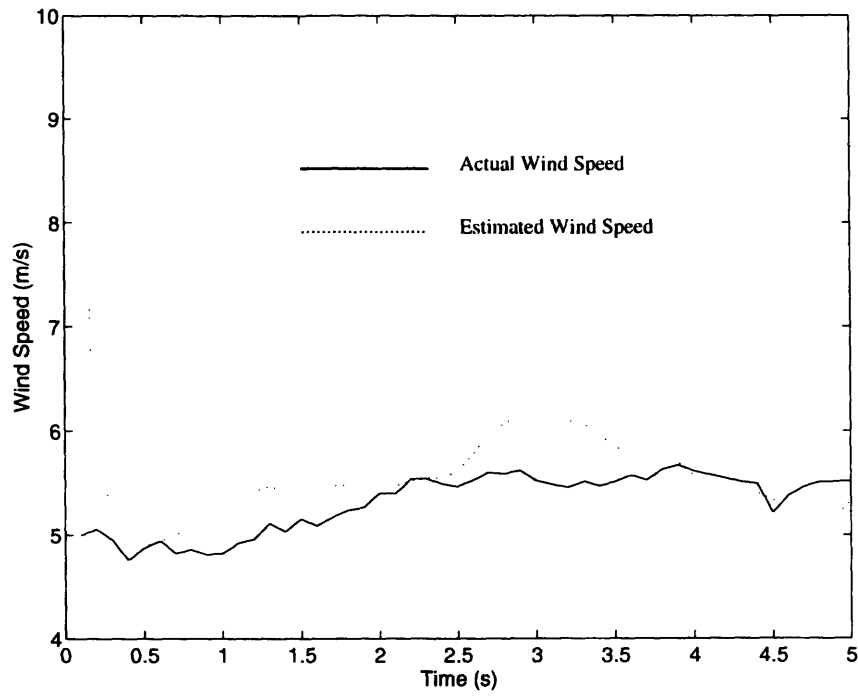


Figure 6.4. Kalman Filter Performance with Maximum Parameter Error of 2.5%.

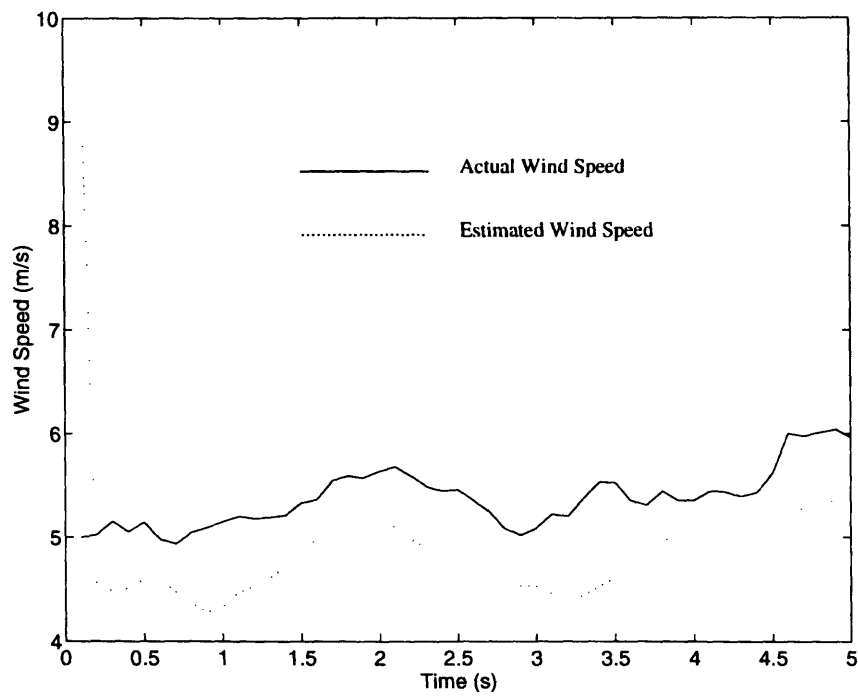


Figure 6.5. Kalman Filter Performance with Maximum Parameter Error of 5%.

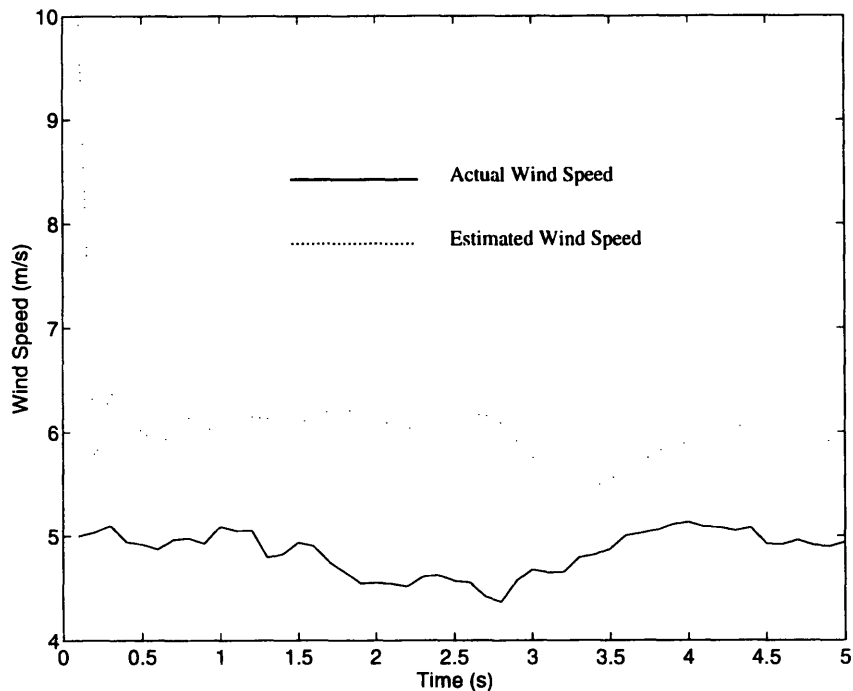


Figure 6.6. Kalman Filter Performance with Maximum Parameter Error of 10%.

With perfect knowledge of the parameters, the rms value of the estimation error is 0.75 m/s (1.68 mph). As expected, when the parameter error increases, so does the rms error of the wind estimate - the example in Figure 6.3 has a 0.78 m/s (1.73 mph) rms error, the example in Figure 6.4 has a 0.92 m/s (2.07 mph) rms error, and the example in Figure 6.5 has a 1.35 m/s (3.03 mph) rms error.

To examine how the estimation error increases as a function of error in a single parameter, two of the most important parameters were chosen: target velocity and target distance. Figures 6.7 and 6.8 show rms wind estimation error as these parameters range from 80% to 120% of their actual values. A typical ten second simulation was chosen, with an initial transverse wind speed of 5 m/s, and the estimation error was calculated over the length of the simulation.

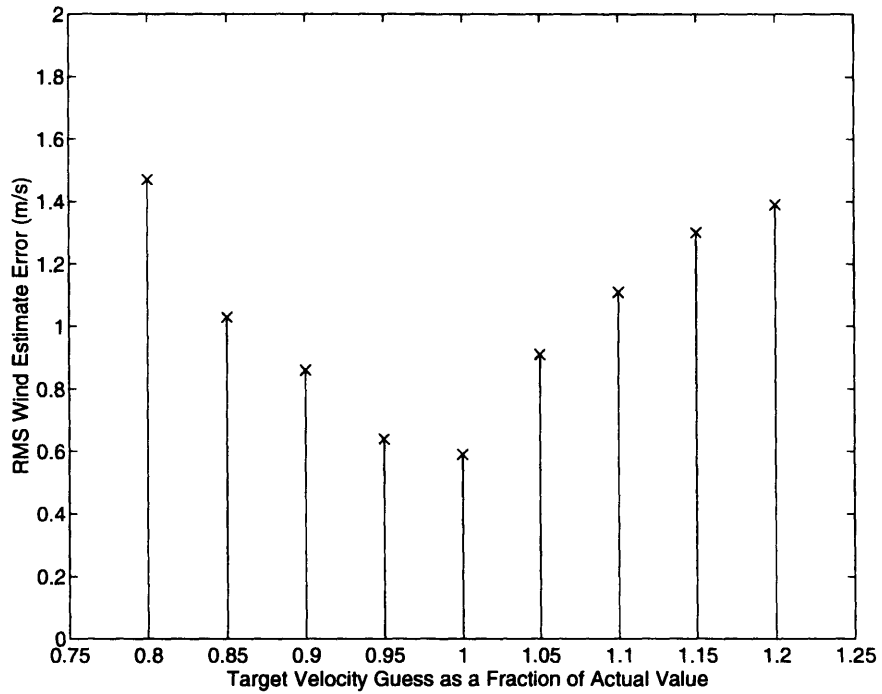


Figure 6.7. RMS Wind Estimate Error as a Function of Target Velocity Error.

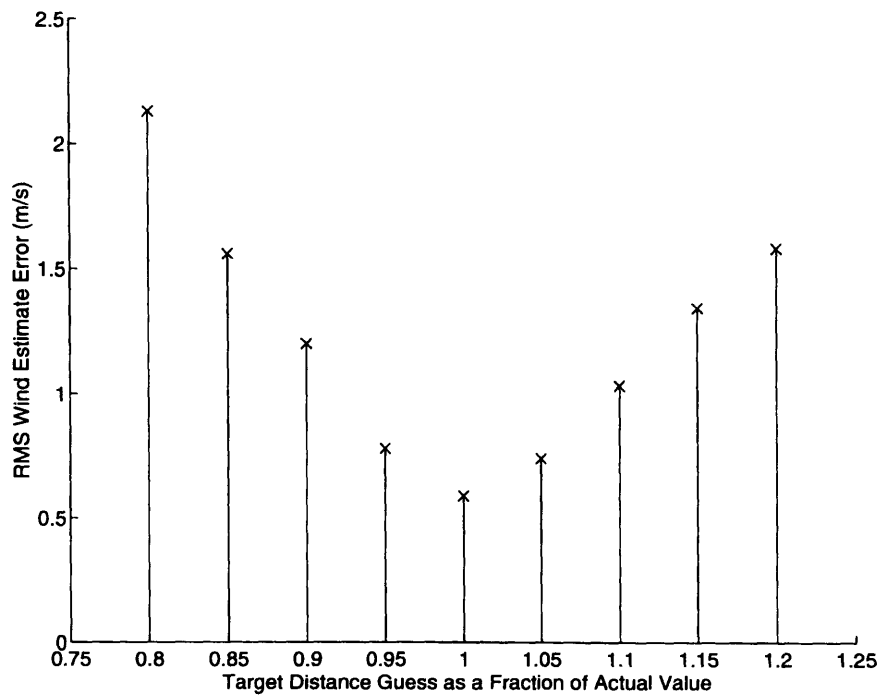


Figure 6.8. RMS Wind Estimate Error as a Function of Target Distance Error.

For a final check on the sensitivity of the estimator to errors in model parameters, ten simulations of ten seconds were taken with different levels of maximum parameter error. The three scenarios presented in Section 5.2 are used as typical examples of light, moderate, and heavy thermal blooming. Plots of estimation error mean value and variance are shown. Each 'X' represents the mean or variance of a single ten second simulation.

For light thermal blooming, the estimator was able to closely follow the wind speed only with perfect model parameters. Even with maximum parameter error constrained to be less than 10%, the estimator had errors of greater than 5 m/s (11.2 mph). As the model parameters became more corrupted, the performance of the estimator steadily decreased. Plots of estimation error mean value and variance are shown in Figure 6.9.

For moderate thermal blooming, the level of blooming increases providing a greater signal to noise ratio for the estimator. As a result, the estimation error decreases and the estimator can tolerate a greater level of model parameter error. For maximum parameter error constrained to be less than 10%, only once was the estimation error greater than 2.5 m/s (5.6 mph). Plots of estimation error mean value and variance are shown in Figure 6.10.

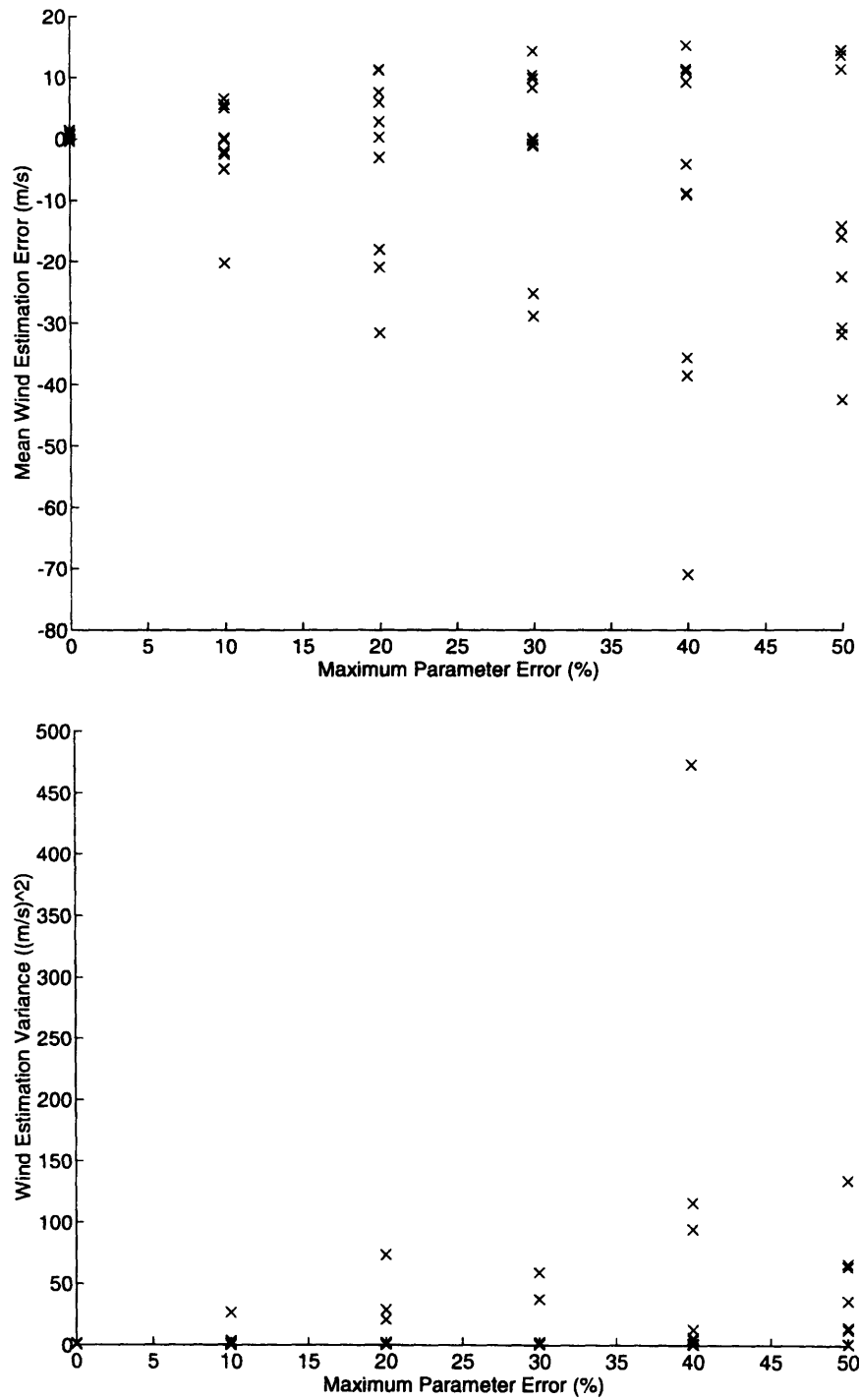


Figure 6.9. Estimation Error Statistics for Light Thermal Blooming Simulations.

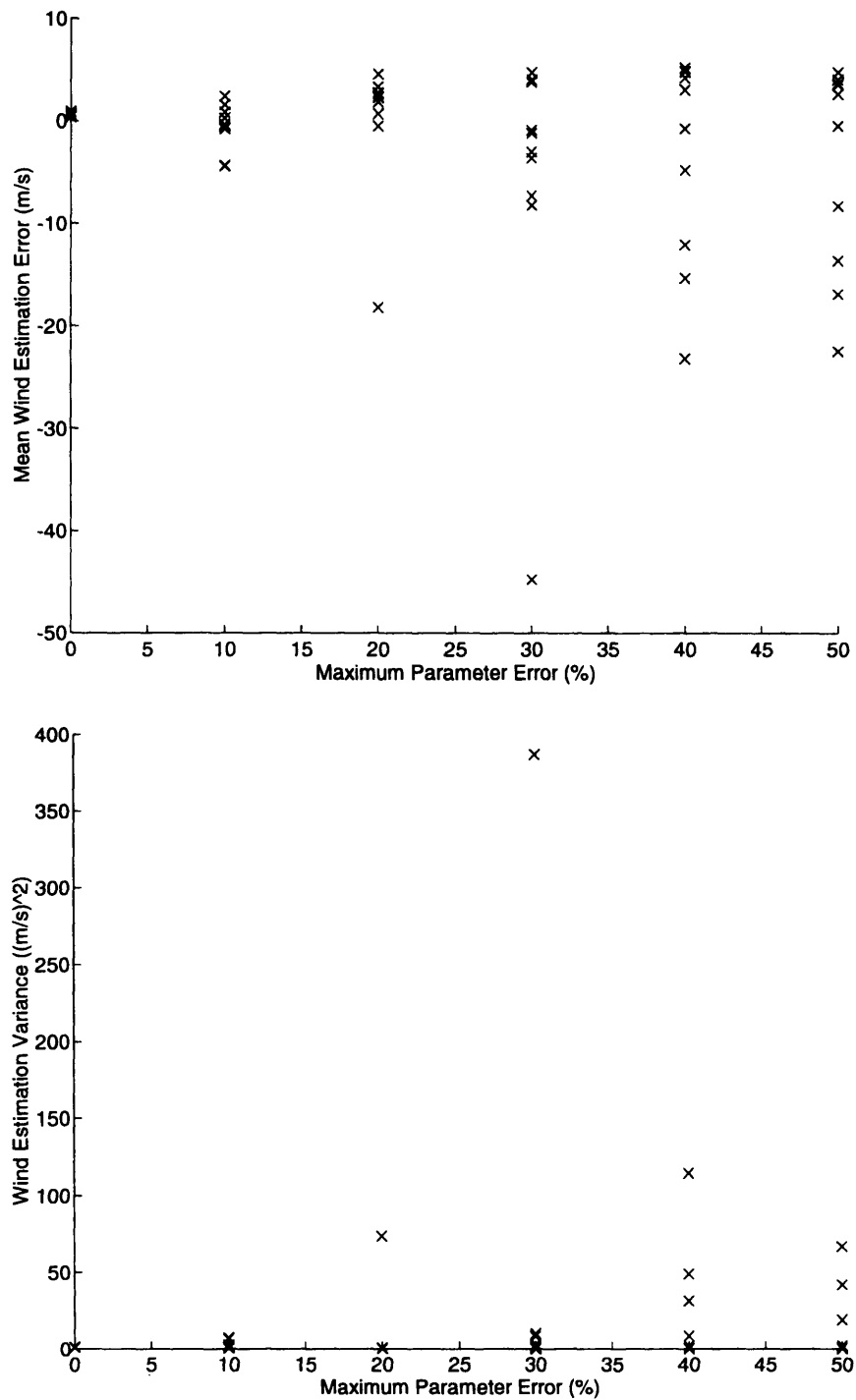


Figure 6.10. Estimation Error Statistics for Moderate Thermal Blooming Simulations.

For heavy thermal blooming, the signal to noise ratio is increased even further. However, as thermal blooming increases, the relationship between wind speed and return wavefront Zernike coefficients becomes increasingly nonlinear. This relationship is shown in Figure 6.11.

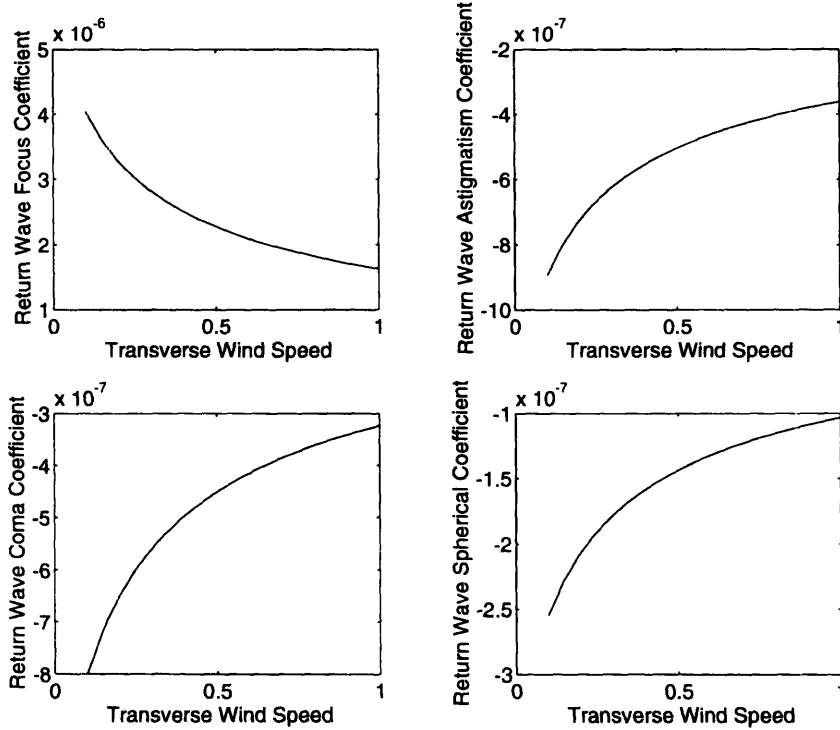


Figure 6.11 Return Wavefront Zernike Coefficients as a Function of Wind Speed.

The linearized model used in the extended Kalman filter is prone to instability. When the estimation error was bounded, for 70% of the simulations, the estimator could handle errors up to 50% in the model parameters and still keep the estimation error under 4 m/s (8.9 mph). For the other 30% of the time, the estimation error was unbounded and quickly exceeded 100 m/s (224 mph). Even with a small variance for the wind speed, the estimator performance was poor. This indicates that alternative methods of determining wind speed should be examined. Plots of estimation error mean value and variance, for the simulations with bounded estimation error, are shown in Figure 6.12.

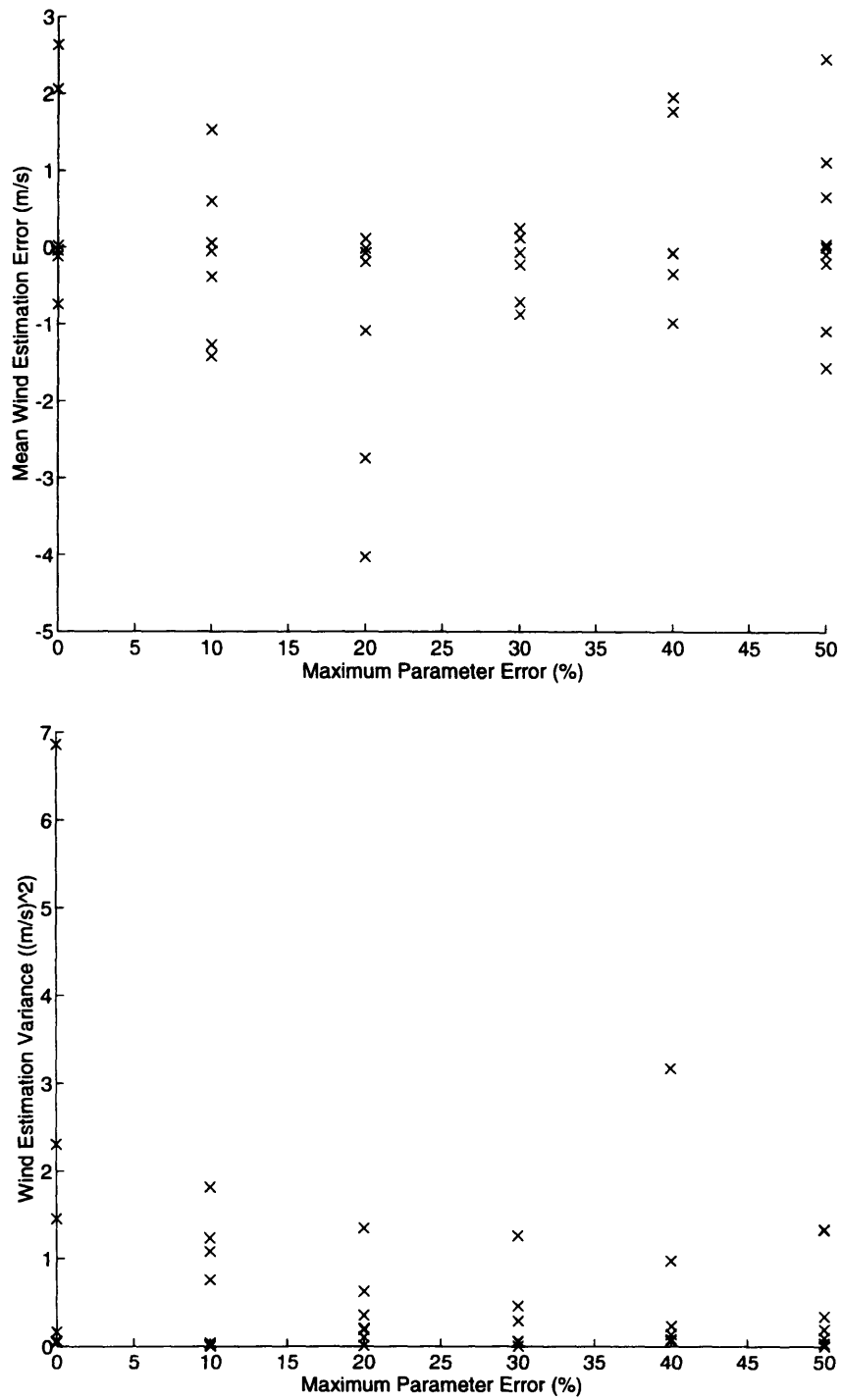


Figure 6.12. Estimation Error Statistics for Heavy Thermal Blooming Simulations.

6.4 SUMMARY

The performance of open loop and optimal focus correction control techniques with parameter uncertainty has been described. The most important parameters for optimal focus correction are target position, velocity and wind speed. Target information will be available from a radar tracking system, leaving wind speed to be determined. An extended Kalman filter was designed to estimate transverse wind velocity from return wave measurements. It has been shown that, for moderate thermal blooming, the estimator can track wind speed with less than 1.5 m/s (3.4 mph) rms error with parameter errors less than 10%. In the majority of heavy thermal blooming simulations, the estimator was able to closely track the wind speed. However, for 30% of the simulations the estimation error was unbounded and quickly exceeded 100 m/s. Relying on return laser wavefront measurements was found to be an inefficient way of estimating wind speed. Other nonlinear estimation techniques such as multiple-model or second order Gaussian filters may provide better results. Even a simple measurement device placed near the laser source would likely provide the desired degree of accuracy. The estimation of other atmospheric parameters not directly measurable would be possible using an extended Kalman filter such as described in this chapter. However, due to the insensitivity of the optimal control techniques to errors in model parameter knowledge this does not appear to be necessary. Simulations of the alternative control techniques, with the addition of model parameter errors, are presented in Chapter 7.

Chapter 7

Realistic Atmospheric Correction

This chapter demonstrates the performance of optimal focal length and optimal focal length with optimal power with model parameter errors while using an extended Kalman filter to determine the transverse wind velocity from return wave measurements. Open loop and phase conjugation methods are included for completeness. The same scenarios that were introduced in Chapter 5 will be used in this analysis.

For the first simulation in each scenario, knowledge of the parameters other than wind will be perfect so that the performance of the estimator can be examined. For the second simulation, to provide a realistic indicator of the performance of the alternative control strategies, the scenarios will be examined combining the estimated wind values with errors introduced in the other parameters.

7.1 PARAMETER UNCERTAINTY MODELS

7.1.1 ATMOSPHERIC CONSTANTS

Because the atmospheric parameters, other than wind, do not change significantly between or during an engagement, they are treated as constants. When computing the optimal corrections and within the estimator, random errors are added to the real parameter values. The errors are uniformly distributed, not to exceed 10% of the real parameter value. The same atmospheric parameter errors are used for the duration of the simulation.

7.1.2 TARGET INFORMATION

Target information is assumed to be provided by an external radar system. Because errors in target range effect all control techniques similarly, the scenarios presented in this chapter will assume perfect target range knowledge to highlight the performance of the estimator and the errors due to incorrect atmospheric knowledge.

7.1.3 WIND

As described in Section 6.2.2, the wind speed is modeled as a random walk process. The variance of the driving noise is chosen to be 0.1 to limit large changes in wind speed. At every sampling time, chosen to be 0.1 seconds in the following simulations, the wind speed is modified using the following equation

$$\text{wind}_{k+1} = \text{wind}_k + w_k \quad (7.1)$$

$$w_k \sim N(0,0.1) \quad (7.2)$$

The extended Kalman filter provides an estimate of the wind speed.

7.2 SIMULATIONS

7.2.1 LIGHT THERMAL BLOOMING

The parameters used in this scenario are identical to the parameters used in Section 5.2.1. As shown in Figure 7.1, the performance of optimal focus correction with estimated wind speed is almost identical to the perfect parameter knowledge simulation. Phase conjugation results in an average 2.8% increase in peak intensity over open loop. Optimal focus correction gives an average 8.5% increase in peak intensity over open loop. Because the system is operating to the left of the critical power point, the optimal power technique is identical to the optimal focus correction.

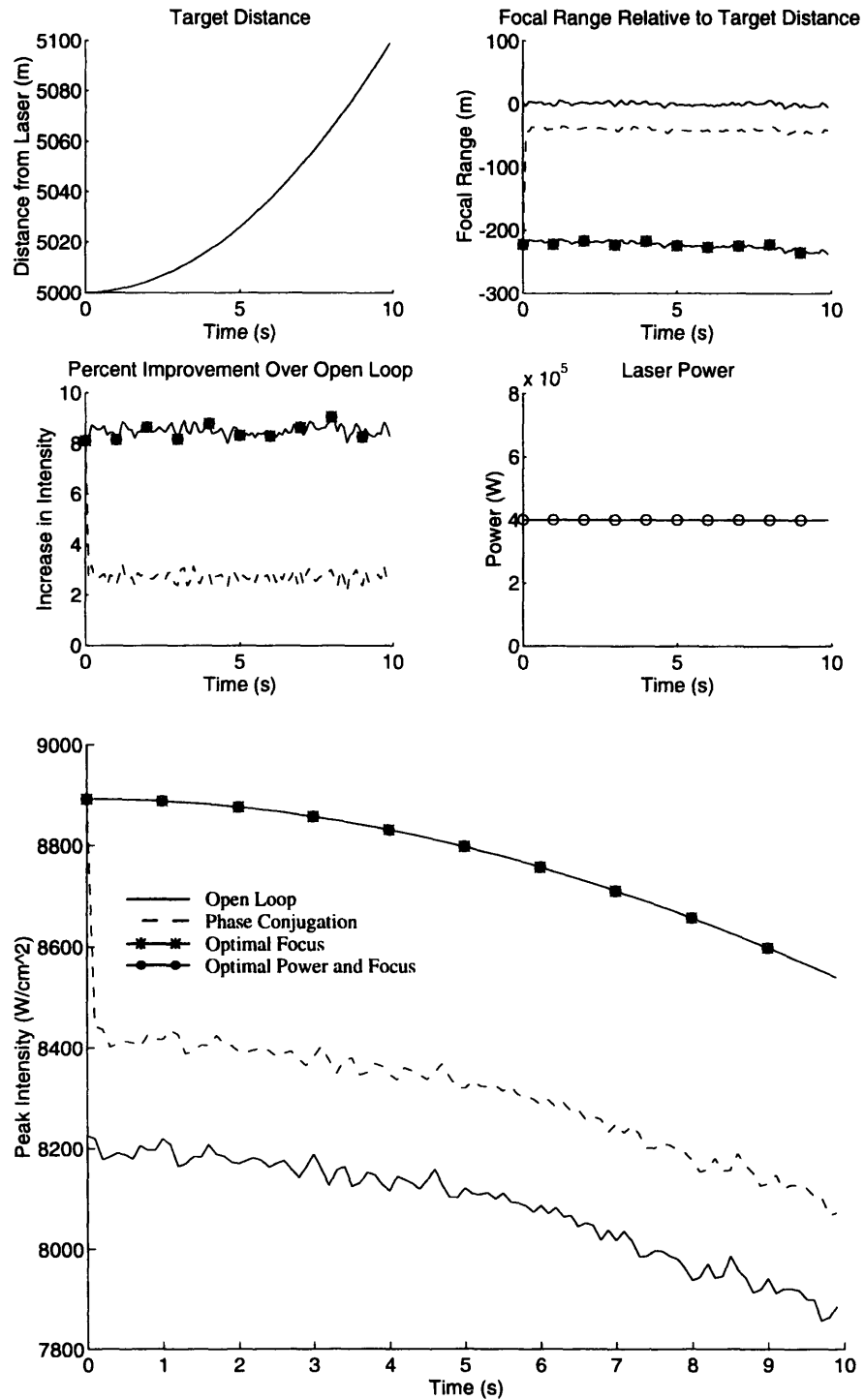


Figure 7.1. Performance Comparison for Light Thermal Blooming.

The actual and estimated wind speeds are shown in Figure 7.2. The real wind speed is plotted with a solid line and the estimate wind speed is plotted with a dotted line. The estimator is seen to accurately follow the changing wind speed. The rms wind error is 1.4 m/s (3.1 mph).

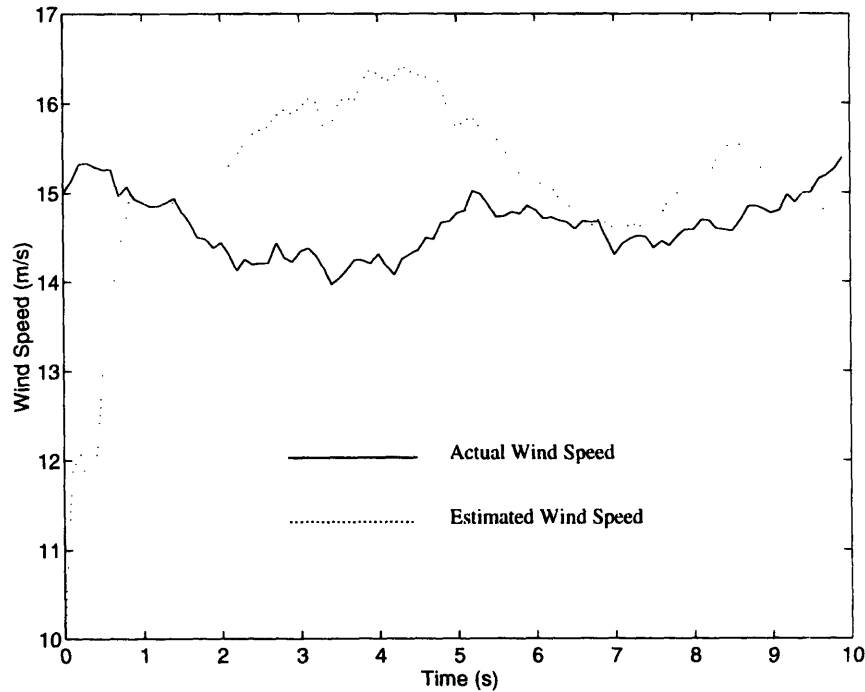


Figure 7.2. Estimator Performance for Light Thermal Blooming.

The addition of parameter errors had a very slight effect on the performance of the optimal focus correction. The increase in peak intensity over open loop decreased from 8.5% to 7.3%. Since open loop and phase conjugation techniques do not use internal models of thermal blooming, parameter errors had no effect on their performances.

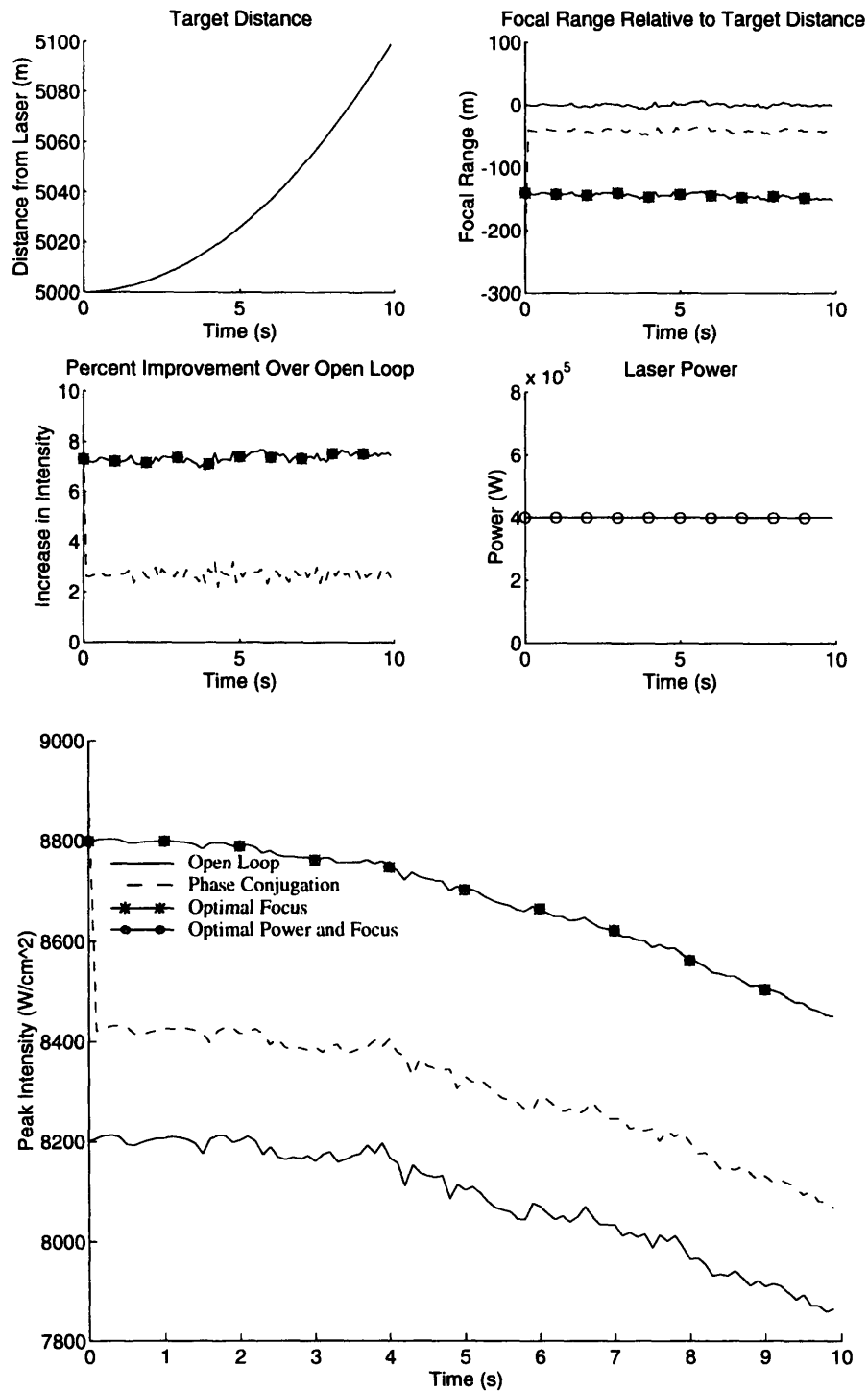


Figure 7.3. Performance Comparison for Light Thermal Blooming with Parameter Errors.

The actual and estimated wind speeds are shown in Figure 7.4. The error in model parameters creates a 11.9 m/s (26.7 mph) offset in the wind estimate. A large level of estimation error is typical for light thermal blooming scenarios as described in Section 6.3. However, even with this significant error in wind speed, the optimal focus correction still outperformed phase conjugation and open loop control methods.

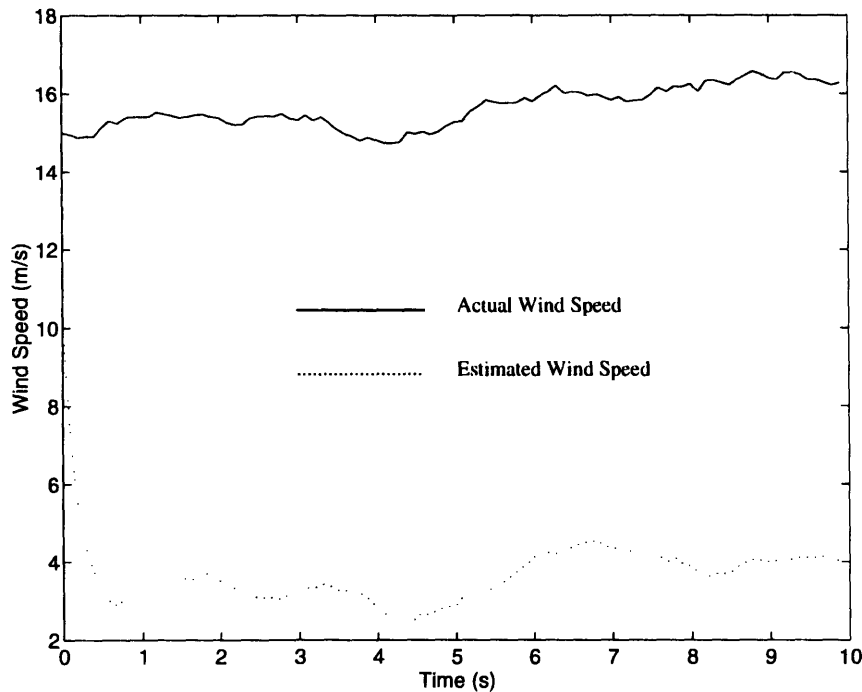


Figure 7.4. Estimator Performance for Light Thermal Blooming with Parameter Errors.

7.2.2 MODERATE THERMAL BLOOMING

For a description of the parameter values used in this scenario, refer to Section 5.2.2. As shown in Figure 7.5, the performance of optimal focus correction with estimated wind speed is almost identical to the perfect parameter knowledge simulation. Optimal focus increases peak intensity an average of 31.7% over open loop. Phase conjugation increases peak intensity an average of 10.4% over open loop. Critical power is again greater than nominal power, so the optimal power technique is identical to optimal focus correction.

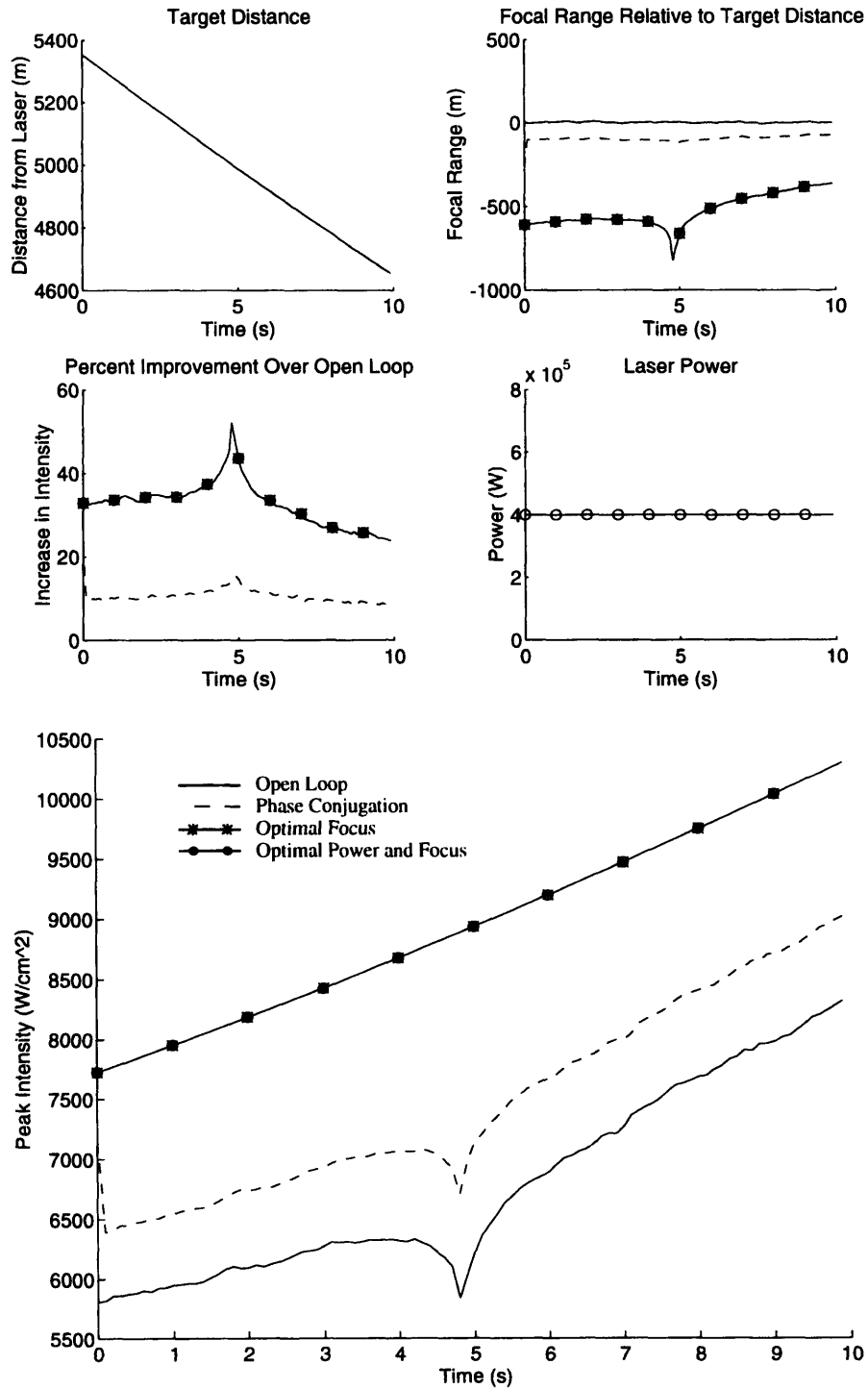


Figure 7.5. Performance Comparison for Moderate Thermal Blooming.

The actual and estimated wind speeds are shown in Figure 7.6. The estimator is seen to accurately follow the changing wind speed, but with a 1.7 m/s (3.8 mph) offset.

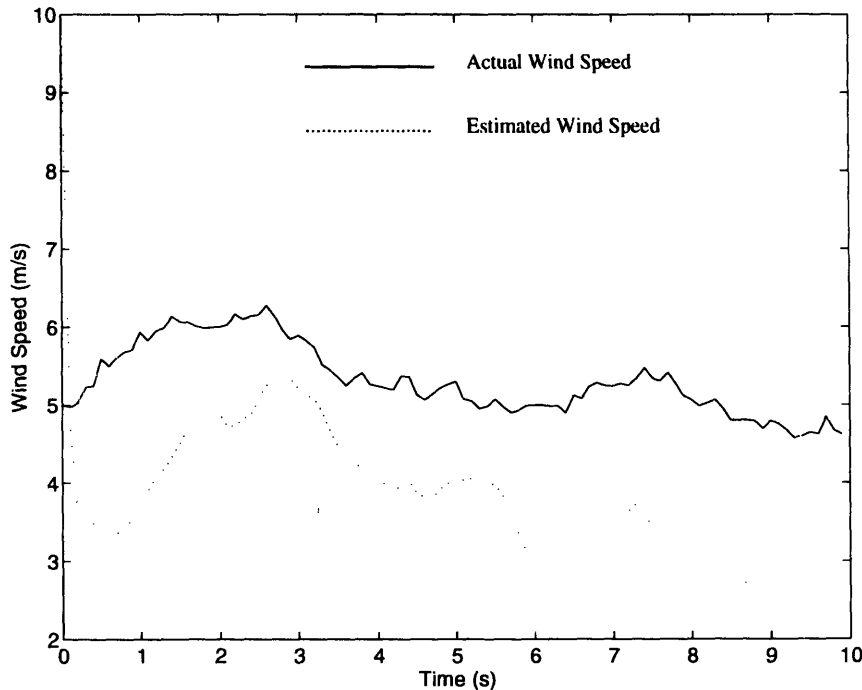


Figure 7.6. Estimator Performance for Moderate Thermal Blooming.

The addition of model parameter errors again had little effect on the performance of the optimal focus correction. Only when the laser line-of-sight was pointing directly into the wind was there a noticeable difference between performance with and without parameter errors. At this time instant, the critical power level was believed to be less than the nominal power level. As a result, the nominal power strategy reduced the laser power to 3.3×10^5 Watts. Even with this adjustment in laser power, thermal blooming was so strong due to the absence of a crosswind, the peak intensity on target dropped 50%. As soon as the target crossed above the X-axis, the critical power level once again exceeded the nominal power level and intensity jumped back up.

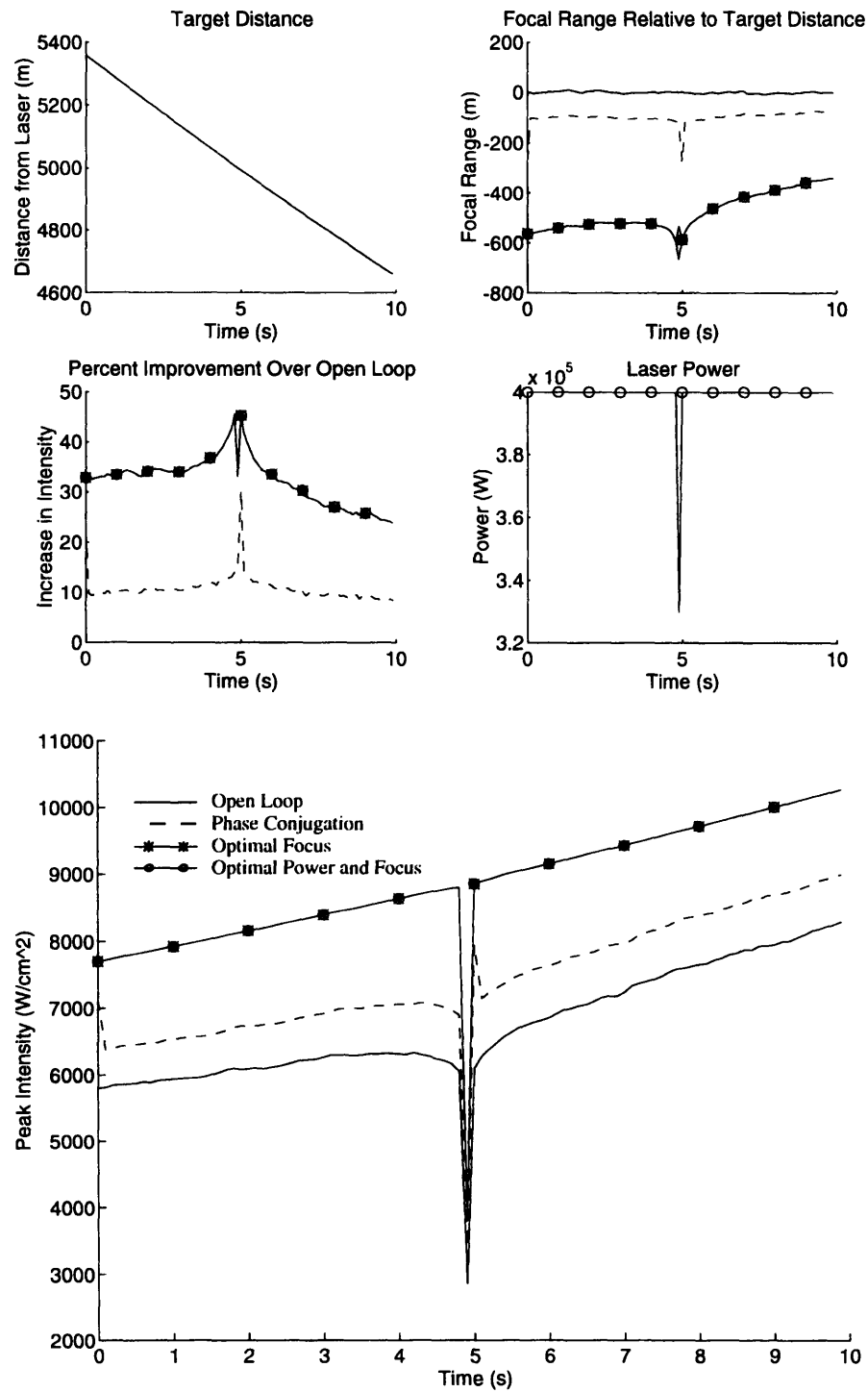


Figure 7.7. Performance Comparison for Moderate Thermal Blooming with Parameter Errors.

The actual and estimated wind speeds are shown in Figure 7.8. The uncertainty in model parameter values results in a 3.0 m/s offset in the wind estimate, much smaller than in the light thermal blooming case.

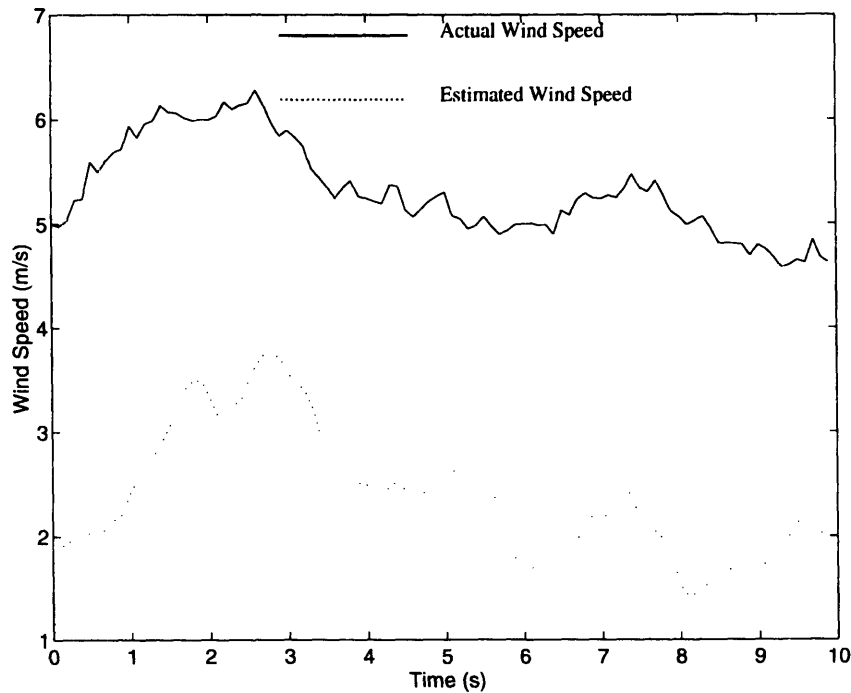


Figure 7.8. Estimator Performance for Moderate Thermal Blooming with Parameter Errors.

7.2.3 HEAVY THERMAL BLOOMING

For a description of the parameter values used in this scenario, refer to Section 5.2.3. As shown in Figure 7.9, the performance of optimal focus correction and optimal power correct with estimated wind speed are virtually identical to the corresponding performances in the perfect parameter knowledge simulations. Optimal focal length and open loop perform equally, while phase conjugation places an average of only 42.9% of the open loop intensity on target. Because critical power is now less than nominal power, the

optimal power technique gives the best performance delivering an average of 22.6% more intensity on target than open loop.

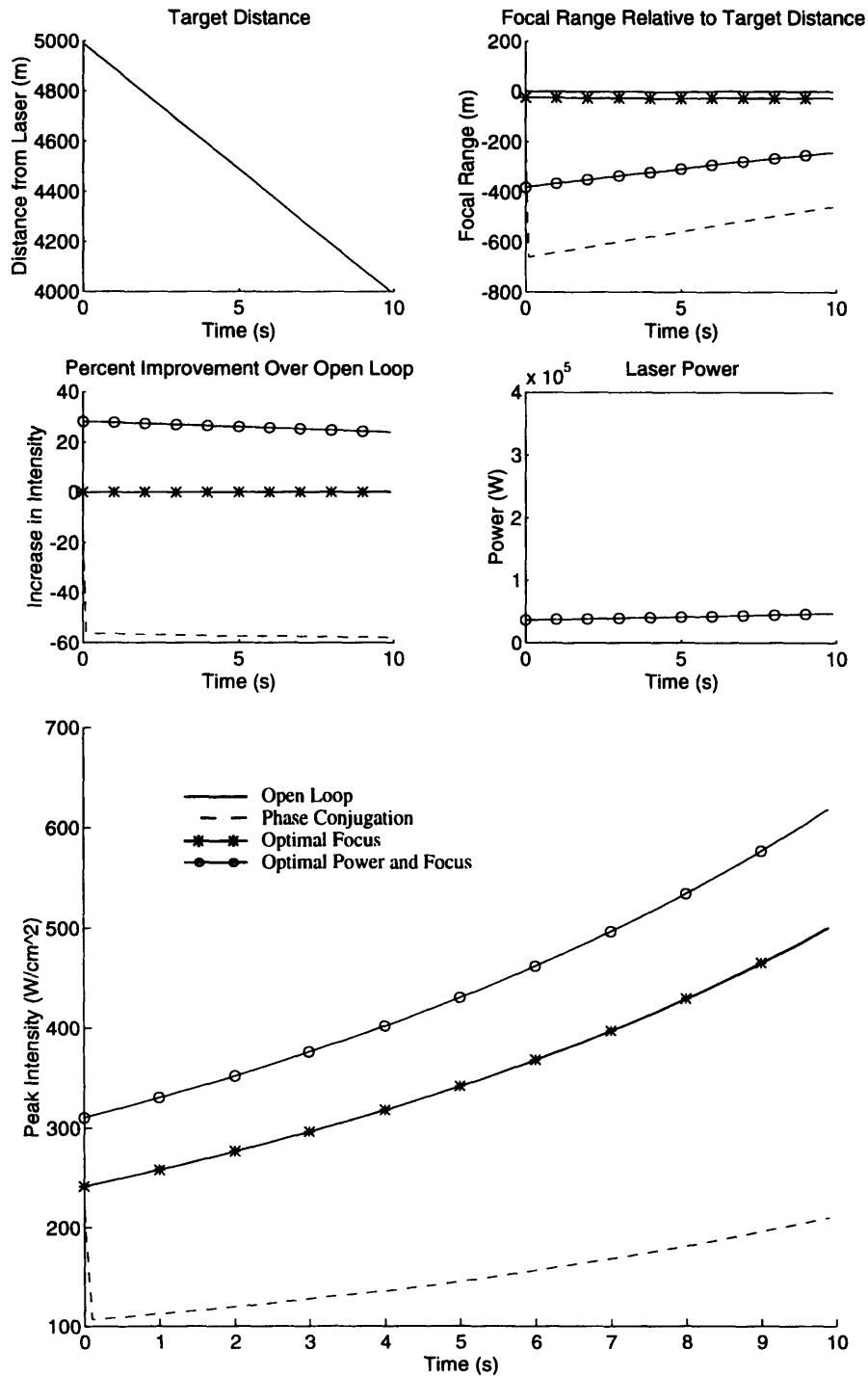


Figure 7.9. Performance Comparison for Heavy Thermal Blooming.

The actual and estimated wind speeds are shown in Figure 7.10. For the first four seconds, the estimator closely followed the wind speed, then suddenly the estimation error dramatically increased. The extended Kalman filter was designed by linearizing the nonlinear model about the nominal parameter values. In this scenario, wind speed and slewing are far from their nominal values. For high levels of thermal blooming, the nonlinearities increase and the estimator performance suffers. Recall that for heavy thermal blooming, in 30% of the simulations the estimation error was unbounded. However, even with a poor estimate of the wind speed, the optimal power correction performs significantly better than the other control techniques.

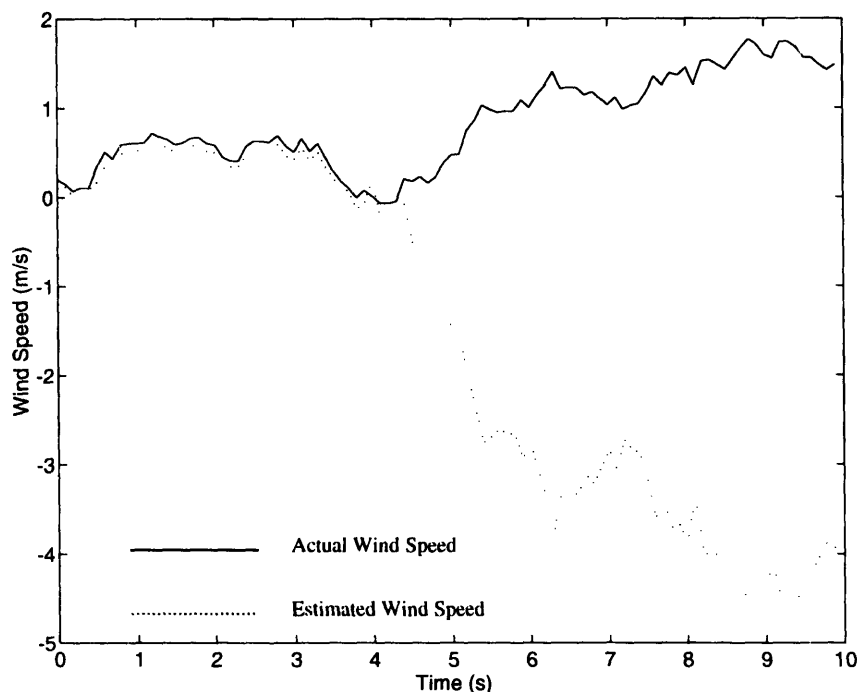


Figure 7.10. Estimator Performance for Heavy Thermal Blooming.

The introduction of parameter errors has again been shown to have little effect on performance with optimal focus correction. In this case, the optimal power correction is also seen to be insensitive to the model parameter errors.

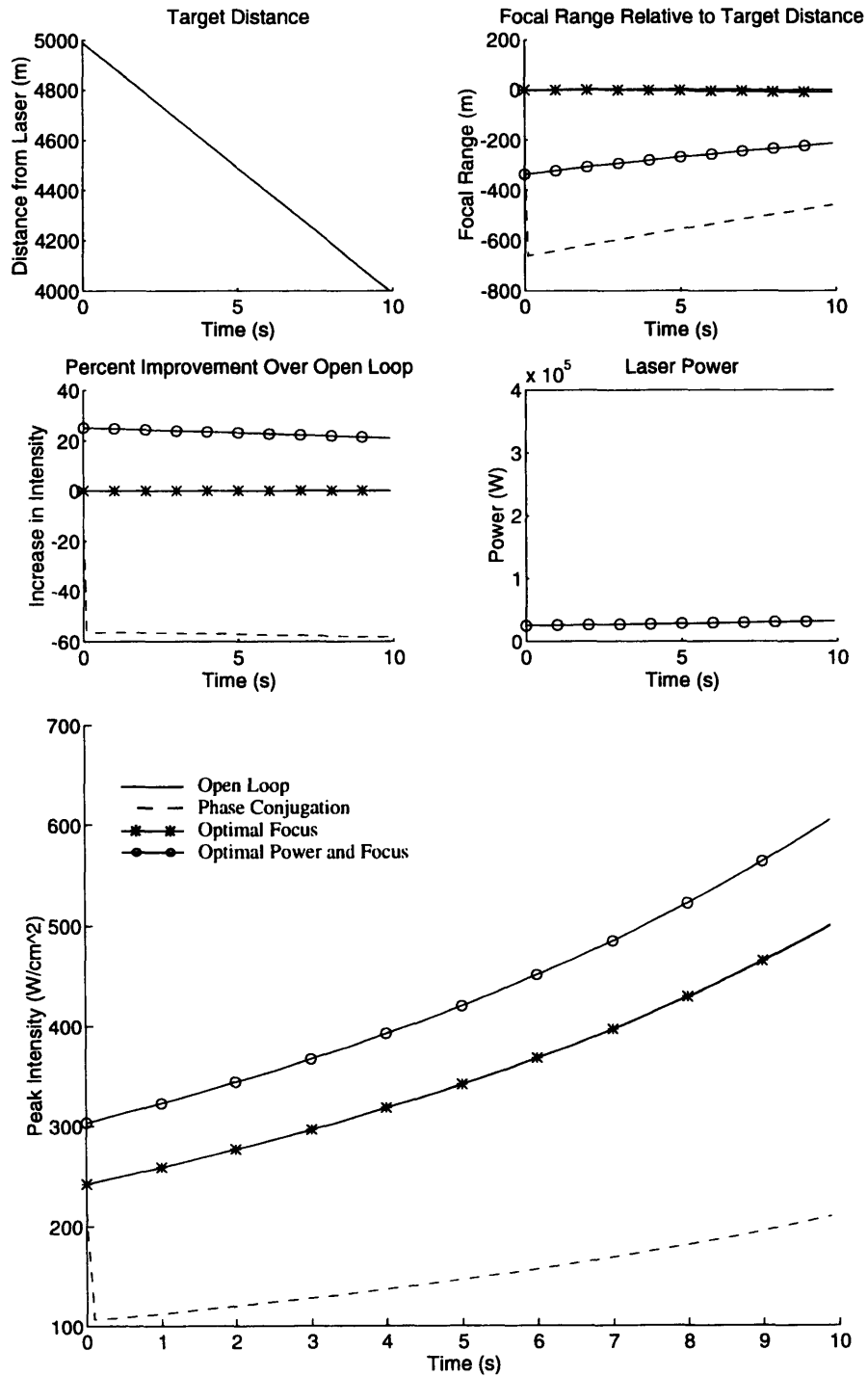


Figure 7.11. Performance Comparison for Heavy Thermal Blooming with Parameter Errors.

The actual and estimated wind speeds are shown in Figure 7.12. The rms estimation error was only 0.02 m/s. In this example the estimator was able to do an excellent job determining the wind speed, even with model parameter errors.

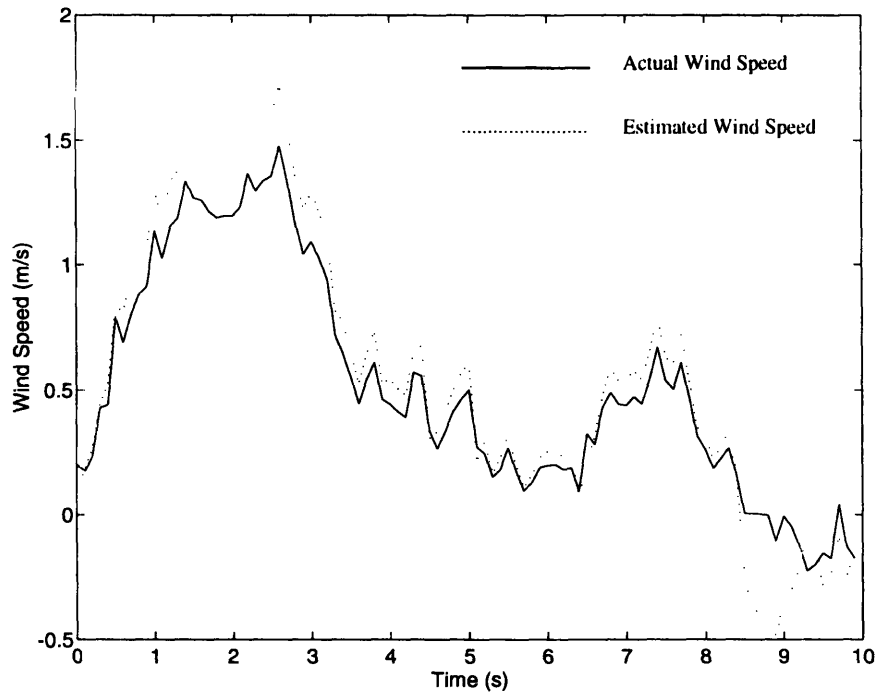


Figure 7.12. Estimator Performance for Heavy Thermal Blooming with Parameter Errors.

7.3 SUMMARY

This chapter compared the performance of the model-based, optimal focus and power strategies to open loop and phase conjugation methods. The extended Kalman filter that was designed in Chapter 6 was integrated into the new techniques to estimate the wind speed from the return wavefront measurements. Additionally, errors were introduced into the model parameters.

For light and moderate thermal blooming, the estimator was able to follow the actual wind speed reasonably well for small levels of parameter error. When significant errors were

introduced into the model parameters, larger offsets were observed in the wind estimates. For heavy thermal blooming, the estimator was able to closely follow the wind speed for parts of the simulation, but sometimes the estimation error rapidly increased. Heavy thermal blooming has the advantage of a high signal-to-noise ratio for the estimator, but the associated increase in nonlinearities can result in severe performance degradation. A simple anemometer placed near the laser aperture, where the majority of thermal blooming occurs, would likely perform more accurately than the estimator over a wider range of operating conditions.

Even with the difficulty in estimating the wind speed, and the introduction of model parameter errors, the optimal focus and optimal power correction techniques consistently performed better than the traditional open loop and phase conjugation methods. For heavy thermal blooming, phase conjugation was found to significantly over compensate for blooming and placed less than half the intensity on target compared to open loop. By turning down the laser power, the optimal power technique resulted in an increase of peak intensity 30% over open loop.

Chapter 8

Conclusions

This chapter presents the conclusions of the design effort and makes recommendations on future work.

8.1 CONCLUSIONS

A model for thermal blooming was described that determines the peak intensity and laser profile on target in terms of nineteen atmospheric, laser, and target parameters. Atmospheric parameters include wind speed, air density, and absorption coefficients. Laser parameters include aperture radius, power, and wavelength. Target parameters describe the target's position and velocity.

A model for atmospheric turbulence was described that determines the turbulence aberration in terms of the first twenty Zernike modes in terms of six parameters: transverse wind velocity, transverse target velocity, target distance, Kolmogorov turbulence constant, and aperture radius.

The traditional control strategies for a high-energy laser - open loop and phase conjugation - were compared to the two novel, model-based approaches: optimal focus correction and optimal power with optimal focus correction. The performance of the four systems was compared during light, moderate, and heavy thermal blooming scenarios. The model parameters were perfectly known so that an upper bound for the model-based control techniques could be established. For light thermal blooming, the critical power level exceeded the nominal power level, so the two optimal control techniques were identical. Phase conjugation resulted in a 2.5% increase in peak intensity over open loop, while optimal focus increased peak intensity 8% over open loop. As the degree of thermal blooming increased, so did the benefits of using the alternative control techniques. For moderate thermal blooming, once again the critical power level exceeded the nominal power level, so the two optimal control techniques were identical. Phase conjugation resulted in a 10% increase in peak intensity over open loop, while optimal focus increased peak intensity up to 45% over open loop. In the heavy thermal blooming scenario, the critical power level fell below the nominal power level, so peak intensity on target could actually be increased by turning down the laser power. The optimal focus strategy and open loop resulted in virtually the same level of peak intensity on target, while phase conjugation performed poorly placing less than half of the peak intensity on target as compared to open loop. By turning down the laser power, the optimal power strategy was able to increase peak intensity up to 30% more than open loop.

The sensitivity of the model-based techniques to errors in the model parameters was examined. The majority of parameters are atmospheric constants that can be measured at the start of the day or entered from a table. However, the transverse wind speed, and the transverse and axial target speed and distance continuously change. It was assumed that a radar system provides target information, so wind speed was the only parameter that must

be estimated or measured. An extended Kalman filter was designed to estimate the wind speed from return wavefront Zernike coefficients. The estimator was evaluated both with and without model parameter errors. It was found to have difficulty accurately determining the wind speed.

Finally, the four control strategies were compared once again, but instead of having perfect parameter knowledge, errors were introduced into the model parameters. The estimator was used to estimate the wind speed. The performance of the various control techniques was compared using the same light, moderate, and heavy thermal blooming scenarios that were presented in the perfect knowledge chapter. Even with large estimation errors and errors introduced into the model parameters, the optimal correction techniques performed significantly better than the traditional open loop and phase conjugation methods.

8.2 RECOMMENDATIONS

Alternative methods of determining the wind speed should be examined. Possibly a simple anemometer would provide the required accuracy.

The optimal focus correction technique described in this thesis should be extended to other Zernike modes, such as astigmatism, coma, and spherical. It would be interesting to determine if these modes require nonlinear correction as does the focus term, or if the optimal correction is simply phase conjugation.

The extent to which the actual high-energy lasers under consideration allow for power throttling should be examined. Note that for high levels of thermal blooming, no significant increase in peak intensity could be achieved without decreasing laser power.

The analysis could be extended from a ground-based system to an airborne system. It appears that thermal blooming would be much less of a problem for an airborne system

because of the high velocity of the laser system itself. This movement would guarantee an influx of unheated air into the laser path and be similar to a high slew rate or transverse wind speed for a ground-based system.

Finally, the performance of the optimal correction techniques should be examined experimentally on a high-energy laser system. If using an actual high-energy laser is not feasible, this analysis could be done with a detailed wave propagation computer model. If the actual laser system is as insensitive to model parameter errors as this research has suggested, the return wavefront sensor could be eliminated.

Appendix A

Zernike Polynomials

The first twenty Zernike polynomials [17] are presented in Table A.1 and plotted in the figures that follow. The first figure in each pair is the three-dimensional wavefront, the second is the corresponding contour plot.

TABLE A.1. Zernike Polynomial Functions.

| i | $P_i(r, \theta)$ | i | $P_i(r, \theta)$ |
|----------------|---------------------------|-----|------------------------------------|
| 1 X-Tilt | $r \cos \theta$ | 11 | $(4r^4 - 3r^2) \cos 2\theta$ |
| 2 Y-Tilt | $r \sin \theta$ | 12 | $(4r^4 - 3r^2) \sin 2\theta$ |
| 3 Defocus | $2r^2 - 1$ | 13 | $r^4 \cos 4\theta$ |
| 4 Astigmatism | $r^2 \cos 2\theta$ | 14 | $r^4 \sin 4\theta$ |
| 5 Astigmatism | $r^2 \sin 2\theta$ | 15 | $(10r^5 - 12r^3 + 3r) \cos \theta$ |
| 6 Primary Coma | $(3r^3 - 2r) \cos \theta$ | 16 | $(10r^5 - 12r^3 + 3r) \sin \theta$ |
| 7 Primary Coma | $(3r^3 - 2r) \sin \theta$ | 17 | $(5r^5 - 4r^3) \cos 3\theta$ |
| 8 Trefoil Coma | $r^3 \cos 3\theta$ | 18 | $(5r^5 - 4r^3) \sin 3\theta$ |
| 9 Trefoil Coma | $r^3 \sin 3\theta$ | 19 | $r^5 \cos 5\theta$ |
| 10 Spherical | $6r^4 - 6r^2 + 1$ | 20 | $r^5 \sin 5\theta$ |

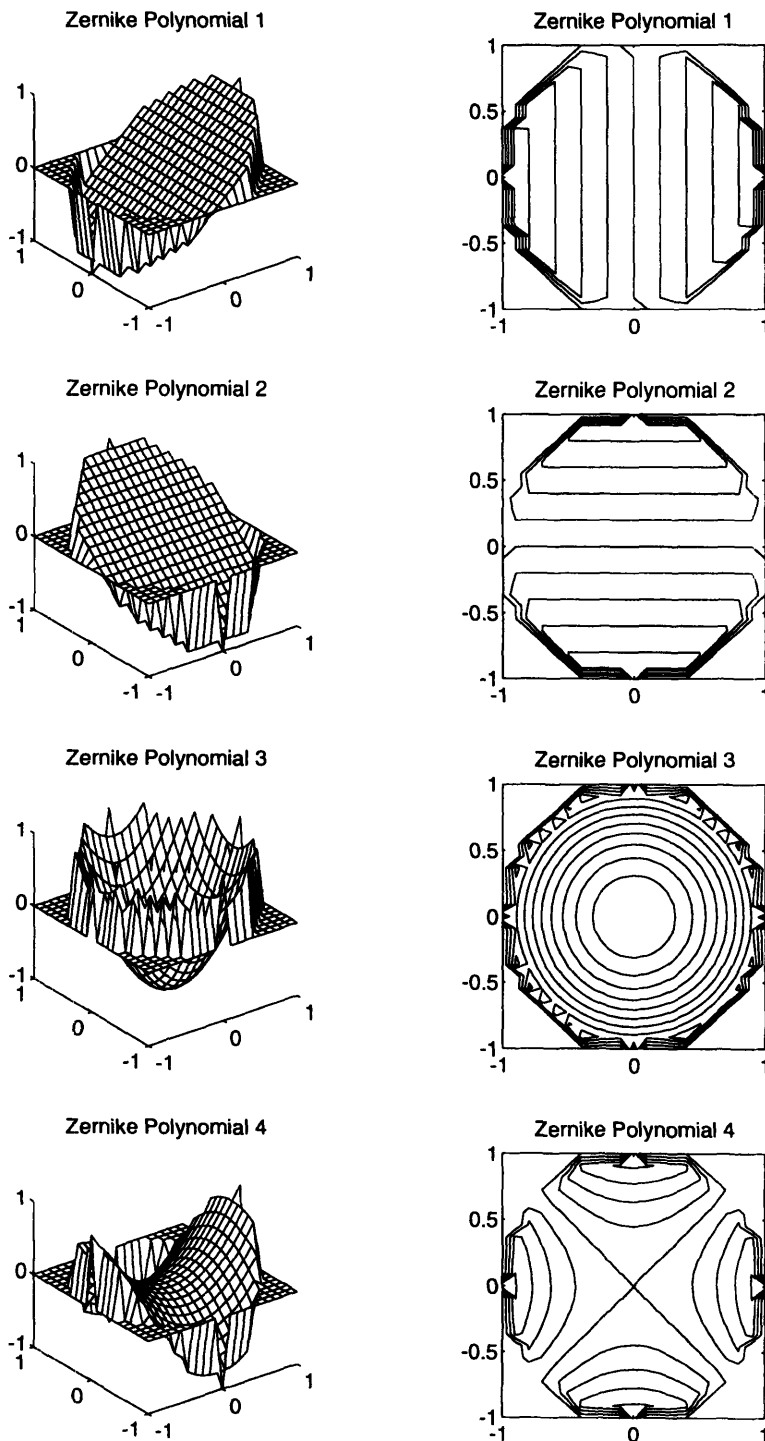


Figure A.1. Zernike Polynomial Functions 1-4.

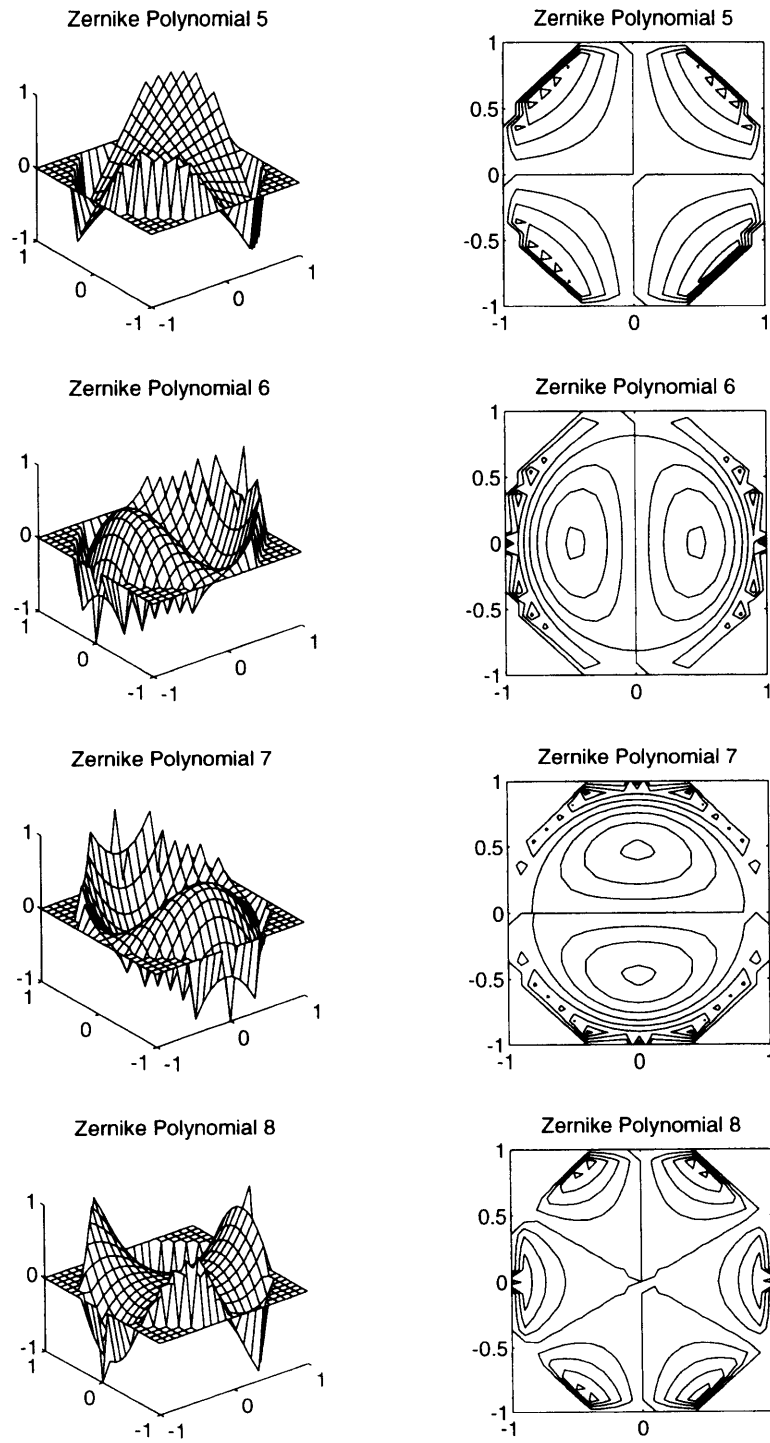


Figure A.2. Zernike Polynomial Functions 5-8.

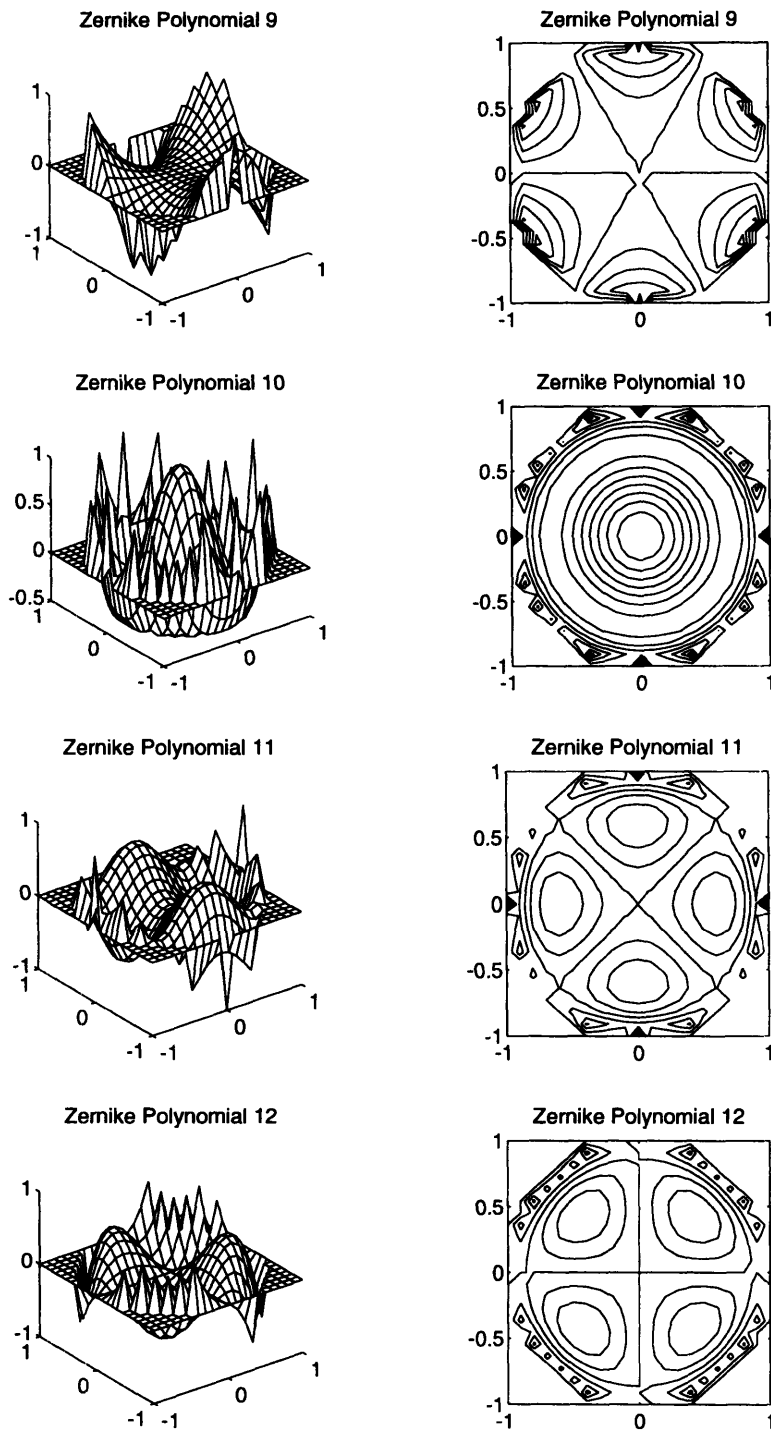


Figure A.3. Zernike Polynomial Functions 9-12.

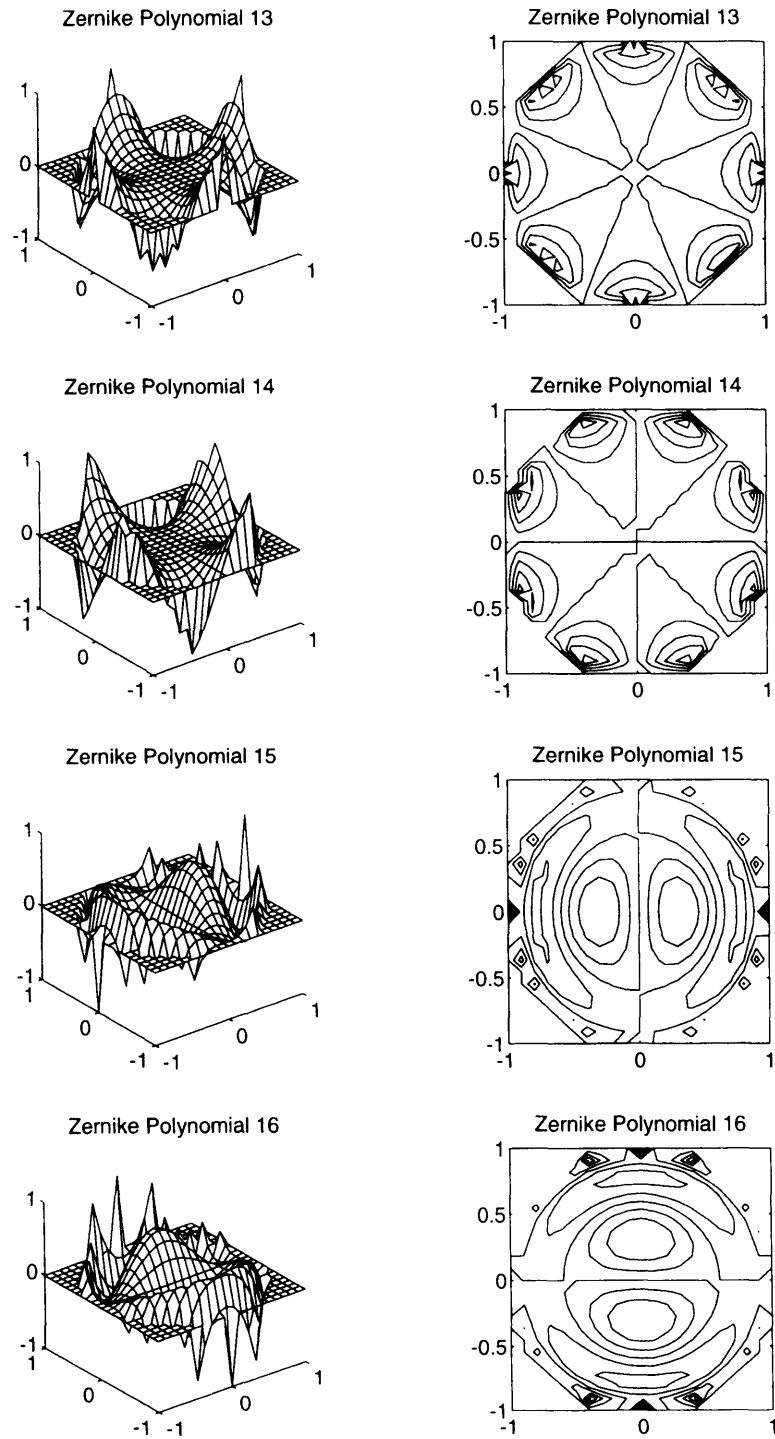


Figure A.4. Zernike Polynomial Functions 13-16.

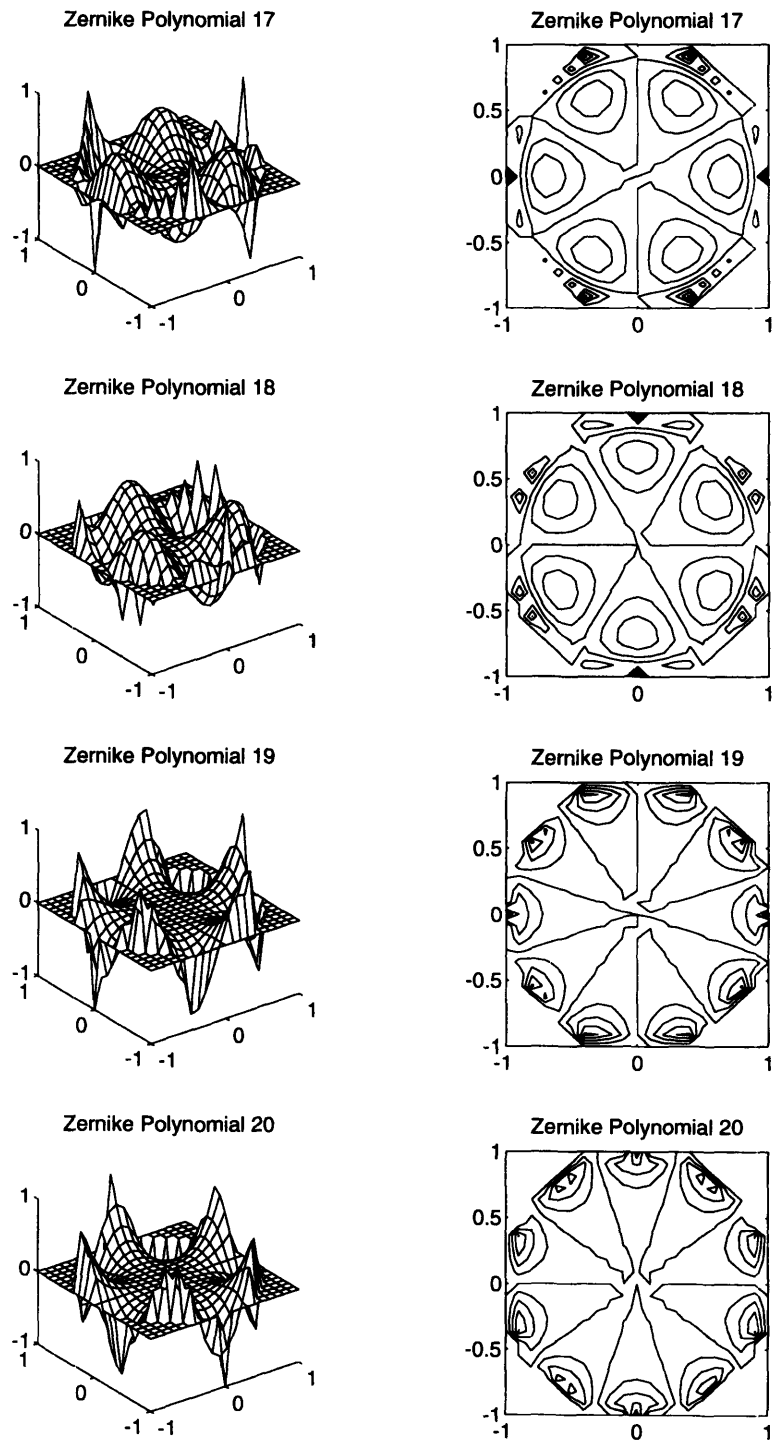





Figure A.5. Zernike Polynomial Functions 17-20.

Appendix B

Parameter Sensitivity

Peak intensity, Zernike focus coefficient, and Zernike coma coefficient are plotted as functions of each parameter as the parameter takes on values from 50% less than its nominal value to 50% greater than its nominal value. Only parameters that have the possibility of changing between or during engagements are presented. The parameter - intensity plot has three lines: optimal power with known parameters, optimal power with nominal parameters, and open loop with nominal target distance.

The following convention, consistent with the plots given in Chapter 6, is used to represent optimal focus correction with and without perfect parameter knowledge and open loop control

-  Optimal Focus, Actual Parameters
-  Optimal Focus, Nominal Parameters
-  Open Loop, Nominal Parameters

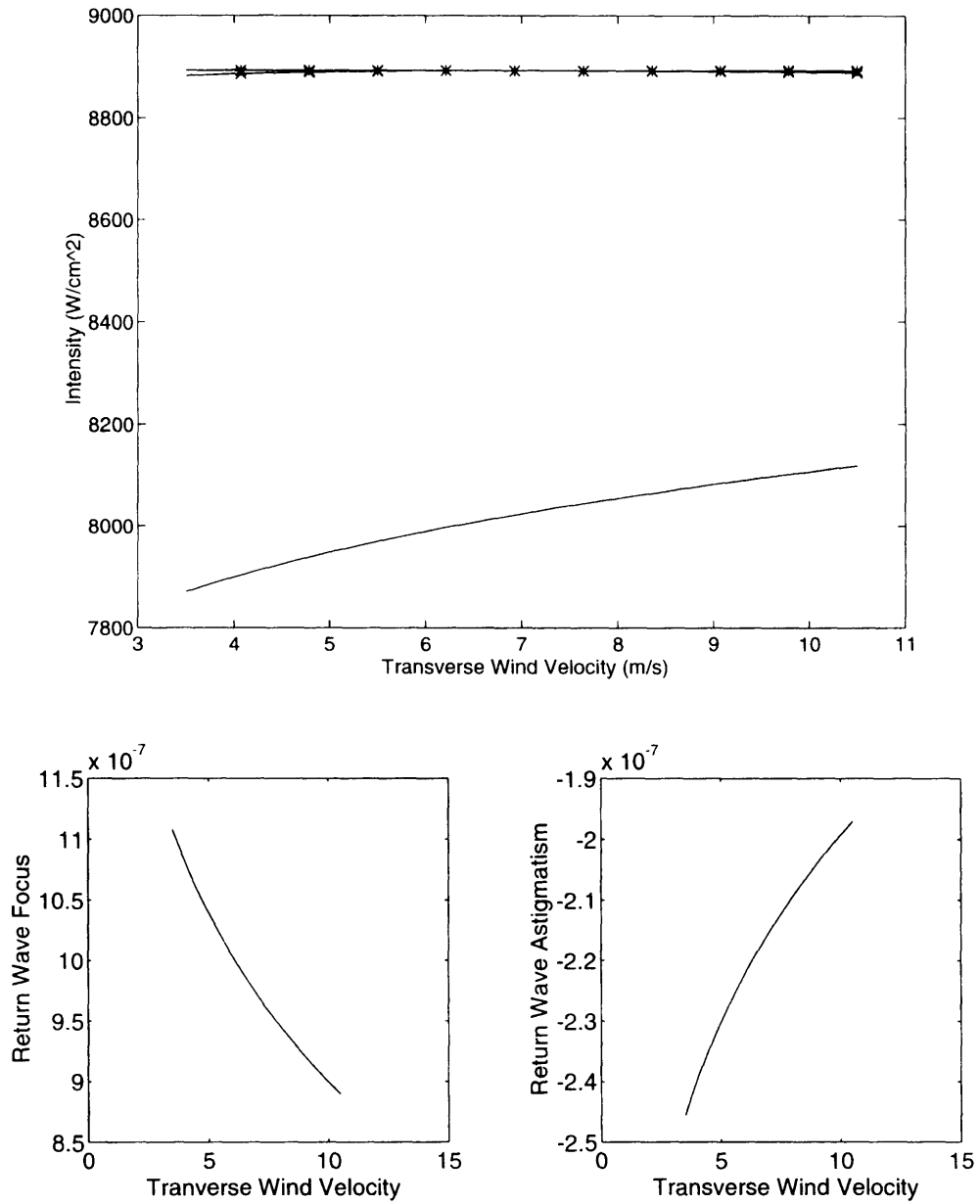


Figure B.1. Sensitivity to Transverse Wind Velocity.

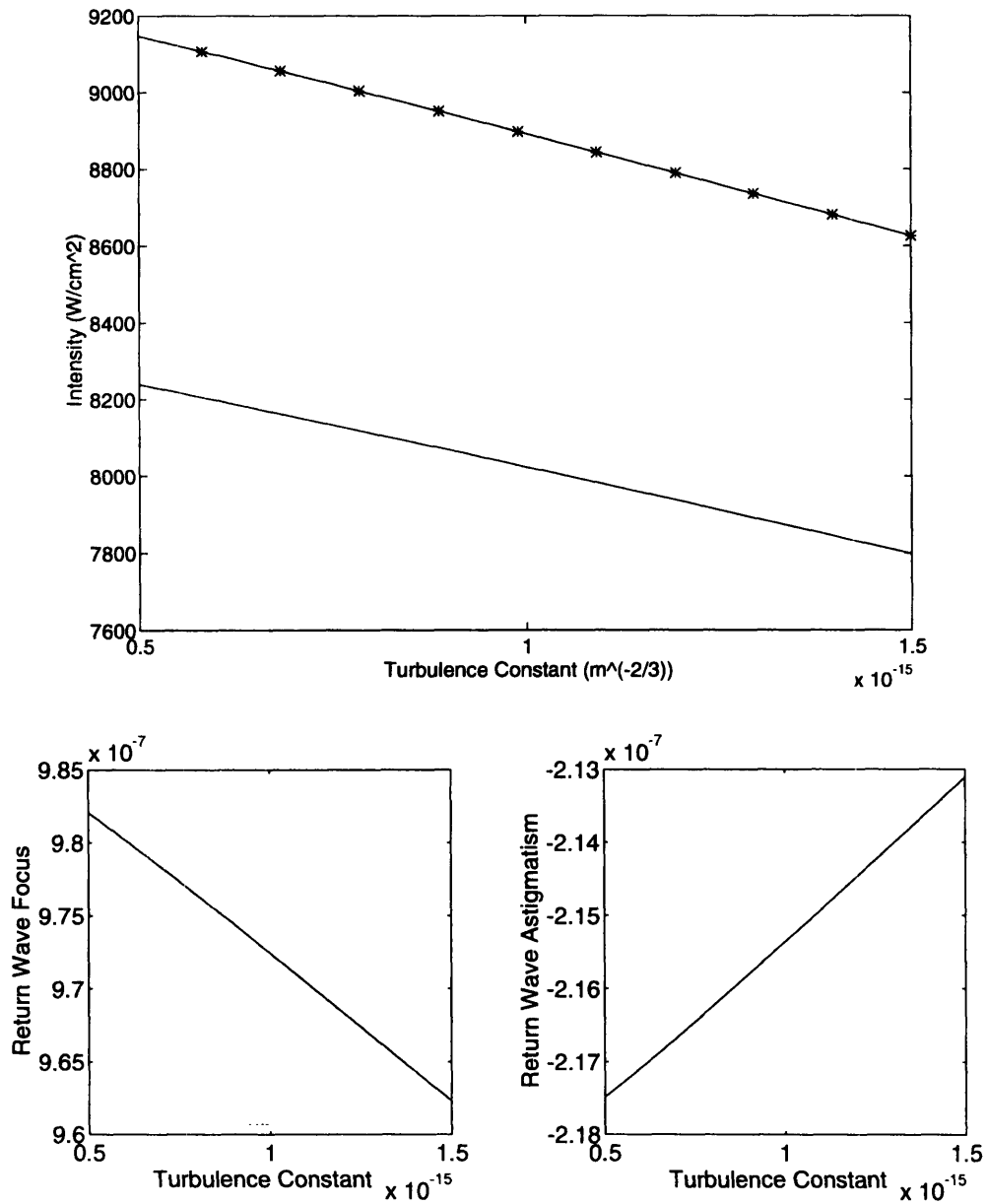


Figure B.2. Sensitivity to Turbulence Constant.

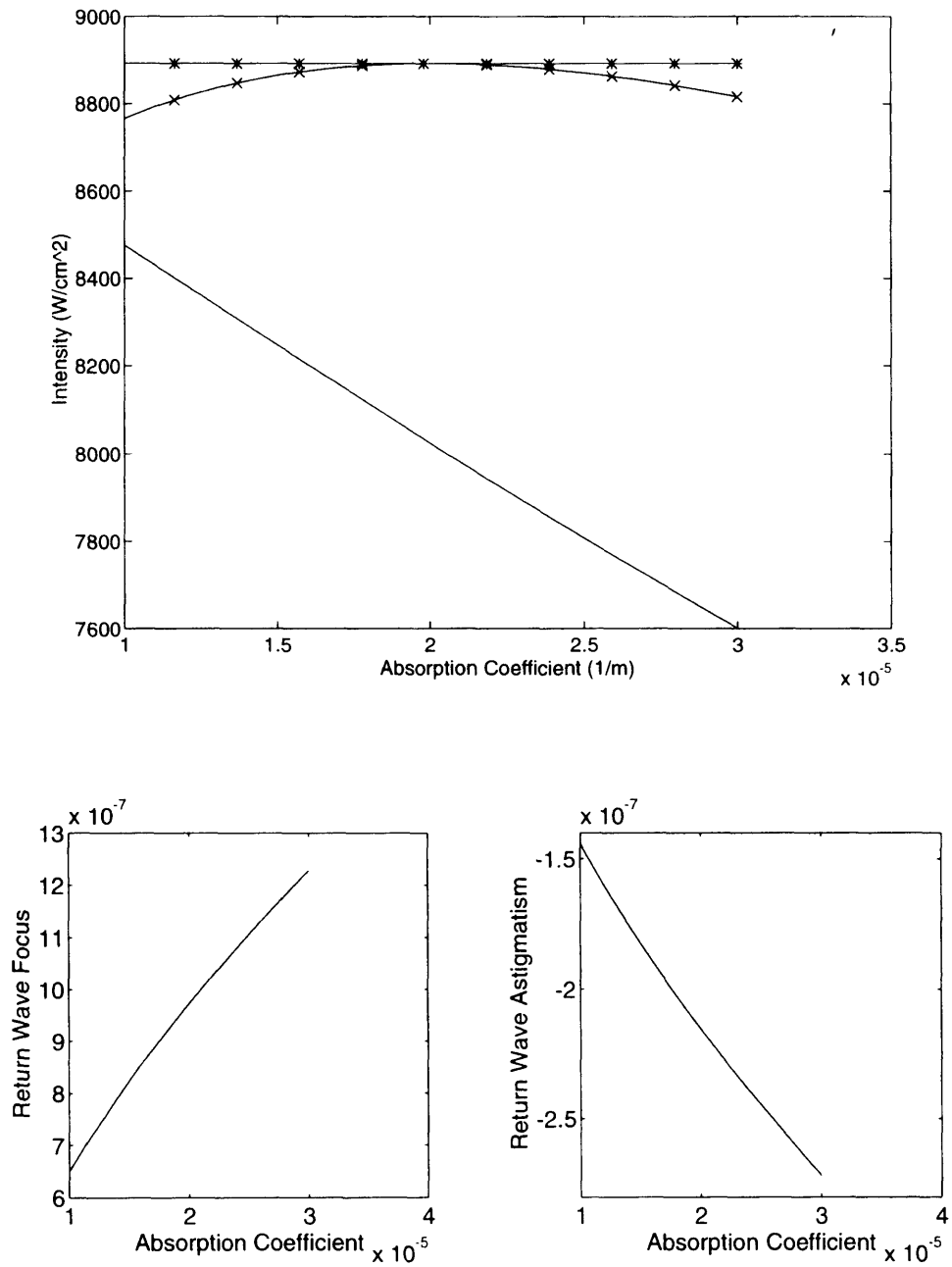


Figure B.3. Sensitivity to Absorption Coefficient.

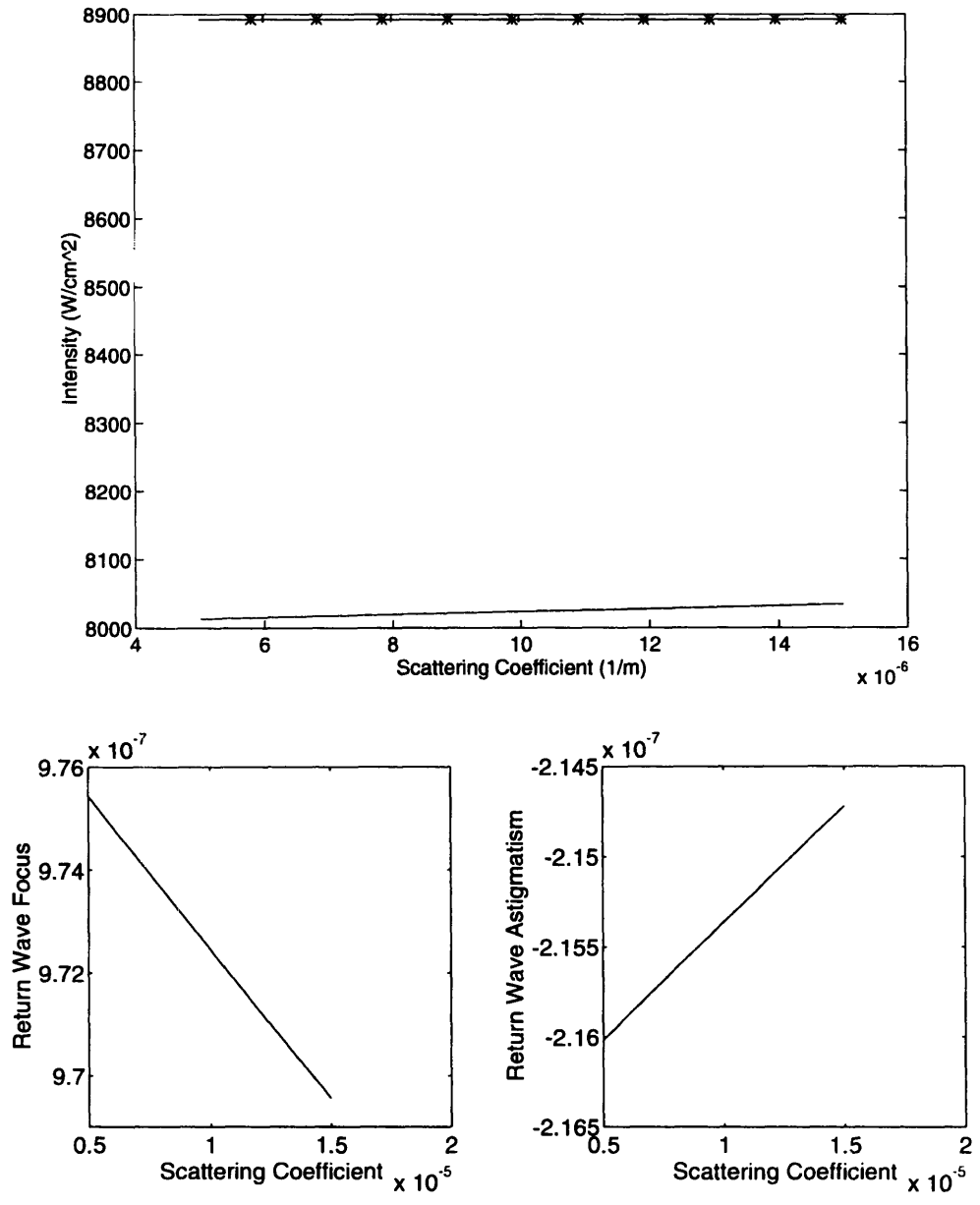


Figure B.4. Sensitivity to Scattering Coefficient.

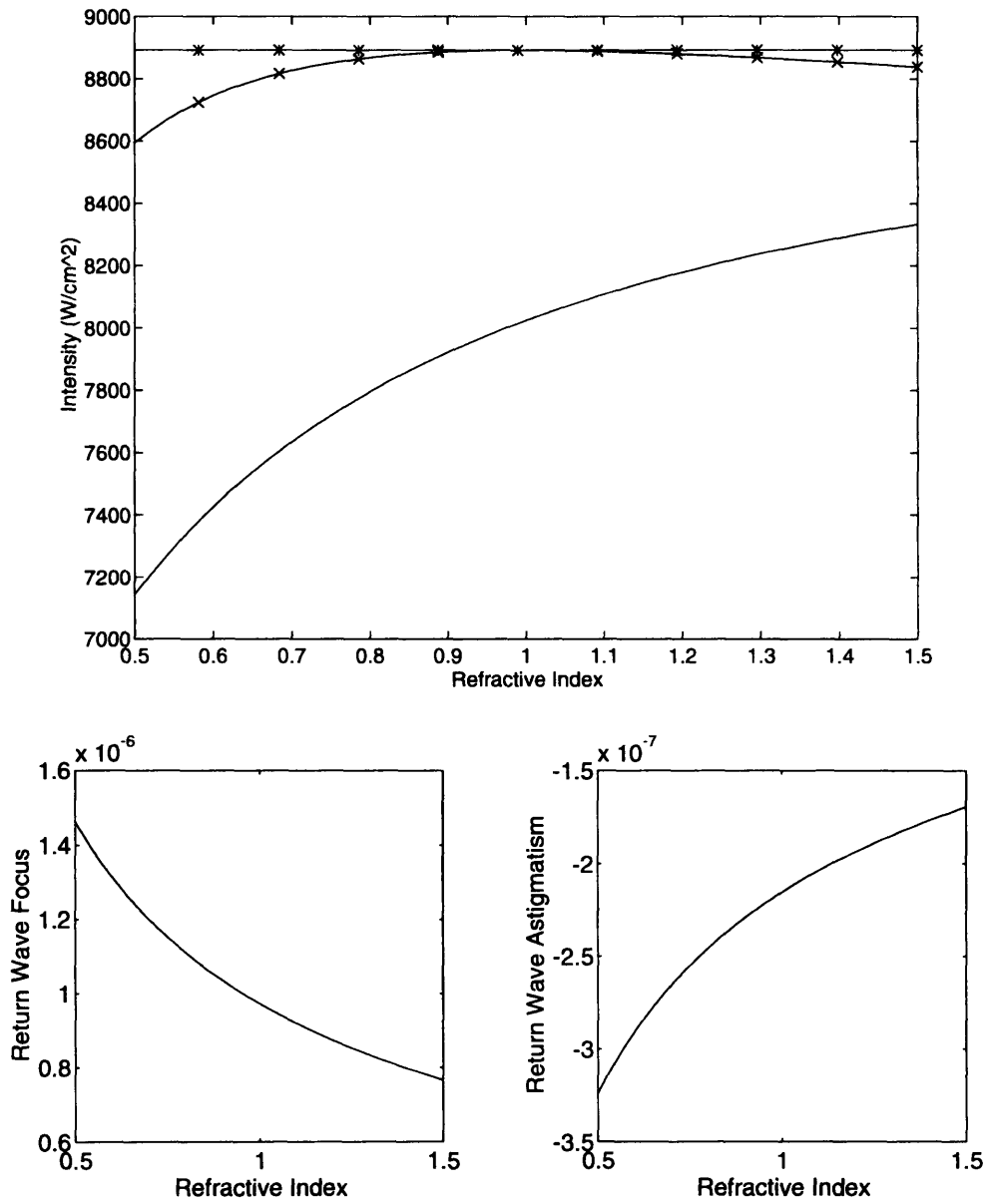


Figure B.5. Sensitivity to Refractive Index.

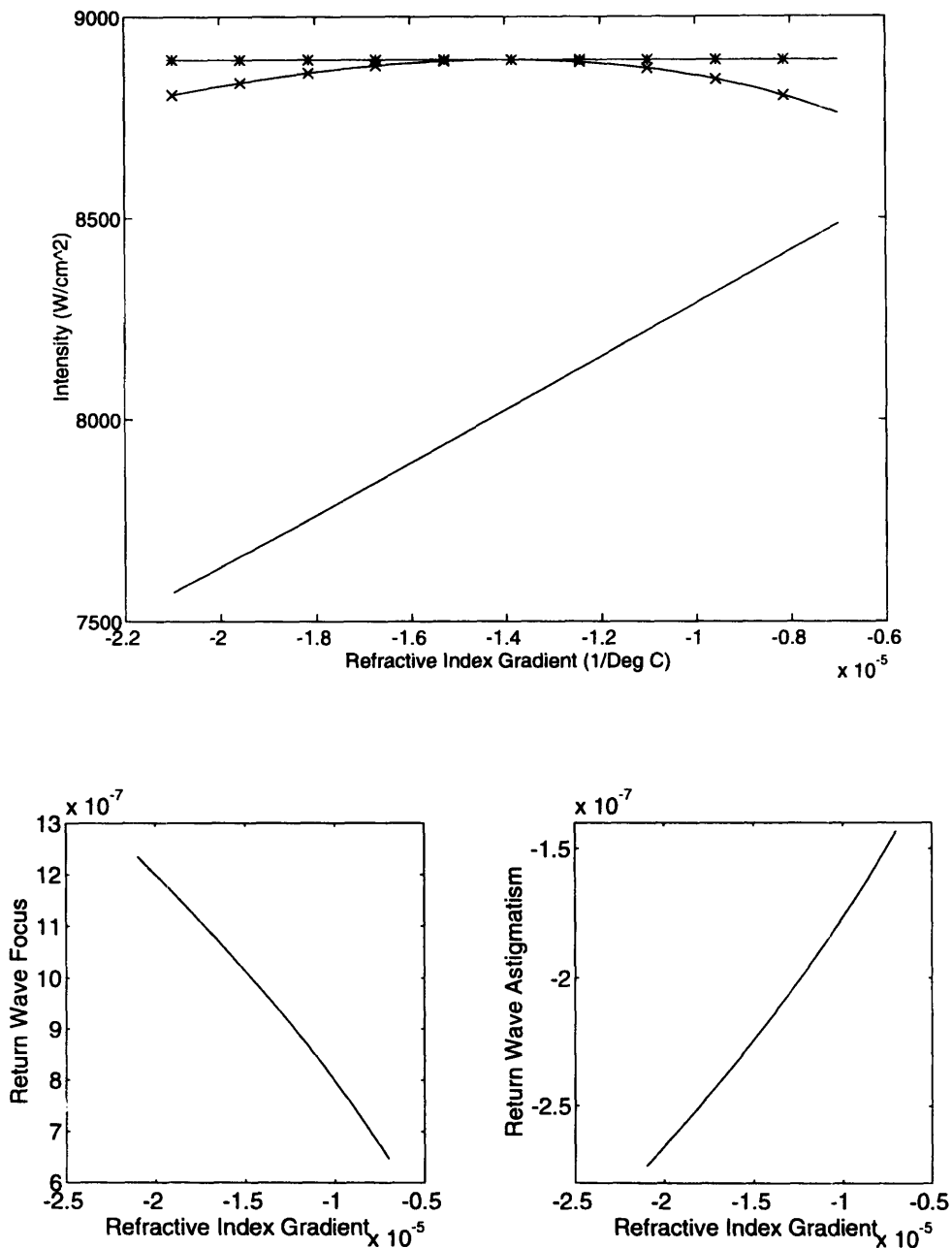


Figure B.6 Sensitivity to Refractive Index Gradient.

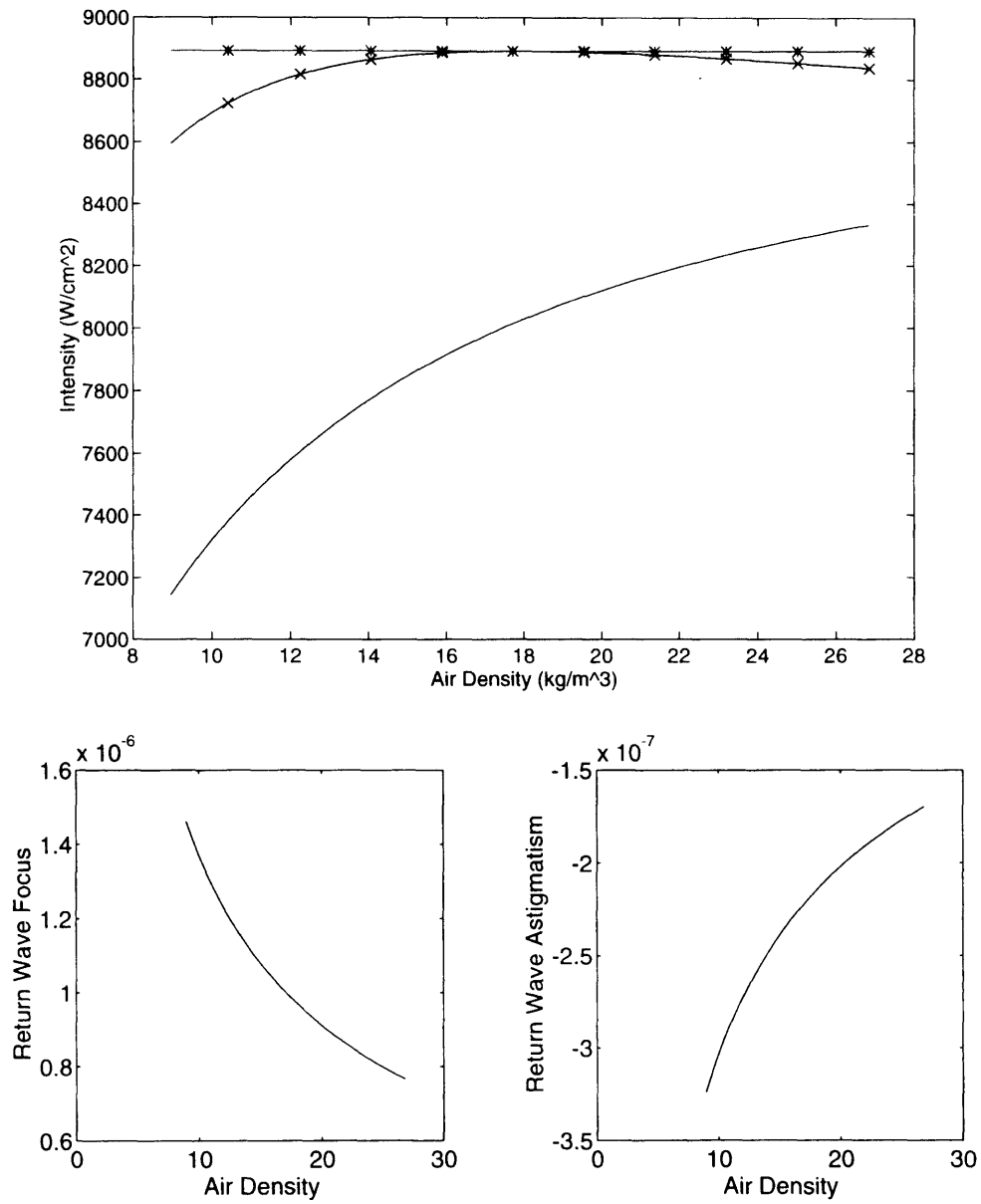


Figure B.7. Sensitivity to Air Density.

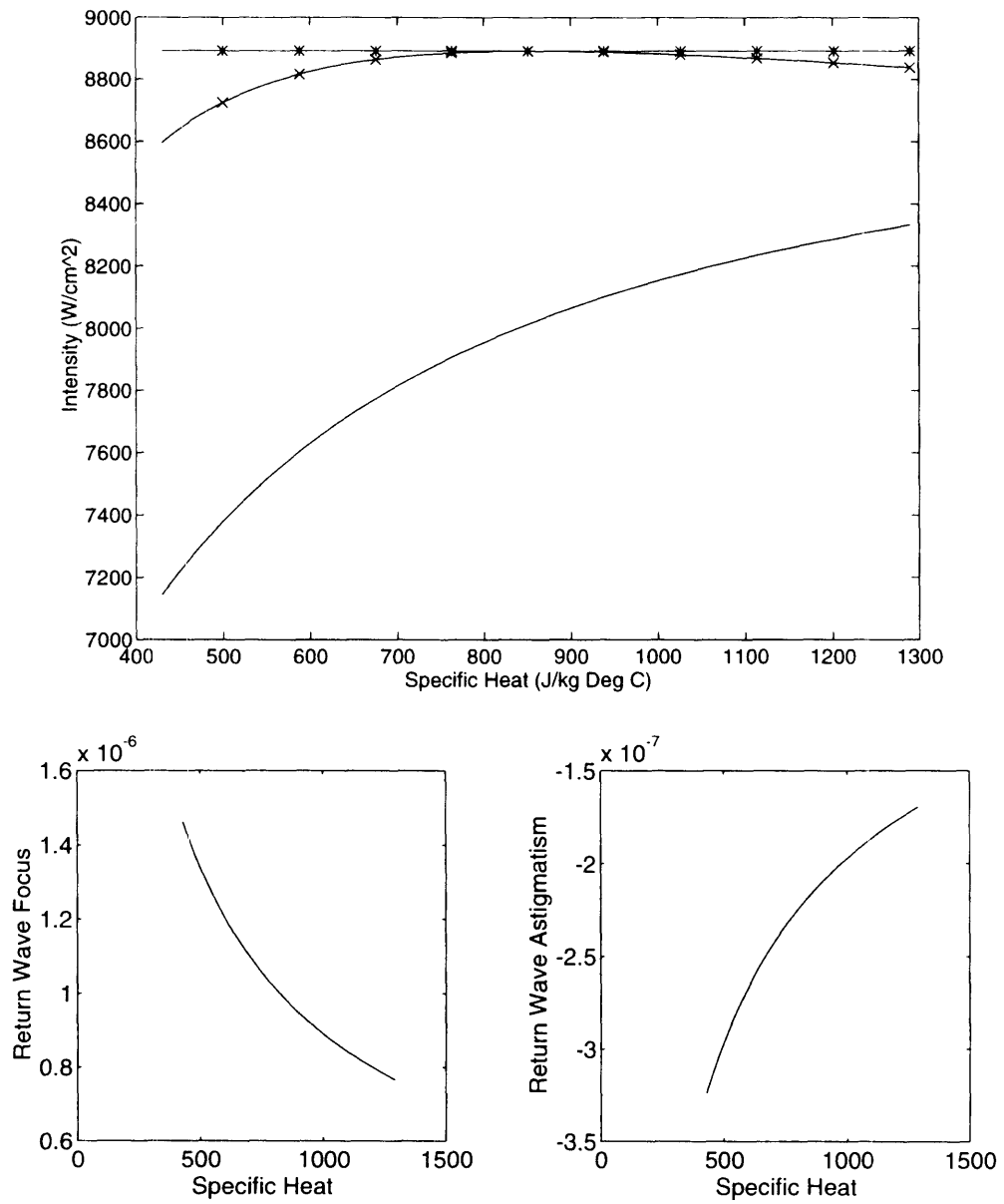


Figure B.8. Sensitivity to Specific Heat.

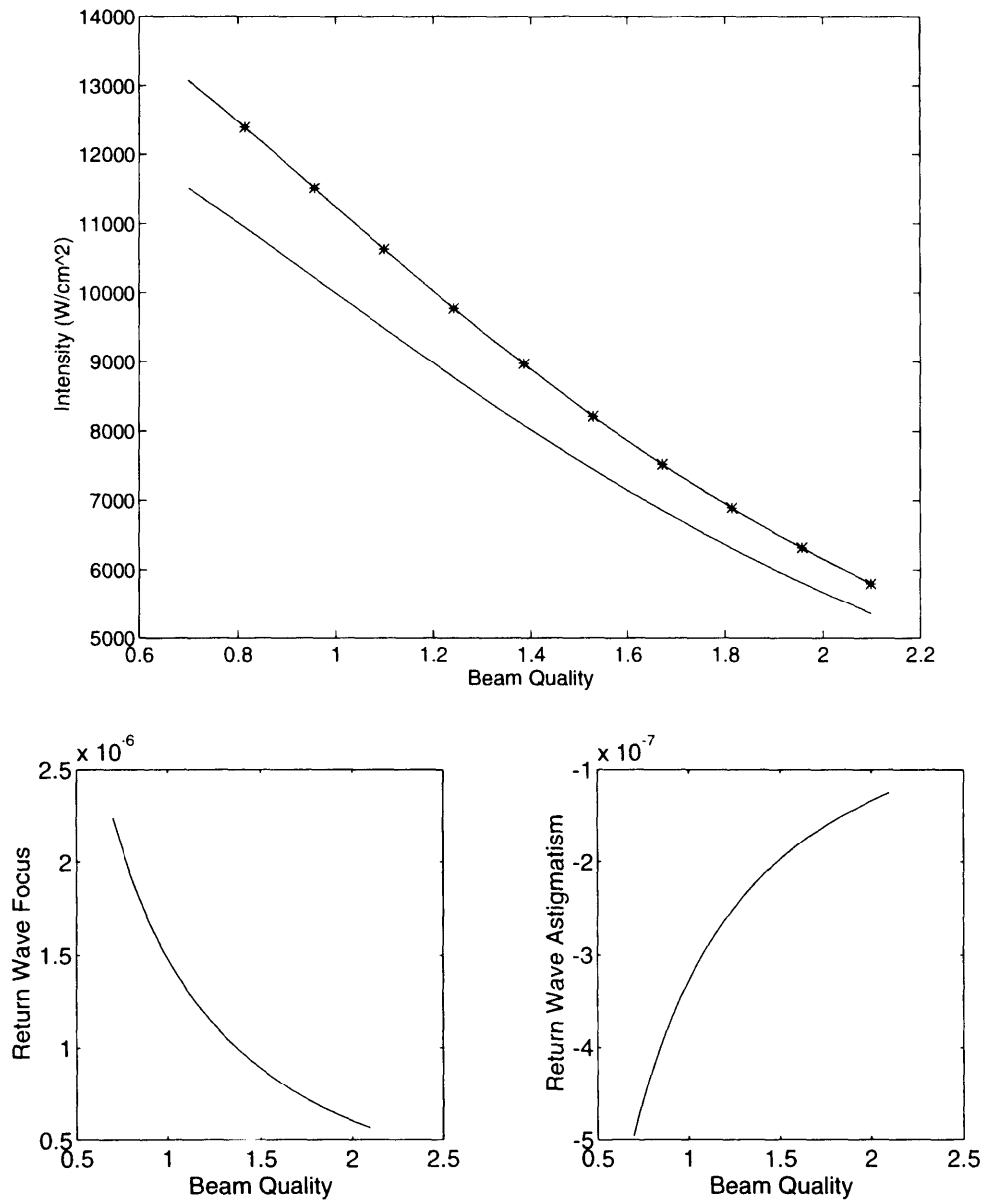


Figure B.9. Sensitivity to Beam Quality.

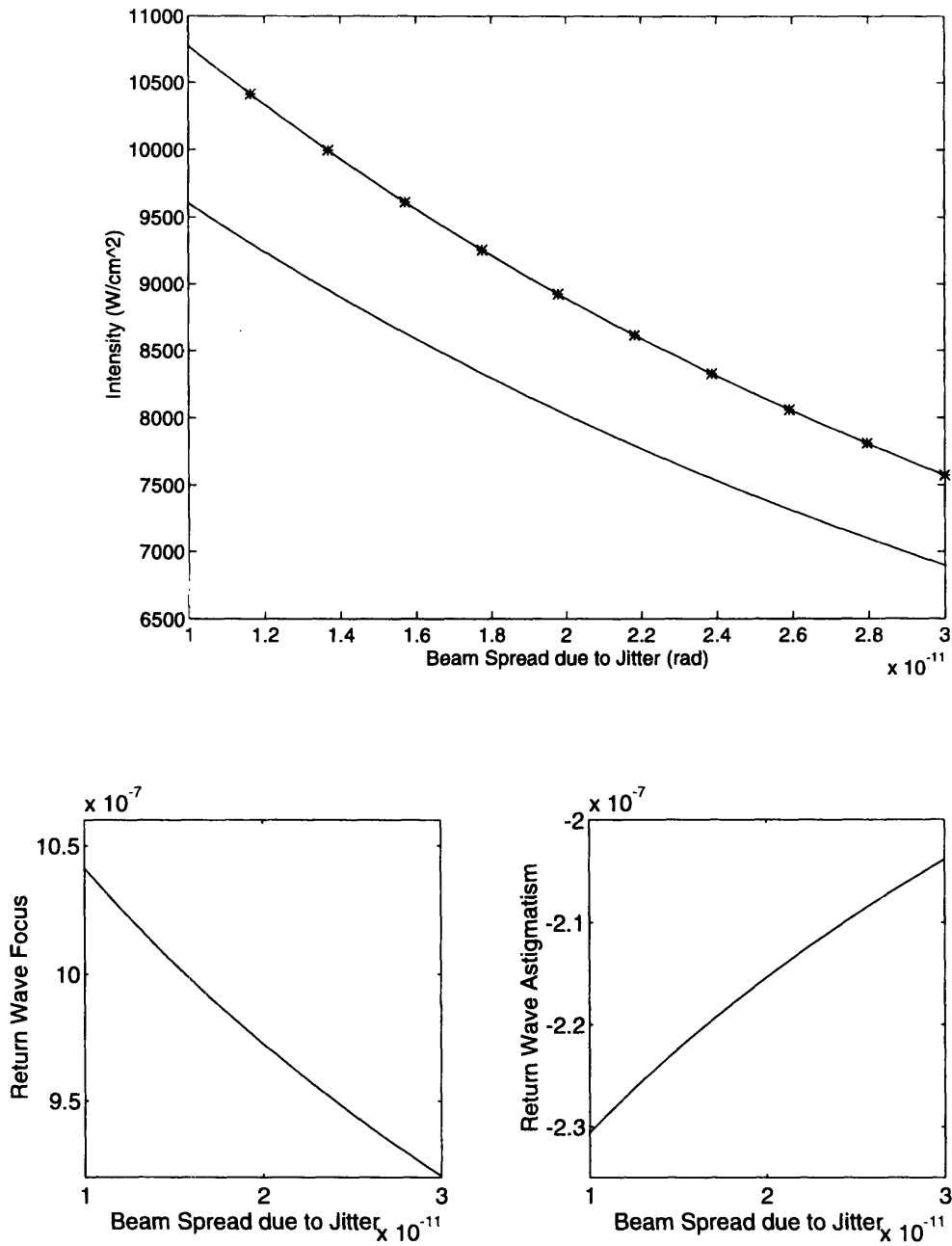


Figure B.10. Sensitivity to Beam Spread due to Jitter.

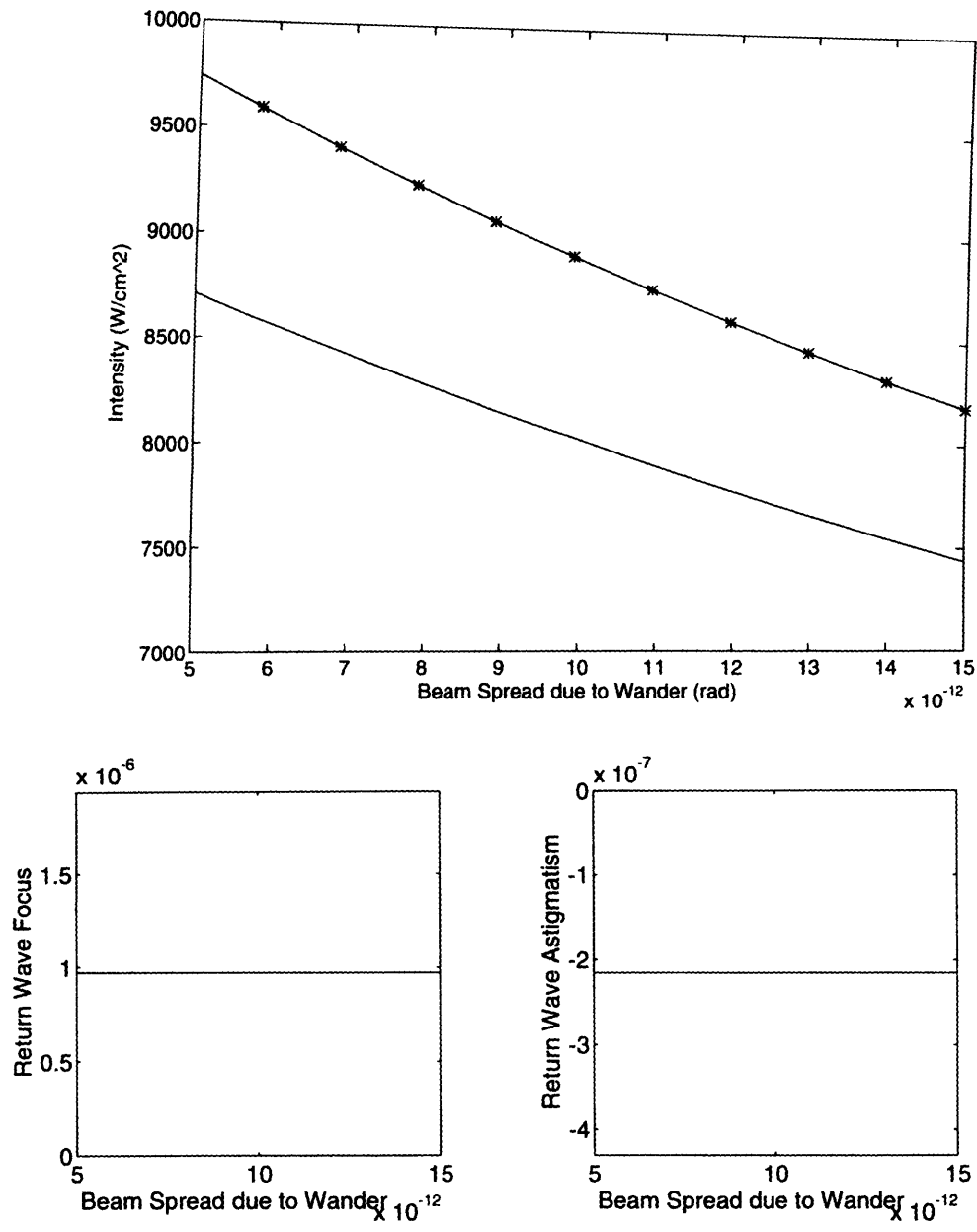


Figure B.11. Sensitivity to Beam Spread due to Wander.

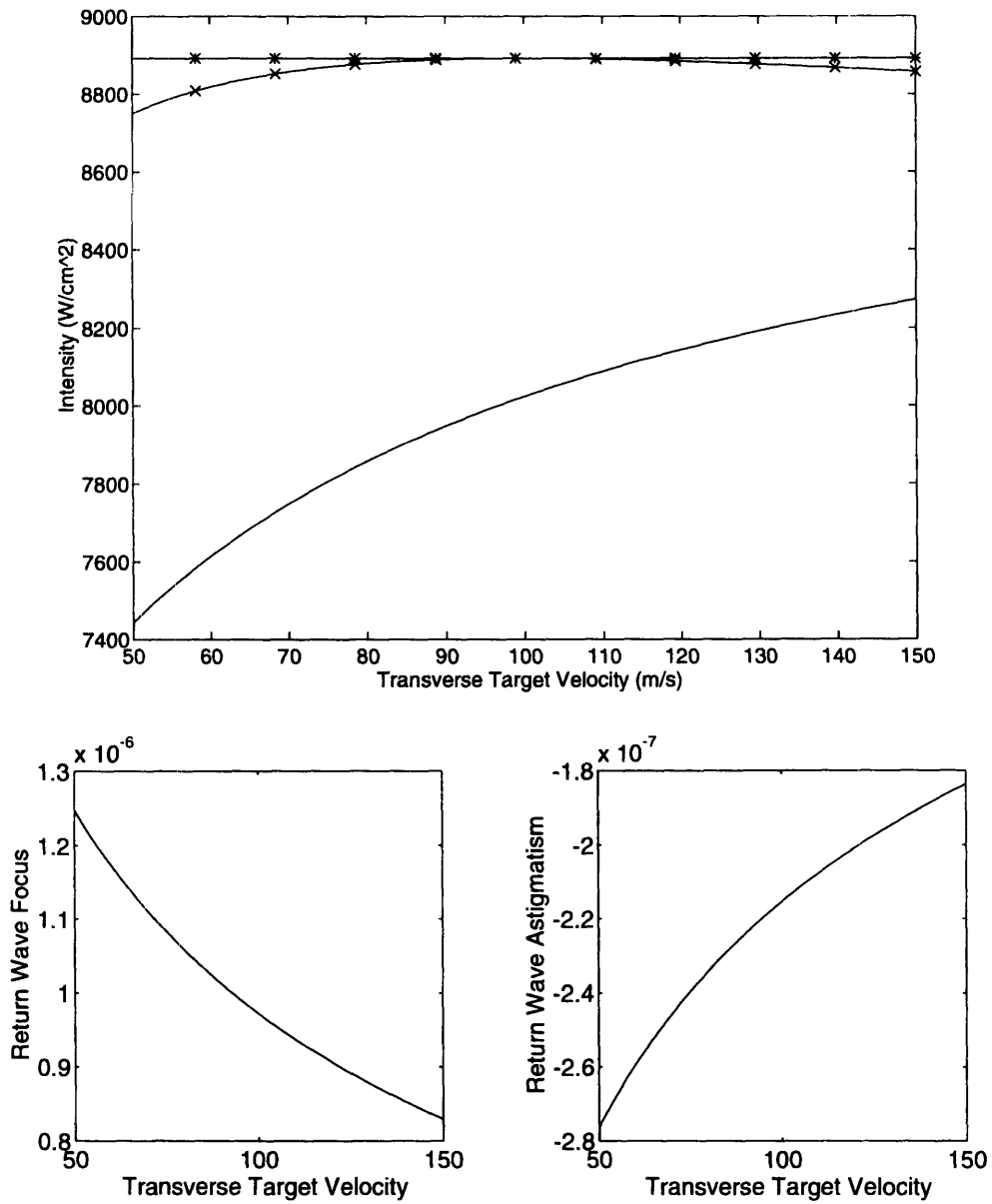


Figure B.12. Sensitivity to Transverse Target Velocity.

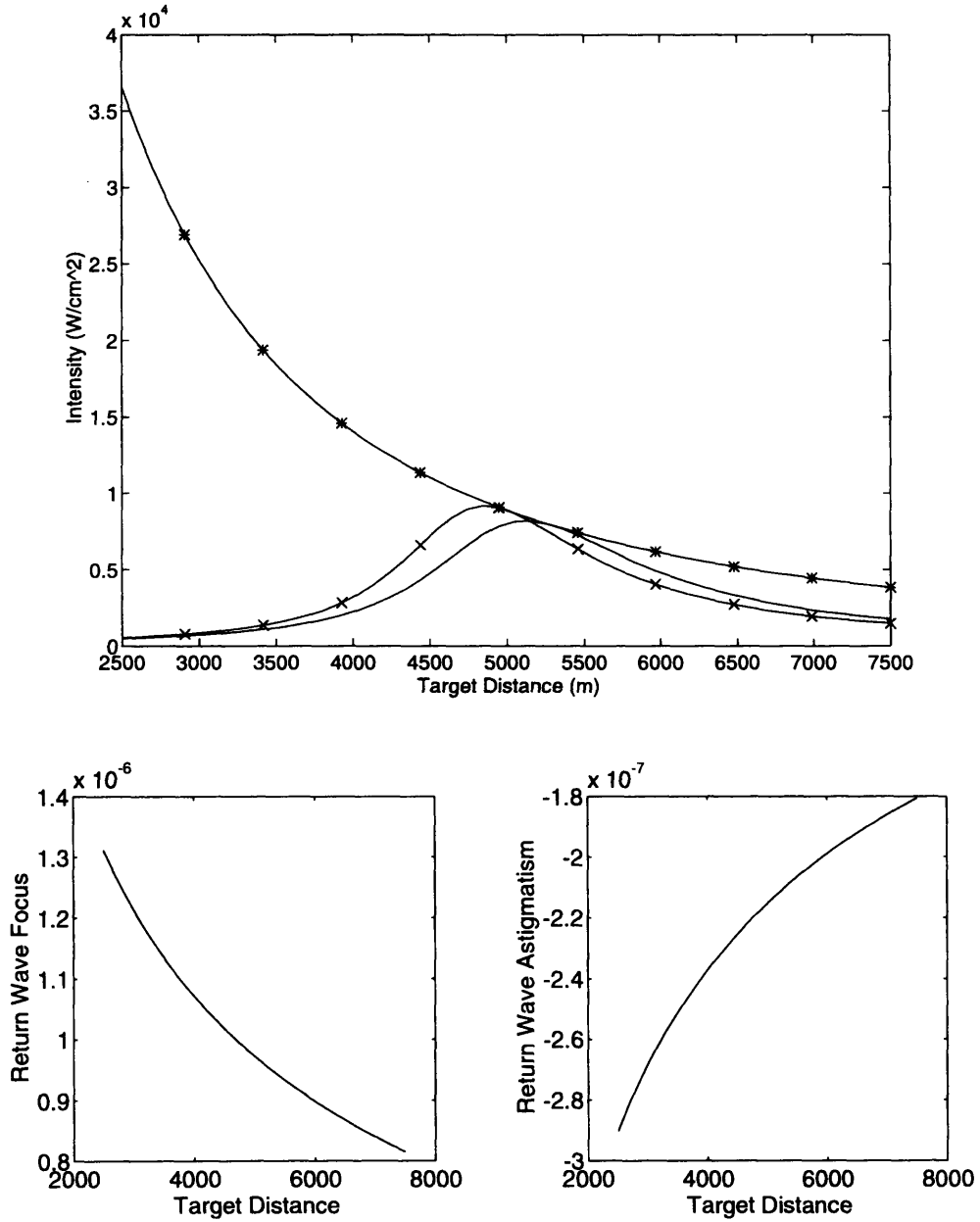


Figure B.13. Sensitivity to Target Distance.

References

- [1] Tyson, R., *Principles of Adaptive Optics*, Harcourt Brace Jovanovich, 1991
- [2] Smith, D., "High-Power Laser Propagation: Thermal Blooming," *Proc. of IEEE*, Vol. 65, No. 12, pp. 1679-1714, Dec. 1977
- [3] Gebhardt, F., "High Power Laser Propagation," *Applied Optics*, Vol. 15, No. 6, pp. 1479-1493, June 1976
- [4] Bradley, L. and J. Herrmann, "Phase Conjugation for Thermal Blooming," *Applied Optics*, Vol. 13, No. 2, pp. 331-334, February 1974
- [5] Gebhardt, F., "Twenty-Five Years of Thermal Blooming: An Overview," *Proc. SPIE*, Vol. 1221, pp. 2-24, 1990
- [6] Schonfeld, J., "The Theory of Compensated Laser Propagation through Strong Thermal Blooming," *Lincoln Laboratory Journal*, Vol. 5, No. 1, pp. 131-150, Spring 1992
- [7] Greenwood, D. and C. Primmerman, "Adaptive Optics Research at Lincoln Laboratory," *Lincoln Laboratory Journal*, Vol. 5, No. 1, pp. 3-24, Spring 1992
- [8] Karr, T., "Thermal Blooming Compensation Instabilities," *J. Opt. Soc. Am. A*, Vol. 6, No. 7, pp. 1038-1048, July 1989
- [9] Schonfeld, J., "Linearized Theory of Thermal-Blooming Phase-Compensation Instability with Realistic Adaptive Optics Geometry," *J. Opt. Soc. Am. B*, Vol. 9, No. 10, pp. 1803-1811, October 1992
- [10] Born, M. and E. Wolf, *Principles of Optics*, Pergamon Press, 1980
- [11] Breaux, H., W. Evers, R. Sepucha, C. Whitney, "An Algebraic Model for Continuous-Wave Thermal-Blooming," CSDL Report R-1173, July 1978
- [12] Holmes, D., J. Korba, and P. Avizonis, "Parametric Study of Apertured Focused Gaussian Beams," *Applied Optics*, Vol. 11, p. 565, 1972
- [13] Breaux, H., "Correlation of Extended Huygens-Fresnel Turbulence Calculations for a General Class of Tilt Corrected and Uncorrected Laser Apertures," BRL Interim Memorandum Report No. 600, May 1978
- [14] Whitney, C., "An Algebraic Model of Adaptive Optics for Continuous-Wave Thermal Blooming," CSDL Report R-1235, January 1979

REFERENCES

- [15] Breaux, H., "A Methodology for Development of Simple Scaling Laws for High Energy CW Laser Propagation," BRL Report ARBRL-TR-02039, January 1978
- [16] Breaux, H., "A Phase Integral Scaling Law Methodology for Combined Repetitive Pulse and CW High Energy Laser Propagation," BRL Interim Memorandum Report, August 1977
- [17] Bures, K., "A Target Intensity Model for Adaptive Optics Analysis," TASC Report 871-1 Rev. 1, July 1978
- [18] "A Model for Atmospheric Turbulence Dynamics," TASC Technical Information Memorandum, Feb. 1978
- [19] Noll, R., "Zernike Polynomials and Atmospheric Turbulence," *J. Opt. Soc. Am.*, Vol. 66, No. 3, pp. 207-211, March 1976
- [20] Hogge, C. and Butts, R., "Frequency Spectra for the Geometric Representation of Wavefront Distortions Due to Atmospheric Turbulence," *IEEE Trans. Antennas and Propagation*, Vol. AP-24, No. 2, pp. 144-154, March 1976
- [21] Rugh, W., *Linear System Theory*, Prentice Hall, 1993
- [22] Hecht, E., *Optics*, Addison Wesley, 1990
- [23] Grace, A., *Optimization Toolbox User's Guide*, The MathWorks, 1992
- [24] Wolfe, W., *Handbook of Military Infrared Technology*, Office of Naval Research, Dept. of the Navy, 1965
- [25] Wolfe, W., and G. Zissis, *The Infrared Handbook*, Environmental Research Institute of Michigan, 1985
- [26] Smith, F., *The Infrared Electro-Optical Systems Handbook: Atmospheric Propagation of Radiation*, SPIE Optical Engineering Press, 1993
- [27] Gelb, A., *Applied Optimal Estimation*, The MIT Press, 1982